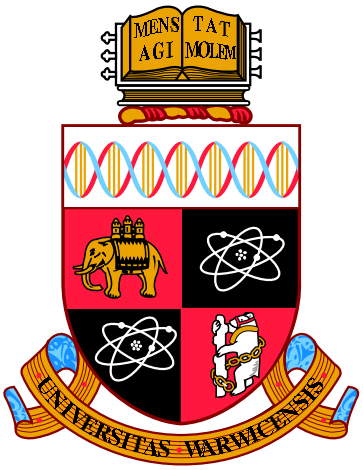

Analytical Approaches for Probing Surface Properties and Reactivity

by

Rehab Al Botros

Thesis

Submitted to the University of Warwick

for the degree of

Doctor of Philosophy

Department of Chemistry

June 2015

THE UNIVERSITY OF WARWICK

To my soul mate Moufid and my little treasure Marcelle
without you my life is empty and my knowledge is worthless.

Contents

List of Figures

List of Tables

Abbreviations

AC	Alternating Current
AFM	Atomic Force Microscopy
ANOVA	ANalysis Of VAriance
BM-SICM	Bias Modulated SICM
CLSM	Confocal Laser Scanning Microscopy
CV	Cyclic Voltamogram
DC	Direct Current
DDL	Diffuse Double Layer
DM-SICM	Distance Modulated SICM
EDOT	4,3-ethylenedioxythiophene
ET	Electron Transfer
FEM	Finite Element Method
Fl	Fluorescein
HAP	Hydroxylapatite
ICR	Ion Current Rectification
IHP	Inner Helmholtz Plane

IP	Ionic Product
ISME	Ion Selective Microelectrode
ITIES	Interface between Two Immiscible Electrolyte Solutions
OHP	Outer Helmholtz Plane
PDEs	Partial Differential Equations
PEDOT	Poly 4,3-ethylenedioxythiophene
ppm	part per million
QRCE	Quasi Reference Counter Electrode
RMS	Root Mean Squared
SECCM	Scanning ElectroChemical Cell Microscopy
SECM	Scanning ElectroChemical Microscopy
SEM	Scanning Electron Microscope
SG/TC	Substrate Generation Tip Collection
SICM	Scanning Ion Conductance Microscopy
SPIP	Scanning Probe Imaging Processor
SPM	Scanning Probe Microscopy
TG/SC	Tip Generation Substrate Collection
TMSDMA	N-(Trimethylsilyl)dimethylamine
UME	Ultramicroelectrode

Acknowledgments

First and foremost, I want to thank my daughter Marcelle and my husband and soul mate Moufid Al Thiraawi for believing in me, supporting me through my time at Warwick, putting up with my modes and my crazy scientific chats, and especially for all the enjoyable walks and nice meals that we shared together.

I would like to express my deep gratitude to my supervisor, Prof. Patrick Unwin, for his encouragement and continuous support through out my PhD years. Without him I would not be able to do it.

I also thank the mechanical and electronic workshops for their amazing skills (Rodney Wesson, Lee Butcher and Marcus Grant), and Dr. Alex Colburn for the superb custom electronics, without which our science would not be possible.

I would like to acknowledge the support from a European Research Council Advanced Investigator Grant (ERC- 2009-AdG247143 Quantif) for funding.

All my friends and colleagues in the Electrochemistry and Interfaces group, for all the science, and the fun activities, over the last four years. Especially the awesome Sophie Kinnear, Binoy Paulose Nadappuram for the best time in my life.

I would like to thank Dr. Massimo Peruffo, Dr. Michael O'Connell, Dr. Kim McKelvey, Dr. Maxim Joseph and Dr. Dmitry Momotenko for all the fruitful scientific discussions, I learned so much of you guys.


arwick
Electrochemistry &
Interfaces Group

Declarations

The work presented in this thesis is entirely original and my own work, except where acknowledged in the text. I confirm that this thesis has not been submitted for a degree at another University.
Experimental work in Chapter 2 was mostly carried out by David Perry.
Experimental work in Chapter 5 was carried out by Binoy Paulose Nadappuram.
Experimental work in Chapter 6 was carried out by Alexander Parker.

Chapter 2 was published as:

Perry D.; **Al Botros, R.**; Momotenko D.; Kinnear S.; Unwin, P. R., Simultaneous Nanoscale Surface Charge and Topographical Mapping. *ACS Nano* **2015**, in press DOI: 10.1021/acsnano.5b02095

Chapter 5 was published as:

Paulose Nadappuram B.; McKelvey K.; **Al Botros R.**; Colburn A. W.; and Unwin P. R., Fabrication and Characterization of Dual Function Nanoscale pH-Scanning Ion Conductance Microscopy (SICM) Probes for High Resolution pH Mapping. *Anal. Chem.* **2013**, 85, 8070 - 8074.

Chapter 6 is in preparation for:

Al Botros, R., *et al* Combinatorial Localized Dissolution Analysis: Application to Acid-induced Dissolution of Dental Enamel and the Effect of Surface Treatments

Chapter 3 is in preparation for:

Al Botros, R., *et al* Transient Interfacial Kinetics, from Confocal Fluorescence Visualization: Application to Proton Attack at the Treated Enamel Substrate

Chapter 4 is in preparation for:

Al Botros, R., *et al* Dual Functional Ion Selective Microelectrode - Scanning Ion Conductance Microscopy (ISME-SICM) Probe: Fabrication and Characterization

Abstract

This thesis reports new analytical approaches involving the employment of various scanning probe microscopy techniques (along with other microscopy techniques), coupled -in particular- with numerical modelling to extract key information about surface properties and crystal dissolution. The set of techniques used include scanning electrochemical microscopy (SECM), scanning ion conductance microscopy (SICM), scanning electrochemical cell microscopy (SECCM), ion selective electrodes (ISEs), atomic force microscopy (AFM), and confocal laser scanning microscopy (CLSM). In general, the approaches involve the coupling of data from two techniques to enhance the amount of information that could be obtained in an experiment. A new bias modulated SICM technique is introduced as a powerful tool to map topography and surface charge density simultaneously. This significant advance takes SICM beyond its original use as a topographical technique and turns it into a method of greater scope and versatility. To further advance scanning electrochemical probe microscopy, the fabrication and application of dual function electrodes, coupling both SICM and SECM techniques is described. The SICM was used to map sample topography and for the local delivery of agents to the sample surface (here calcite microcrystals), while the SECM part was employed as an ion selective electrode to acquire ion activity profiles (Ca^{2+} and H^{+}, respectively) in bulk solution and in proximity to the surface. The pH probe size was pushed down to the nanoscale, while the calcium ones were in the 1.5 - 3 µm across. A major aspect of this work was to analyse experimental measurements with numerical finite

element method simulations enabling the determination of dissolution flux values, thus opening the door to many possible and interesting applications for these probes in the future. Acid attack on dental enamel surfaces is also considered using different approaches. In one approach SECM was coupled with CLSM to visualise the proton diffusion profile near enamel surfaces in a bid to extract highly temporal kinetic information about the acid attack on enamel. An attentive approach was to use the SECCM technique as a tool to probe acid-induced dissolution of enamel, by locally delivering protons with a well defined mass transport. Landing with the acidic droplet on the sample surface for different time periods generated etch pits, which were then analysed with AFM. A key aspect was to develop a numerical *finite element method* (FEM) model that was employed to extract dissolution kinetics for the different types of enamel samples (treated and untreated).

Chapter 1

Introduction

This thesis is concerned with the employment of new techniques and approaches for the investigation of surface properties (surface charge, dissolution kinetics, acid attack and localised concentrations) at solid/liquid interfaces. Accordingly, this chapter gives an overview of all the techniques that are used in this investigation, as well as the studied materials (calcite and tooth enamel). Each chapter in this thesis is self-contained and based on a journal article that is in print or in preparation. As such, each chapter contains a focused introduction of the material in this chapter which serves to provide a general background.

1.1 Dynamic Electrochemistry

Dynamic electrochemistry describes the phenomenon of electron transfer at electrode surfaces at non-equilibrium conditions. Once a potential is applied to an electrode, reactive species are transported from bulk solution towards the electrode/ solution interface, where they undergo electron transfer. Figure 1.1 illustrates the

processes that might be involved in this process, such as adsorption or desorption and reactions at the interfacial regions, plus the mass transport at the bulk region.[1] The current flow at the electrode is controlled by the rate of the previous processes, and depends highly on the slowest step.[2]

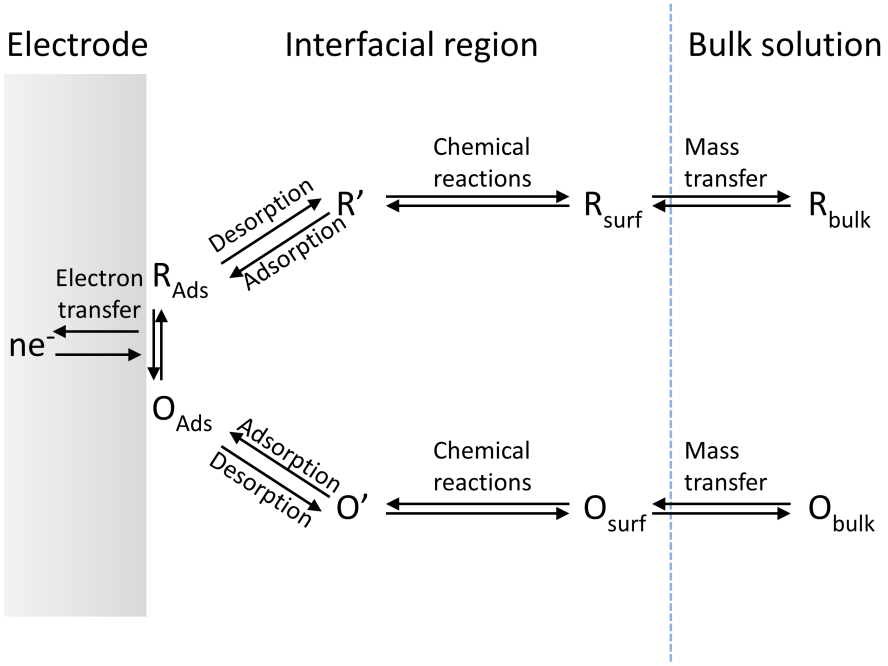

Figure 1.1: A schematic diagram of a general electrode reaction.[2]

1.1.1 Electron Transfer

For a simple system at equilibrium such as O/R active pair, where the following reaction occurs:

$$O + ne^- \rightleftharpoons R \tag{1.1}$$

The potential of the electrode can be linked to the activity of the oxidised and reduced molecules with the Nernst equation:[1]

$$E = E^0 - \frac{RT}{nF} ln \frac{a_R}{a_O} \tag{1.2}$$

where E is the electrode potential, E^0 is the standard potential of the electrode, R is the molar gas constant, T is the absolute temperature, F is Faraday constant, n is the number of transferred electrons, and a_R and a_O are the activities of reduced and oxidized species respectively.

Despite the fact that dynamic electrochemistry studies systems that are not at equilibrium, a Nernstian behaviour could be assumed in the case where electron transfer kinetics are so fast that the mass transport governs the electrode response.[2,3]

1.1.2 Mass Transport

Species movement in solution from bulk towards the electrode surface arise from three phenomena, diffusion, convection and migration. The mass transport under those phenomena can be described by the Nernst-Planck equation:[1,2]

$$J_i = -D_i \bigtriangledown c_i - \frac{z_i F}{RT} D_i c_i \bigtriangledown \phi + c_i \upsilon \tag{1.3}$$

where J_i denotes the mass transport flux of species i. D_i, z_i and c_i are the diffusion coefficient, charge number and concentration of species i respectively. ϕ is the electric potential, and υ is the solution velocity.

Diffusion

Diffusion is the movement of species under the influence of concentration gradient. Fick's first law describes diffusion at steady state conditions.[2]

$$J_{i,d} = -D_i \bigtriangledown c_i \tag{1.4}$$

$J_{i,d}$ is the diffusive flux, and $\bigtriangledown$ is the gradient operator in the space of interest. The negative sign denotes that the species move from a region with low concentration to a region with a high concentration. Fick's second law describes the diffusion of

species with time as follows:[2]

$$\frac{\partial c_i}{\partial t} = -D_i \bigtriangledown^2 c_i \tag{1.5}$$

Convection

Convection occurs due to the mechanical movement of the solution itself rather than the movement of species inside the solution. There are two types of convection, *natural convection* which arises due to temperature and density changes in the solution; and *forced convection* which is introduced to the solution to increase the mass transport by stirring or pumping of the solution. The convective flux is descrided with the following equation:[3]

$$J_{i,c} = +c_i \upsilon \tag{1.6}$$

Migration

Migration is the movement of charged species under the influence of electrical field, and the migration flux is given as follow:[3]

$$J_{i,m} = -u_i c_i \bigtriangledown \phi \tag{1.7}$$

where the mobility u_i is given as:

$$u_i = \frac{z_i F}{RT} D_i \tag{1.8}$$

1.1.3 Electric Double Layer

At the event of immersing a solid in a liquid phase, an interfacial region forms where the electrostatic potential (ϕ) differs from that in bulk solution. In this region charges from the bulk solution are arranged close to the interface to neutralize the accumulated charge at the solid surface. This ordering of charge is called the *electric*

double layer.[2,3]

Development of the double layer model

Helmholtz was the first to introduce a model to explain the double layer arrangement, proposing that a charged electrode attracts counter-ions and repel co-ions once immersed in an electrolyte solution. He suggested the formation of a rigid planar double layer at the electrode/liquid interface, which is able to store charge electrostatically and behaves as a planar capacitor as shown in Figure 1.2.

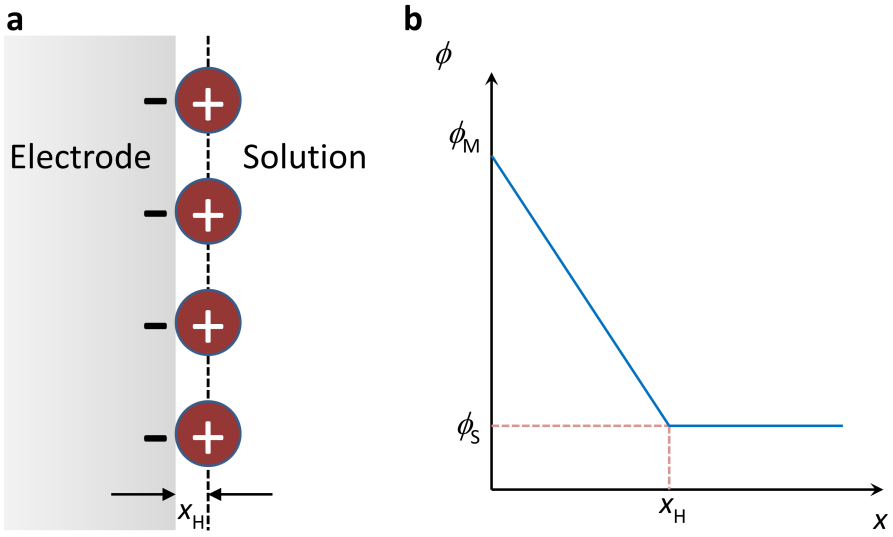

Figure 1.2: A schematic diagram of a) the Helmholtz outer plane (note big circles denote solvated ions). b) The interfacial potential change with distance from the surface.

The double layer capacity in the Helmholtz model is described as:[3]

$$C_{d,H} = \frac{\epsilon_r \epsilon_0}{x_H} \tag{1.9}$$

where ϵ_r, ϵ_0 are the relative permittivity and the permittivity of vacuum respectively. x_H is the closest distance an ion can come to the electrode surface (ionic radius). The Helmholtz model does not take into account any interactions occurring further than the first layer next to the electrode surface, and ignores the effect of electrolyte

concentration, thermal motion, adsorption and solvent-surface interactions.

Gouy-Chapman theory introduced the *diffuse* model to the double layer, where the electric potential decreases exponentially with distance from the surface.[3] Both Gouy and Chapman (independently) proposed the effect of electrode potential and ionic concentration on the value of the double layer capacity, suggesting that the double layer is not rigid as previously described by Helmholtz, but rather it is of various thickness where the ions are free to move. The double layer thickness x_{DL} can be obtained using the following equation assuming $z:z$ electrolyte:[3]

$$x_{DL} = (\frac{\epsilon_r \epsilon_0 k_B T}{2 n_i^0 z^2 e^2})^{1/2} \tag{1.10}$$

where k_B is Boltzman constant, n_i^0 is the numerical bulk concentration and the double layer thickness increase with decreasing ionic strength. Figure 1.3 illustrates the schematic of the diffusive double layer and the change in interfacial potential for this theory, however it is good to note that ions are considered here to be point charges, so theoretically there is no maximum value for the ion concentration near the surface, thus the model fails for double layers.

Stern joined the two previous models,[4] claiming the presence of a compact *finite size ion* layer next to the electrode surface, followed by *point charges diffuse layer* extending to the bulk solution. Thus, distinguishing between the adsorbed ions and the diffused double layer. The interfacial potential in this theory drops linearly across the first layer then drops exponentially across the diffuse layer (Figure 1.4).

Grahame,[5] however, presented the existence of three distinctive regions in the double layer, the first region is the specifically adsorbed ions that lose their solvation shell, which they are closest to the surface. Those ions can hold similar or opposite charge to the surface, and the plane passing through their centers is called the *inner Helmholtz plane* IHP. The second region are the solvated and non-specifically adsorbed ions, where the plane passing through the ions center is

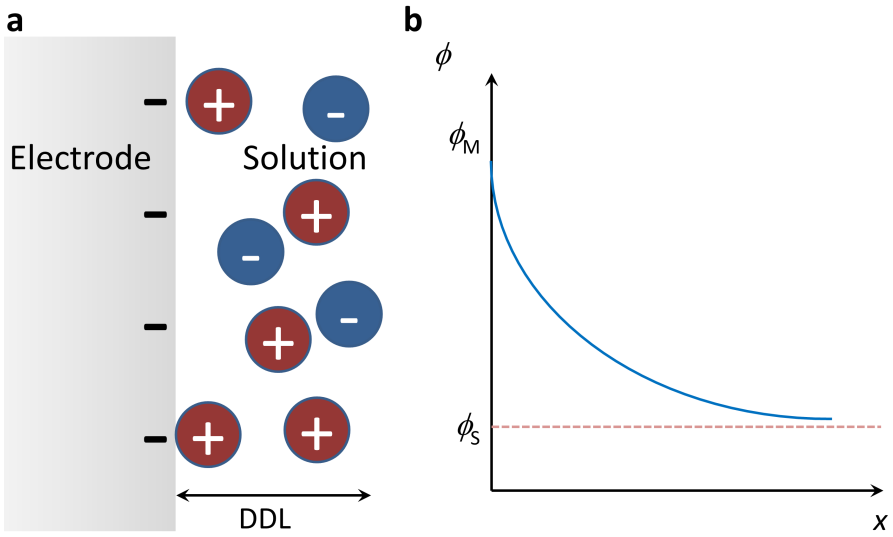

Figure 1.3: A schematic diagram of a) the *diffuse double layer* arrangement as in Gouy-Chapman theory (note big circles denote solvated ions). b) The interfacial potential exponential change with distance from the surface according to Gouy-Chapman theory.

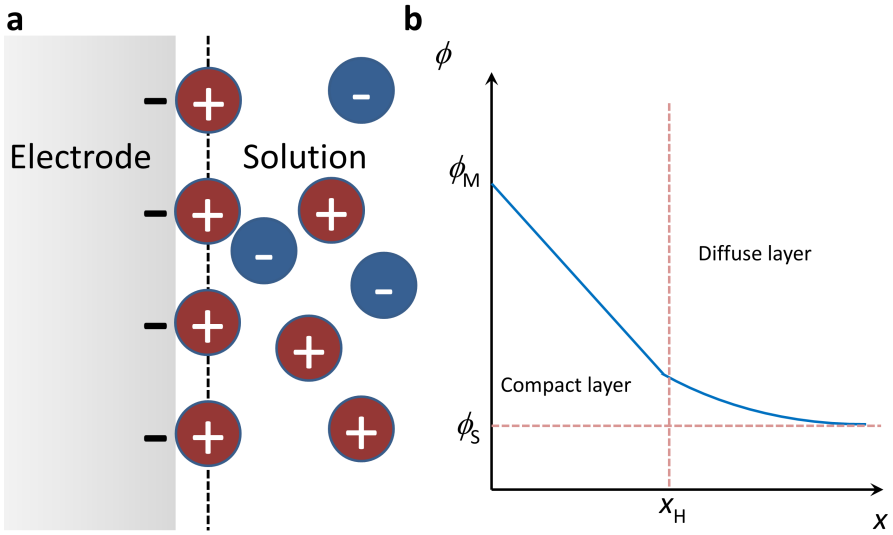

Figure 1.4: A schematic diagram of a) the Stern double layer theory (note big circles denote solvated ions). b) The interfacial potential change with distance from the surface according to Stern model.

called the *outer Helmholtz plane* OHP. The third region is the diffuse double layer which extends outside the OHP towards the bulk solution (Figure 1.5).[5] More recent studies investigated the effect of the physical nature of the interfacial region,

with consideration of the bipolar properties of water as a solvent, This has led to introducing the zeta potential.[3]

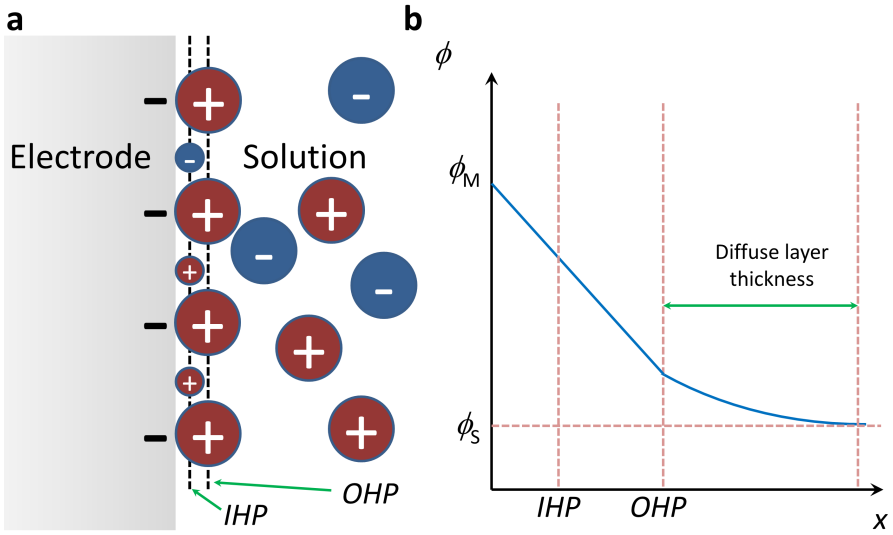

Figure 1.5: A schematic diagram of a) the three regions in the double layer arrangement according to Grahame (note big circles denote solvated ions, small circles represent the adsorbed ions which lost their solvation shell). b) The interfacial potential change with distance from the surface.

1.1.4 Ultramicroelectrodes (UMEs)

The Ultramicroelectrodes by definition are electrodes with one dimension at least that is smaller than the diffusion layer δ, called the critical dimension r.[2,6] In practice, this means that the electrode critical dimension is in the micrometre range (0.1 - 50 µm). Thus, UMEs have a high current density but low current flow allowing the usage of two electrodes setup. The exposed metal part can take different geometries[7,8] depending on its application, which include spherical, hemispherical, ring,[10,11] band,[12,13] arrays,[14,15] mercury electrodes,[15,16] carbon fibre[17,18] and disk.[19] The planar disk UME is the most popular electrode in experiments.[20] Figure 1.6a and c illustrates the differences in the diffusion layer between a macroelectrode and a disk UME. The diffusion profile towards the infinite size electrode surface is purely planar (equation 1.11), while at the UME surface it is hemispherical. Thus, enhanc-

ing the mass transport towards the electrode (equation 1.12),[21] which yields in a steady state voltammetric response[22] at low scan rates (Figure 1.6b). While for a conventional electrode the current tails off due to the inability of planar mass transport diffusion to provide unreacted species rapidly enough to the electrode surface (Figure 1.6d).[23]

$$\frac{\partial c}{\partial t} = D\frac{\partial^2 c}{\partial x^2} \tag{1.11}$$

$$\frac{\partial c}{\partial t} = D(\frac{\partial^2 c}{\partial r^2} + \frac{1}{r}\frac{\partial c}{\partial r} + \frac{\partial^2 c}{\partial z^2}) \tag{1.12}$$

The limiting current at a disk UME is given by the following equation:[2,26]

$$I = 4nFaDc_\infty \tag{1.13}$$

where n is the number of electrons transferred in the electrode reaction, F is Faraday's constant, D is the diffusion coefficient of the reacting species, a is the disk electrode radius, and c_∞ is the bulk concentration.

UMEs have great advantages over macroelectrodes due to their distinctive properties. Their fast response times that are free from non-faradaic contributions[27] enable their application in fast-scan cyclic voltammetric techniques, and in the study of short timescale homogeneous and heterogeneous electron transfer processes.[9,28] The high mass transport of the microelectrodes are equivalent to the mass transport of a rotating disk macroelectrode with a few thousands rpm[7], which allows the study of fast electron transfer rates.[29] UMEs can be used in a wide range of high resistive media due to their low iR drop as they pass significantly low currents in the (pA-nA) range. Samples include non-aqueous solutions (oil, organic solvents, ...), solids (soil, food, ...), and biological samples in low electrolyte concentrations.[7,28–30] The UMEs small size and subsequently their small flowing currents make them

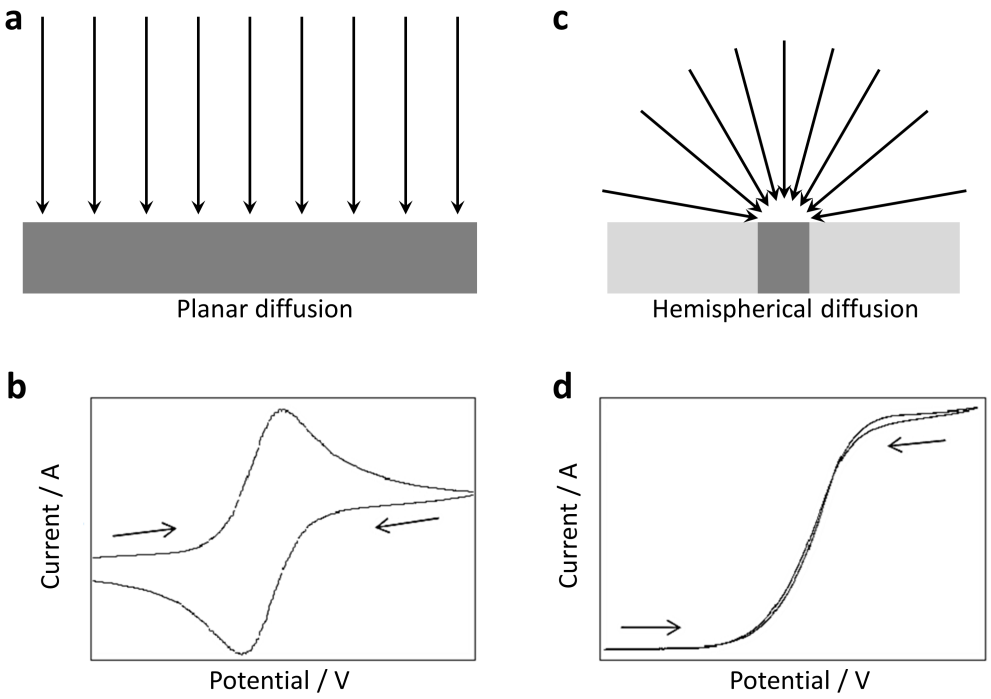

Figure 1.6: schematic diagram of a) planar diffusion at an infinite size electrode and b) voltammetric response. c) hemispherical diffusion at a disk ultramicroelectrode and d) steady state voltammetric response.

very attractive to use in medical and pharmaceutical research that involve micro-environment applications for both *in-vivo* and *in-vitro* studies (such as single cells and tissues).[31] Furthermore, the UMEs cause minimum damage to the studied media which allows their use *in-vivo* on living specimens such as mammalian brains to study catecholamine neurotransmitters production.[9,32–34]

The UME tip is normally characterised by the RG value, which is given by the following equation:[26]

$$RG = \frac{r_g}{a} \tag{1.14}$$

where r_g is the insulating glass radius and a is the metal disk radius. The RG value for most experiments is 10 as this minimised the back diffusion effects for the electrode.[26] The disk microelectrode can be fabricated easily by sealing a metal wire

or a carbon fibre in a glass insulating shield.[8,35] There are two common methods of fabrication,[36] the first one is where a glass capillary of about 10 cm length and 1 mm inner diameter and 2 mm outer diameter is sealed from one end with bunsen burner or a small torch. Then a metal wire ($\sim$ 2 cm) is inserted in the capillary and sealed in using flame while avoiding the formations of air bubbles around the wire. The electrical contact is achieved by injecting silver epoxy through the open end of the capillary and inserting a copper wire. Subsequently, the metal wire is exposed by polishing the sealed glass end to reach the metal disk, and the surrounding glass is smoothed and polished to a reach the required RG value. In the second method, the metal wire is sealed inside a glass pipette through the use of a micropipette laser puller.[36]

1.2 Electroanalytical Methods

Electroanalytical methods are the type of techniques that study the properties of an analyte in an electrochemical cell, by either measuring the current under constant potential (amperometry),[37,38] or measuring potential without or with minimal current flow (potentiometry),[39,40] or measuring the current under the effect of variable and controlled potential signal (voltammetry).[41,42]

1.2.1 Amperometry

In an electrochemical cell, a potential is applied between the working electrode and the reference electrode and held at a chosen value to either oxidise or reduce the ion of interest. The amperometric detection is based on the measurement of the flowing current or the changes in the current value under this potential. Applications of this method include the detecting and titration of particular species selectively and quantitatively using the applied potential, such as uric acid,[43] dopamine,[44] acetylsalicylic acid in drugs,[45] ferrate[46] and palladium and platinum.[47]

1.2.2 Potentiometry

In potentiometric measurements, no current flows in the cell as no net Faradaic reaction occurs (open circuit). The measured potential at the indicator electrode in respect to the reference electrode is used to determine the concentration of an analyte in the solution.[2] This method is used in the ion selective electrode setup,[48] with applications in the environmental,[49] biological,[50,51] and biomedical sensors developments.[52] The potentiometric tip is considered to be a passive sensor as it does not change the concentration of the studied species.

1.2.3 Voltammetry

In voltammetry, information about the analyte is extracted from the recorded voltammogram, which is obtained by varying the potential between the working electrode and the reference electrode (either step by step or continuously), while recording the changes in the current value *vs.* the applied potential.[2] The different types of voltammetry are related to the manner of the change in potential. Thus, for linear sweep voltammetry[53] the potential is changed linearly with time, and the current displays a peak value due to the oxidation or reduction of ions at a certain potential value $E_{\frac{1}{2}}$, this value could be used to identify the reacting species and the current value is used to define the analyte concentration. In cyclic voltammetry[54] the potential is changed linearly from V1 to V2, then it is swept back to V1, this is called a cycle and can be repeated many times. This type of voltammetry is similar to the linear sweep method, although species in the solutions are oxidised during the increasing potential half cycle (at E_{pa}) and reduced back in the decreasing potential sweep (at E_{pc}). For a reversible couple the difference E_{pa} - E_{pc} is around $59/n$ on 1st sweep where n is the number of electrons in the Oxidation/Reduction process.[55] The information extracted in this method includes redox potentials,[56] electrochemical reaction rates,[57] and diffusion coefficients.[58] Stripping voltammetry[59] is a quantitative

analytical technique, where an analyte is deposited on the electrode during a deposition step (anodic,[60,61] cathodic[62,63] or adsorption[64,65] reaction), then during the stripping step the analyte is released into the solution resulting in a current value that is indicative of the analyte concentration. Other types of voltammetry include staircase voltammetry,[66,67] squarewave voltammetry,[68,69] and alternating current voltammetry.[70,71]

1.3 Scanning Probe Microscopy (SPM)

Scanning probe microscopy is a branch of imaging techniques that involves the use of a physical probe to measure a certain interaction effect of a sample surface, and subsequently build a multidimensional image based on the value of the measured interaction. The resolution of the acquired images differs between techniques, and relies highly on the size of the probe, and on the accuracy of the probe positioning. For some techniques atomic resolution can be obtained through the usage of piezoelectric materials as actuators, since very high voltages corresponds to tiny changes in the piezoelectric crystal dimensions.[72]

1.3.1 Scanning Electrochemical Microscopy (SECM)

The great advantage of the scanning electrochemical microscopy technique is its ability to perform all types of macroscopic electrochemical measurements in the microscale domain, which enable the characterisation of surfaces, structures and system kinetics at very high spacial resolution due to the use of UMEs. It is possible to track electron, ion, and molecule transfers, as well as detecting reactions at solid/liquid, liquid/liquid and liquid/gas interfaces. The probe physical movement during an experiment is controlled by a piezoelectric pusher, where accurate three dimensional positioning (*x,y and z*) is achieved using the piezo controller.[73,74] Since the SECM technique was introduced in 1989,[75] a massive volume of work

has been published exploring its methodology, instrumentations, capabilities and applications.[24,73,74,76–80] Several modes of scanning have been introduced, feedback mode, generation/collection mode, penetration mode and ion transfer feedback mode.

Feedback Mode

Feedback mode SECM[76,77,81] employs a UME as a working electrode with a sample that is immersed in an electrolyte solution, where a potential is applied to the UME to induce a reaction at the electrode/solution interface:

$$R_{(aq)} - e^{-} \rightleftharpoons O_{(aq)} \tag{1.15}$$

At bulk, the current flowing at the electrode tip reaches a steady state that is relatively immune to convection, with a hemispherical diffusion profile of the reactive species, see Figure 1.6b. However, once the electrode is positioned in close proximity to an inert surface, the current decreases while approaching the sample, as the diffused species get hindered by the sample surface, in what is known as a negative feedback signal (Figure 1.7a).[82,83] In the case of an active surface, a current enhancement is achieved due to the regeneration of the species at the sample surface, this is called a positive feedback (Figure 1.7b).[82,83] This change in current in both cases is a function of the tip-surface distance, thus it can be used as a feedback signal to track the topography and reactivity of the sample (Figure 1.7c).

A common issue that arises herein is how to distinguish between the signal corresponding to the topography and the one corresponding to the activity of the surface, as an increase in the current signal could be due either to surface activity, or to an increase in tip-substrate distance.[84] One way of resolving this issue is to introduce a distance-modulated mode, where a sinusoidal voltage signal is applied to the z-piezo controlling the tip, this would cause a positional oscillation ampli-

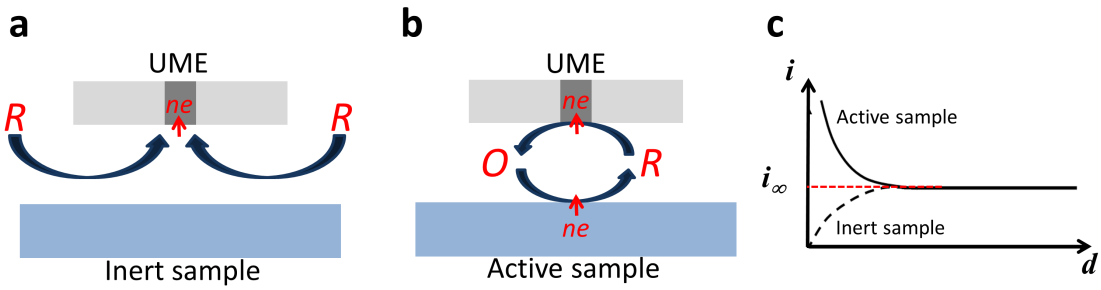

Figure 1.7: a) Hindered diffusion at an inert surface (negative feedback). b) Regeneration of species at an active sample (positive feedback). c) Approach curves for an active surface (solid line), and an inert sample (dashed line).

tude, and subsequently generates an alternating current component.[85] for an inert surface the current decreases on approaching the surface, thus both positional and current signals are in phase. On the other hand, the current would increase as approaching an active surface, thus the two signals are out of phase. By recording the phase between the modulated distance signal and the alternating current signal, it is possible to define if the surface is active or not, thus extracting the topography.[2] Another method of resolving the topography and reactivity of a surface simultaneously during an SECM experiment is the application of the new technique intermittent contact-scanning electrochemical microscopy IC-SECM, introduced by McKelvey *et al*,[86] where the SECM tip is oscillated normal to the substrate surface, and approached towards the sample. The change in the oscillation amplitude due to the intermittent contact of the tip with the surface is used as a feedback signal to maintain a constant tip-substrate distance. Other methods used to overcome the topography convolution are the use of two types of mediators, one to track the topography and another to probe the surface reactivity,[87] or the use of impedance measurements techniques,[88,89] shear force methods,[90,91] and coupling SECM with atomic force microscopy.[92–94]

Generation/Collection Mode

In tip generation/substrate collection (TG/SC) mode,[77,95] the SECM tip is held at a specific potential so to generate an analyte by an oxidation or reduction reaction. The analyte then travels through the tip-substrate gap where it undergoes a reaction at the substrate interface which is also retained at a suitable potential, thus species are detected through the substrate current i_s. In substrate generation/tip collection (SG/TC) mode,[96,97] the species are produced at the sample interface, and are detected at the tip through a reaction that produces the tip current i_t (see Figure 1.8). In (TG/SC) mode, as the substrate is much larger than the tip, the efficiency of collection $i_s/i_t \sim 1$ for a one-step heterogeneous electron transfer, as the analyte that was produced at the tip diffuses to the substrate surface without escaping into bulk. However, for coupled homogeneous chemical reactions, i_t and i_s have very different values. In the case of a slow competitive reaction that converts the species of interest into an electroinactive form, diffusion is dominant, and the efficiency of collection i_s/i_t increases as the probe approaches the surface with a value ~ 1 at close tip-substrate distance. Nevertheless, if the competitive reaction is fast, resulting in $i_s/i_t \sim 0$, as the analyte undergoes the reaction to turn into an electroinactive form before reaching the surface.[83,98−101]

Penetration Mode

In this mode a micro to nano-meter size electrode is used to penetrate a soft microstructure medium (such as a polymer film) that is loaded with an active mediator to extract spatially resolved information about concentrations, kinetics, mass transport and diffusion coefficients. Once the tip is in the media and far from the insulator or conductor base substrate, solid-state voltammetry can be performed similarly to the conventional measurements in solution. The tip current increases or decreases while approaching the underlying surface depending on the reactiv-

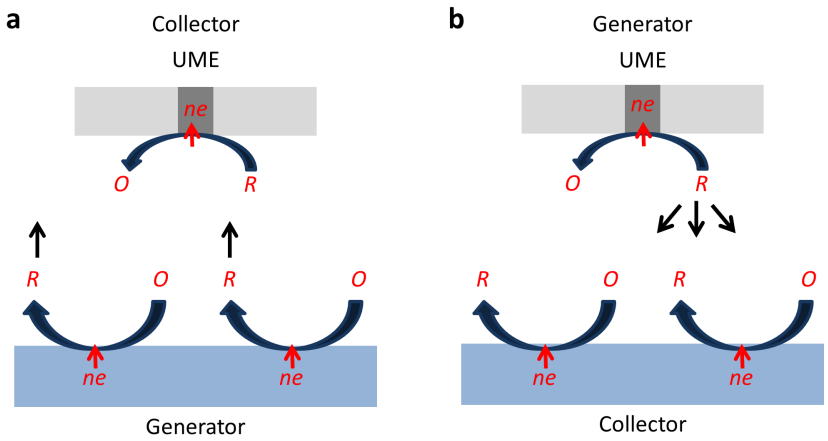

Figure 1.8: a) Substrate generation/tip collection mode where species are reduced at the sample surface then diffuse towards the tip to be oxidised. b) Tip generation/substrate collection mode where species are generated at the tip surface and collected at the substrate interface.

ity of the substrate. Approach curves are similar to the ones recorded in solution if the film is homogeneous and not very resistive.[102,103] This technique has been used to study biological systems, such as intact nuclei,[104] giant liposomes,[105] and mammalian cells.[106]

Ion Transfer Feedback and Electron Transfer at the liquid/liquid Interface

The probing of heterogeneous electron transfer (ET) reactions at the interface between two immiscible electrolyte solutions (ITIES) is of great importance for many biological and technological systems. The SECM approach to probing this type of problems is similar to studies at the liquid/solid interface.[80,107] The SECM probe is positioned in the upper solution (organic), which contains one form of the redox species,(*e.g.,* R_1), the tip is held at a sufficiently positive potential to drive the oxidation reaction to produce O_1. Once the probe is positioned at close proximity to the ITIES, the mediator is regenerated through the reaction between the oxidised form O_1 at the organic phase and the reduced form of the mediator at the aqueous phase R_2:

$$O_1 + R_2 \rightarrow R_1 + O_2 \tag{1.16}$$

Thus, the tip current increases while approaching the interface (positive feedback), and this enables the extraction of reaction kinetics from the approach curves.[108]

The ion-transfer feedback mode can be used to probe the transfer of electroinactive ion species (such as K^+,[109] Na^+ and Li^+,[110] ClO_4^- and NO_3^-,[111]...) across the ITIES. This mode employs a micrometer or a nanometer size pipette filled with an electrolyte solution, that is immiscible with the bulk solution, as the working probe. The ion transfer at the ITIES that produces the tip current and the feedback, could be facilitated[109] or unassisted.[112]

In SECM experiments, the concentrations of the potential-determining ion provides a constant driving force for either electron transfer or ion-transfer processes at the nonpolarisable ITIES. Alternatively, an external bias is applied between the two phases for a polarizable ITIES to provide wider potential windows for studying electron transfer and ion transfer. The applied bias should be in the polarisation window to prevent current flow in the macroscopic liquid/liquid interface.[113,114]

1.3.2 Scanning Ion Conductance Microscopy (SICM)

In ion conductance microscopy, the probe is a pulled-glass pipette filled with electrolyte solution where a quasi reference/counter electrode (QRCE) is inserted within. The sample is immersed in electrolyte solution, and a bias is applied between the QRCE in the probe and the QRCE in solution, the flowing ionic current is measured.[115] Upon approaching an inert surface, the current decreases due to blocking of ion diffusion towards the tip opening. The direct current (DC) value can be used as a feedback signal for the DC mode, where the probe approaches the surface until a decrease in response of typically $\sim$ 0.2 - 3% of the bulk current is detected.[3]

The tip is then stopped before touching the sample, which makes it a very attractive technique to image soft surfaces such as biological samples.[116] Nevertheless, the DC bulk value could change due to thermal drift, tip partial blockage and changes in polarized QRCEs, causing less stability in the feedback mechanism.

Distance modulation (DM)-SICM

An AC component can be introduced to the ion current through distance modulation of the probe position while scanning the sample,[117,118] the changes in AC amplitude due to tip-surface distance variation is much sharper than DC changes, thus providing higher sensitivity for tracking topography (Figure 1.9a). However, the response time of the feedback is limited to the frequency of the probe oscillation, and the physical movement of the tip could cause convective fluid movements around the probe.

Bias modulation (BM)-SICM

A new mode was proposed recently where the AC current component could be generated through the application of bias modulation,[119] This is achieved by applying a sinusoidal potential signal between the QRCE in bulk and the one in the probe (Figure 1.9b). Both the AC amplitude and the phase signals can be used as feedback set points for the probe positioning. The oscillating bias can be applied around 0 V, which eliminates net ion current flow, and insures the minimization of QRCEs polarization and electro-osmotic effects.

1.3.3 Scanning Electrochemical Cell Microscopy (SECCM)

The probe in this technique is a theta glass pipette that is pulled to a fine end (typically nano to micrometer diameter). Both barrels are filled with electrolyte solution and a QRCE is inserted in each of them. A bias is applied between the two electrodes, where an ion current flows through a small meniscus that forms at the

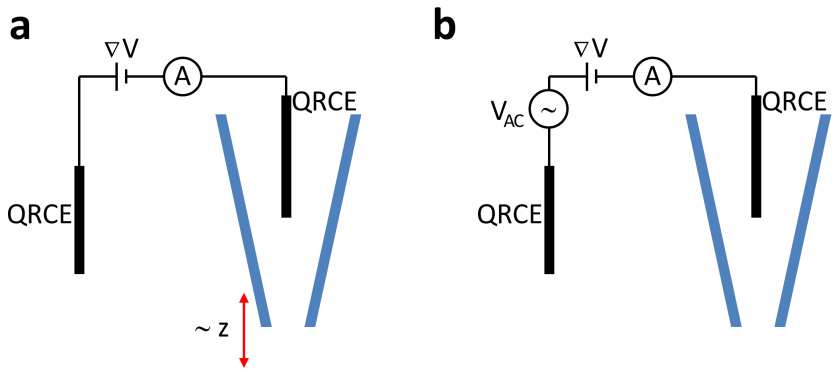

Figure 1.9: a) Distance modulated scanning ion conductance microscopy setup (DM-SICM). b) Bias modulated scanning ion conductance microscopy setup (BM-SICM)

end of the probe.[120–122] The sample in this technique is not immersed in solution, and the probe is physically oscillated to generate an AC current component. The ion current value when the meniscus is suspended in air is very small (~ 0) as the meniscus is well confined. Once the probe approaches the substrate, and the meniscus is in contact with the surface, it suffers periodic and reversible deformation due to the positional oscillation. This causes a sudden increase in the AC current, as the change in the meniscus size has a great effect on the resistivity of the circuit. Thus, the tip-surface distance could be maintained by maintaining the AC set point. Furthermore, the DC current can now be used to extract information relating to the surface characteristics and activity,[122] conductive and semi-conductive samples could also be used as working electrodes, through the application of a potential (Figure 1.10).

1.3.4 Ion Selective Electrodes (ISEs)

The ion selective electrode employs a probe with the ability to convert the activity of a specific ion in the solution into an electric potential that is measured against a reference electrode.[2,3] Their functionality is based on the transport of the selected ion from one phase (the solution) into another phase (the electrode), causing a potential difference. The relationship between the measured potential and the ion

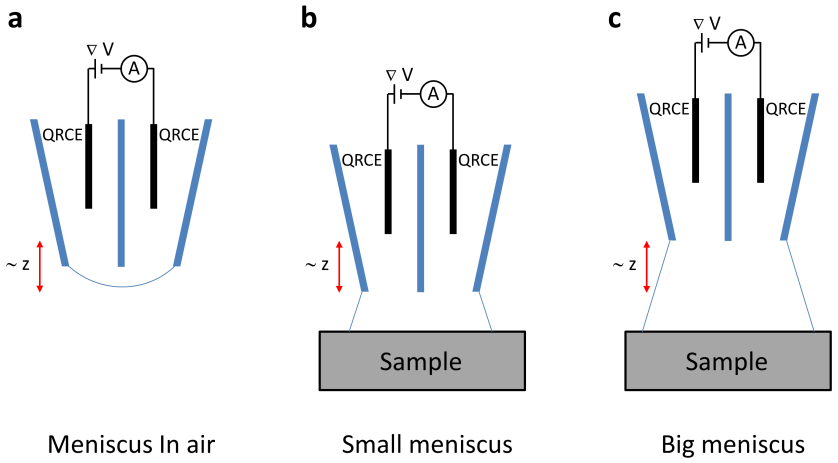

Figure 1.10: a)SECCM tip in air, where the meniscus is confined. b) The meniscus making contact with the surface at the closest distance of the z-position oscillation. c) The meniscus deformation at the highest distance of the z-position oscillation.

activity is described by Nernst equation:

$$E_m = -\frac{RT}{z_i F} ln \frac{\alpha_i^\beta}{\alpha_i^\alpha} \tag{1.17}$$

where β is the electrode phase, and α is the solution phase. The electrode phase in ISEs could be a glass membrane, an inorganic salt solid membrane or an ion exchange membrane. This electrode setup detects the ion activity but does not sense the sample surface, thus positioning of the probe presents a challenge, and another technique should be introduced to provide positioning capabilities.

1.4 Confocal Laser Scanning Microscopy (CLSM)

CLSM[123,124] is an optical microscopy technique where a specimen is scanned point by point using a laser beam, the image of is then reconstructed by a computer software to build 2D or 3D profile of the specimen.[125,126] The advantage of this type of scanning is the generation of in focus images for each scanned plane. In CLSM, the laser beam passes from the light source through an aperture, to be focused by an objective lens into a focal point on the specimen. The generated signal (reflected,

scattered or fluorescent light) then travels through a pinhole to minimise the out of focus light before reaching the detector (Figure 1.11).

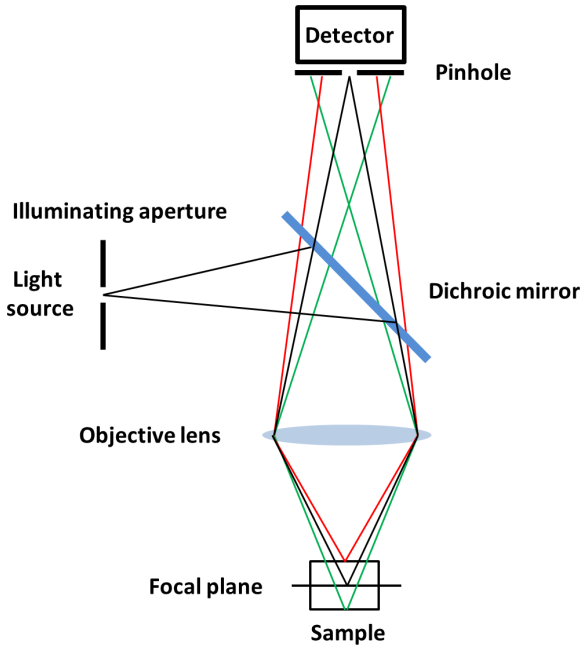

Figure 1.11: A schematic of the confocal microscope.

Fluorescence confocal microscopy employs either a fluorophore solution or fluorophore tagged-sample, which is exited at a certain wavelength by the laser beam. The emitted signal is usually of a different wavelength and is filtered prior to detection. CLSM has a wide application in analytical, biological and medical sciences.

1.5 Crystal Dissolution

The driving force behind the crystal dissolution is the undersaturation of the solution, which is defined by the following equation:

$$S = \frac{IP}{K_{sp}} \tag{1.18}$$

where IP is the ionic product of the crystal ions in solution, and K_{sp} is the solubility product. Crystal dissolution is believed to involve two basic processes: surface processes, which include the detachment of dissolution units from kinks and steps, the movement of units on the surface, and the solvation of the ions in aqueous solutions; and the mass transport process where the dissolution units diffuse through the parent phase by diffusion, convection or migration to bulk solution as illustrated in Figure 1.12. Accordingly, depending on the slowest process, the dissolution could be either mass-transport controlled, surface-controlled, or under mixed control.[127]

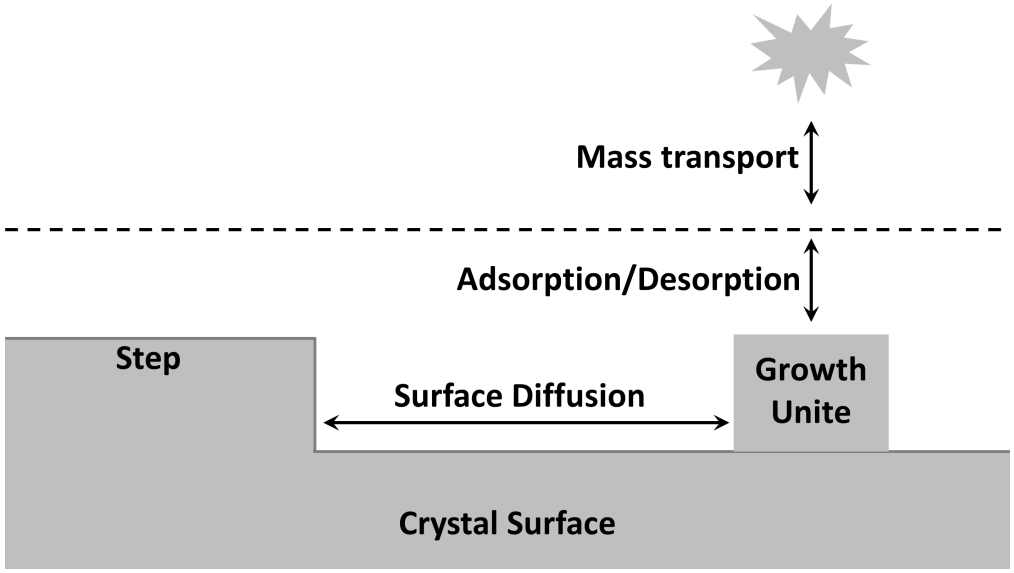

Figure 1.12: Schematic of crystal dissolution surface and mass transport processes.

1.5.1 Calcite Dissolution

The dissolution of crystals occurs when the surrounding solution is under saturated, (S<1). For the case of calcite, the dissolution is pH dependent, at low pH values the protons attack the crystal surface directly in what is called acid induced dissolution, the following equations summaries the kinetics of the dissolution reaction taking place in this case:[128]

$$CaCO_{3(s)} + H^{+}_{(aq)} \rightleftharpoons Ca^{2+}_{(aq)} + HCO^{-}_{3(aq)} \tag{1.19}$$

$$HCO^{-}_{3(aq)} + H^{+}_{(aq)} \rightleftharpoons H_2CO_{3(aq)} \rightleftharpoons CO_{2(g)} + H_2O_{(l)} \tag{1.20}$$

At higher pH values, the reaction of water with calcium carbonate dominates, which is a much slower process:[129]

$$CaCO_{3(s)} + H_2O_{(l)} \rightleftharpoons Ca^{2+}_{(aq)} + HCO^{-}_{3(aq)} + OH^{-}_{(aq)} \tag{1.21}$$

1.5.2 Dental enamel

Enamel is the visible part of a tooth that is covering the crown. It is made up of > 95% calcium hydroxyapatite (HAP), with the rest being water, organic material and other minerals.[130,131] The enamel composition varies a lot between people, due to nature and environmental aspects.[132] Enamel is one of the hardest materials in the human body,[133] where the saliva can perform remineralisation and acts as a buffer to help protect it, as it contains calcium and phosphate ions.[134]

Enamel dissolution

As in any type of crystal, the HAP dissolution driving force is mainly the undersaturation of the solution. The solubility of HAP increases at lower pH values as a result of the decrease of the ionic product ($IP_{HAP} = [Ca^{2+}]^{10}\ \ [PO^{3-}_4]^6\ \ [OH^-]^2$). The dissolution of enamel is called demineralisation, where the HAP is attacked by acid present in food and drinks. The following equation describes the acid induced dissolution reaction:[131]

$$Ca_{10}(PO_4)_6(OH)_{2\ (s)} + 8H^{+}_{(aq)} \rightleftharpoons 10Ca^{2+}_{(aq)} + 6HPO^{2-}_{4(aq)} + 2H_2O_{(l)} \tag{1.22}$$

Fluoride is considered to be an effective treatment for enamel, as it is absorbed by the surface to form either fluorapatite or calcium di-fluoride, which help inhibiting the dissolution.[135]

1.6 Finite Element Method (FEM) Simulations

The recorded signal at a probe depends largely on the mass transport of species in solution as well as surface reactions, to analyse those measurements it is possible to acquire analytical solutions for simple geometries.[136,137] However, once the geometry gets more complicated and various processes occur in a system, it is difficult to obtain analytical solutions of equations. Thus, numerical solutions for the problem are required. The finite element method can be used to find approximate solutions for partial differential equations in the domain.[122,138] The geometry of the problem is usually divided into smaller sub-domains with specific equations associated with each of them, the Nernst-Planck equation is commonly used. Those sub-domains are then divided into small mesh elements, where a numerical solution of the partial differential equations in each element is calculated either for a steady state condition, or as a time dependent study. Solutions are evaluated and checked after calculations, to prove that they make sense and are physically possible. Herein, the finite element method software Comsol package is used.

1.6.1 Comsol Multiphysics

Comsol Multiphysics (known as FEMLAB before 2005) is a science focused commercial software, based on the *finite element method* numerical analysis simulation and solver package, for simulating physics-based problems and solving of partial differential equations (PDEs). The package is used to investigate a wide range of physics and engineering problems, especially multiphysics phenomena. With the package user interface, it is possible to take advantage of the tens of add-on products, thus

extending the platform of problem solving in electrical, mechanical, fluid flow, and chemical applications. In recent years, higher interest in the use of Comsol in the electrochemical area has been reported, due to the ability of coupling several physical phenomena through the PDEs that are incorporated in the software or manually built. The main phenomena that govern electrochemical systems are conservation of charge and current in the electrolyte and electrodes, together with the conservation of mass for each solute species in an electrolyte.[139] Prediction of a fluid flow additionally involves the conservation of momentum and total mass in a solution or mixture.[139] Thus, for a specific problem, those equations could be solved in a suitable geometry and time domain. The Comsol user friendly interface allows the build of different geometries, multiphase domains, addition of several physics, connecting those physics together, build new physics and incorporate new PDEs within the same model to achieve a representative simulation of the real experimental system.

Applications of the Comsol Multiphysics in recent research involved investigating the diffusion profile at electrode arrays for chronoamperometric measurements,[8] inlaid[10] and recessed[10,11] microdisc arrays, differential cyclic voltammetry,[13] mass transport effect on the efficiency of biosensors,[14] calcite dissolution kinetics,[15–17] electron transfer[21] and investigating substrate reactivity[22] by SECM imaging, coupling of flow and mass transport in hydrodynamic electrochemistry[23,24] natural convection effects at microdisks,[26] cyclic voltammetry[31] and stripping voltammetry[30] studies for ITIES.

1.7 Aims of this Thesis

The work presented in this thesis is focused on investigations using new analytical techniques and their application to study surface properties (charge, and dissolution kinetics). This work has involved a multidisciplinary effort combining experiments and modelling with my effort mainly on developing models that enhance experimen-

tal design and analysis.

In chapter 2, a new technique BM-SICM developed by this group is coupled with FEM modelling to investigate the surface charge density at interfaces, through probing of the diffuse double layer. A numerical finite element method model has been developed to verify the experimental results, and prove the sensitivity of the AC response to surface charge at the cyclic voltammetry measurements, and the ability to resolve topography once the bias offset is eliminated.

In chapter 3, an SECM setup is used to generate acid attack on enamel samples, while the CLSM is used to probe the proton diffusion profile near the surface, thus combining the two techniques with FEM modelling to investigate the acid dissolution kinetics of enamel, and the effect of fluoride treatment.

In chapter 4, a dual channel probe is introduced, with a SICM barrel for probe positioning and agent local delivery, and a ISME channel for ion potentiometric measurement. The probe size developed herein reached 1.5 µm (total diameter), providing very good imaging resolution. The probe was used to study the calcite dissolution at different conditions, and the FEM modelling provided a robust frame for extraction of dissolution rates.

In chapter 5 another dual channel is introduced with a SICM tip to track topography, and an iridium oxide coated carbon electrode for pH measurements. The new probe was tested by probing the pH profile around calcite microcrystals that are dissolving in an electrolyte solution under neutral pH conditions. The dissolution of calcite is known to change the local pH of the solution, and my main contribution was to develop a numerical model to extract pH profiles around the crystal to deduce dissolution fluxes.

Chapter 6 provides an SECCM acid-induced dissolution study for enamel surfaces (untreated, fluoride treated, zinc treated and a combined treatment), coupled with AFM imaging of formed itch pits. The dissolution rates for different surface treatments were extracted through a FEM model that I developed.

1.8 References

(1) Fisher, A. C. *Electrode Dynamics*; Oxford University Press, 1996.

(2) Bard, A. J.; Faulkner, L. R. *Electrochemical Methods: Fundamentals and Applications*; Wiley, 2000.

(3) Brett, C. M. A.; Brett, A. M. O. *Electrochemistry: Principles, Methods, and Applications*; Oxford University Press, 1993. (4) Stern, O. *Elektrochem.* **1924**, 30, 508-516.

(5) Grahame, D. C. *Chem. Rev.* **1947**, 41, 441-501.

(6) Amatore, C.; Pebay, C. c.; Thouin, L.; Wang, A.; Warkocz, J. *Anal. Chem.* **2010**, 82, 6933-6939.

(7) Forster, R. J. *Chemical Society Reviews* **1994**, 23, 289-297.

(8) Bard, A. J.; Stratmann, M.; Unwin, P. *Encyclopedia of Electrochemistry volume 3: Instrumentation and Electroanalytical Chemistry*; Wiley-VCh, 2003.

(9) Wightman, R. M. *Science* **1988**, 240, 415-420.

(10) MacFarlane, D.; Wong, D. *J. Electroanal. Chem. Interfacial Electrochem.* **1985**, 185, 197-202.

(11) Fleischmann, M.; Bandyopadhyay, S.; Pons, S. *J. Phys. Chem.* **1985**, 89, 5537-5541.

(12) Wehmeyer, K. R.; Deakin, M. R.; Wightman, R. M. *Anal. Chem.* **1985**, 57, 1913-1916.

(13) Shea, T. V.; Bard, A. J. *Anal. Chem.* **1987**, 59, 2101-2111.

(14) Fosdick, L. E.; Anderson, J. L.; Baginski, T. A.; Jaeger, R. C. *Anal. Chem.* **1986**, 58, 2750-2756.

(15) Ciszkowska, M.; Stojek, Z. *J. Electroanal. Chem. Interfacial Electrochem.* **1985**, 191, 101-110.

(16) Baldo, M. A.; Daniele, S.; Corbetta, M.; Mazzocchin, G. A. *Electroanalysis* **1995**, 7, 980-986.

(17) Ponchon, J. L.; Cespuglio, R.; Gonon, F.; Jouvet, M.; Pujol, J. F. *Anal. Chem.* **1979**, 51, 1483-1486.

(18) Dayton, M.; Brown, J.; Stutts, K.; Wightman, R. *Anal. Chem.* **1980**, 52, 946-950.

(19) Wightman, R. M.; Wipf, D. O. *Electroanal. Chem.* **1989**, 15, 267-353.

(20) Zoski, C. G. *Electroanalysis* **2002**, 14, 1041-1051.

(21) Heinze, J. *Angew. Chem., Int. Ed. Engl.* in English **1993**, 32, 1268-1288.

(22) Bindra, P.; Brown, A.; Fleischmann, M.; Pletcher, D. *J. Electroanal. Chem. Interfacial Electrochem.* **1975**, 58, 39-50. (23) Crank, J. *The Mathematics of Diffusion*, 2nd edition ed.; Oxford University Press 1975. (24) Bard, A. J.; Mirkin, M. V.; Unwin, P. R.; Wipf, D. O. *J. Phys. Chem.* **1992**, 96, 1861-1868.

(25) Aoki, K. *Electroanalysis* **1993**, 5, 627-639.

(26) Zoski, C. G.; Liu, B.; Bard, A. J. *Anal. Chem.* **2004**, 76, 3646-3654.

(27) Williams, C. G. *Development and application of imaging techniques for the investigation of dentinal hypersensitivity.* PhD, University of Warwick, UK, 2008.

(28) Howell, J. O.; Wightman, R. M. *Anal. Chem.* **1984**, 56, 524-529.

(29) Fischer, A. *Electrode dynamics*; Oxford Univ. Press, 2003.

(30) Bond, A.; Fleischmann, M.; Robinson, J. *J. Electroanal. Chem. Interfacial Electrochem.* **1984**, 168, 299-312.

(31) Bitziou, E. *Development and Applications of Microelectrodes in Hydrodynamic and Photoelectrochemical Systems.* PhD, University of Warwick, UK,2006.

(32) Wightman, R. M. *Anal. Chem.* **1981**, 53, 1125A-1134A.

(33) Roitman, M. F.; Stuber, G. D.; Phillips, P. E.; Wightman, R. M.; Carelli, R. M. *J. Neurosci.* **2004**, 24, 1265-1271.

(34) Heien, M. L.; Khan, A. S.; Ariansen, J. L.; Cheer, J. F.; Phillips, P. E.; Wassum, K. M.; Wightman, R. M. *Proc. Natl. Acad. Sci. U. S. A.* **2005**, 102, 10023-10028.

(35) Zoski, C. G. *Electroanalysis* **2002**, 14, 1041-1051.

(36) Danis, L.; Polcari, D.; Kwan, A.; Gateman, S. M.; Mauzeroll, J. *Anal. Chem.*

2015, 87, 2565-2569.

(37) Amatore, C.; Collignon, M. G.; Lemaitre, F. *Electrochemical Detection of Exocytosis: A Survey from the Earliest Amperometry at Carbon Fiber Ultramicroelectrodes to Recent Integrated Systems*, 2015.

(38) Mishra, D.; Harrison, N. R.; Gonzales, C. B.; Schilström, B.; Konradsson-Geuken, A. *PLOS ONE* **2015**.

(39) Andrade, F. J.; Blondeau, P.; Macho, S.; Riu, J.; Rius, F. X. *Nanomater. Electrochem. Sens. Biosens.* **2014**, 169.

(40) Spano, N.; Guccini, V.; Ciulu, M.; Floris, I.; Nurchi, V. M.; Panzanelli, A.; Pilo, M. I.; Sanna, G. *Arabian J. Chem.* **2015**.

(41) Meng, Y.; Bard, A. J. *Anal. Chem.* **2015**, 87, 3498-3504.

(42) Zhu, L.; Xu, L.; Huang, B.; Jia, N.; Tan, L.; Yao, S. *Electrochim. Acta* **2014**, 115, 471-477.

(43) Erden, P. E.; Kilic, E. *Talanta* **2013**, 107, 312-323.

(44) Migheli, R.; Puggioni, G.; Dedola, S.; Rocchitta, G.; Calia, G.; Bazzu, G.; Esposito, G.; Lowry, J. P.; O'Neill, R. D.; Desole, M. S. *Anal. Biochem.* **2008**, 380, 323-330.

(45) Quintino, M. d. S. M.; Corbo, D.; Bertotti, M.; Angnes, L. *Talanta* **2002**, 58, 943-949.

(46) Golovko, D. A.; Sharma, V. K.; Pavlova, O. V.; Belyanovskaya, E. A.; Golovko, I. D.; Suprunovich, V. I.; Zboril, R. *Cent. Eur. J. Chem.* **2011**, 9, 808-812.

(47) Langyan, R.; Khatkar, S. *Asian J. Chem.* **2013**, 25, 1376.

(48) Rashid, M.; Khan, F.; Wahab, R. *Ind. Eng. Chem. Res.* **2014**, 53, 14897-14903.

(49) Ali, T. A.; Mohamed, G. G.; Azzam, E.; Abd-elaal, A. A. *Sens. Actuators, B* **2014**, 191, 192-203.

(50) Werner, C. F. 2014.

(51) Banica, F.-G. *Chemical sensors and biosensors: fundamentals and applications*;

John Wiley & Sons, 2012.

(52) Moya, A.; Zine, N.; Illa, X.; Prats-Alfonso, E.; Gabriel, G.; Errachid, A.; Villa, R. *Procedia Eng.* **2014**, 87, 276-279.

(53) Norouzi, P.; Gupta, V. K.; Larijani, B.; Ganjali, M. R.; Faridbod, F. *Talanta* **2014**, 127, 94-99.

(54) Strycharz, S. M.; Malanoski, A. P.; Snider, R. M.; Yi, H.; Lovley, D. R.; Tender, L. M. *Energy Environ. Sci.* **2011**, 4, 896-913.

(55) Harnisch, F.; Freguia, S. *Chem Asian J* **2012**, 7, 466-475.

(56) Arteaga, J. F.; Ruiz-Montoya, M.; Palma, A.; Alonso-Garrido, G.; Pintado, S.; Rodriguez-Mellado, J. M. *Molecules* **2012**, 17, 5126-5138.

(57) Nicholson, R. S. *Anal. Chem.* **1965**, 37, 1351-1355.

(58) Mandal, A. B.; Nair, B. U. *J. Phys. Chem.* **1991**, 95, 9008-9013.

(59) Wang, J. *Stripping analysis: Principles, instrumentation, and applications*; Vch Pub, 1985.

(60) Wang, J.; Lu, J.; Hocevar, S. B.; Farias, P. A.; Ogorevc, B. *Anal. Chem.* **2000**, 72, 3218-3222.

(61) Martiniano, L. C.; Abrantes, V. R.; Neto, S. Y.; Marques, E. P.; Fonseca, T. C.; Paim, L. L.; Souza, A. G.; Stradiotto, N. R.; Aucélio, R. Q.; Cavalcante, G. H. *Fuel* **2013**, 103, 1164-1167.

(62) Rue, E. L.; Bruland, K. W. *Mar. Chem.* **1995**, 50, 117-138.

(63) Abualhaija, M. M.; van den Berg, C. M. *Mar. Chem.* **2014**, 164, 60-74.

(64) Wang, J.; Hocevar, S. B.; Ogorevc, B. *Electrochem. Commun.* **2004**, 6, 176-179.

(65) Paleček, E.; Postbieglová, I. *J. Electroanal. Chem. Interfacial Electrochem.* **1986**, 214, 359-371.

(66) Gulaboski, R.; Kokoškarova, P.; Mitrev, S. *Electrochim. Acta* **2012**, 69, 86-96.

(67) Krulic, D.; Fatouros, N.; Liu, D. *J. Electroanal. Chem.* **2015**, 754, 30-39.

(68) Tian, X.; Cheng, C.; Yuan, H.; Du, J.; Xiao, D.; Xie, S.; Choi, M. M. *Talanta*

2012, 93, 79-85.

(69) Ensafi, A. A.; Karimi-Maleh, H.; Mallakpour, S. *Electroanalysis* **2012**, 24, 666-675.

(70) Lee, C. Y.; Elton, D.; Brajter-Toth, A.; Bond, A. M. *Electroanalysis* **2013**, 25, 931-944.

(71) Lee, C.-Y.; Guo, S.-X.; Murphy, A. F.; McCormac, T.; Zhang, J.; Bond, A. M.; Zhu, G.; Hill, C. L.; Geletii, Y. V. *Inorg. Chem.* **2012**, 51, 11521-11532.

(72) Meyer, E.; Hug, H. J.; Bennewitz, R. *Scanning probe microscopy: the lab on a tip*; Springer Science & Business Media, 2013.

(73) Mirkin, M. V. *Anal. Chem.* **1996**, 68, 177A-182A.

(74) Sun, P.; Laforge, F. O.; Mirkin, M. V. *Phys. Chem. Chem. Phys.* **2007**, 9, 802-823.

(75) Bard, A. J.; Fan, F. R. F.; Kwak, J.; Lev, O. *Anal. Chem.* **1989**, 61, 132-138.

(76) Kwak, J.; Bard, A. J. *Anal. Chem.* **1989**, 61, 1794-1799.

(77) Amemiya, S.; Bard, A. J.; Fan, F.-R. F.; Mirkin, M. V.; Unwin, P. R. *Annu. Rev. Anal. Chem.* **2008**, 1, 95-131.

(78) Cortés-Salazar, F.; Momotenko, D.; Girault, H. H.; Lesch, A.; Wittstock, G. *Anal. Chem.* **2011**, 83, 1493-1499.

(79) Ye, H.; Park, H. S.; Bard, A. J. *J. Phys. Chem. C* **2011**, 115, 12464-12470.

(80) Bard, A., Mirkin, MV, Eds. *Scanning Electrochemical Microscopy*; Marcel Dekker: New York, 2001.

(81) Kwak, J.; Bard, A. J. *Anal. Chem.* **1989**, 61, 1221-1227.

(82) Bard, A.; Fan, F.; Pierce, D. T.; Unwin, P. R.; Wipf, D. O.; Zhou, F. *Science* **1991**, 254, 68-74.

(83) Unwin, P. R.; Bard, A. J. *J. Phys. Chem.* **1991**, 95, 7814-7824.

(84) Pollard, A. J.; Faruqui, N.; Shaw, M.; Clifford, C. A.; Takahashi, Y.; Korchev, Y. E.; Ebejer, N.; Macpherson, J. V.; Unwin, P. R.; Roy, D. In *MRS Proceedings*; Cambridge Univ Press, 2012, pp mrsf11-1422-qq1407-1404.

(85) Etienne, M.; Schulte, A.; Schuhmann, W. *Electrochem. Commun.* **2004**, 6, 288-293.

(86) McKelvey, K.; Edwards, M. A.; Unwin, P. R. *Anal. Chem.* **2010**, 82, 6334-6337.

(87) Gonsalves, M.; Macpherson, J. V.; O'Hare, D.; Winlove, C. P.; Unwin, P. R. *Biochim. Biophys. Acta, Gen. Subj.* **2000**, 1524, 66-74.

(88) Eckhard, K.; Schuhmann, W. *Analyst* **2008**, 133, 1486-1497.

(89) Kurulugama, R. T.; Wipf, D. O.; Takacs, S. A.; Pongmayteegul, S.; Garris, P. A.; Baur, J. E. *Anal. Chem.* **2005**, 77, 1111-1117.

(90) Takahashi, Y.; Shiku, H.; Murata, T.; Yasukawa, T.; Matsue, T. *Anal. Chem.* **2009**, 81, 9674-9681.

(91) Ludwig, M.; Kranz, C.; Schuhmann, W.; Gaub, H. E. Review of scientific instruments **1995**, 66, 2857-2860.

(92) Macpherson, J. V.; Unwin, P. R. *Anal. Chem.* **2001**, 73, 550-557.

(93) Gardner, C. E.; Macpherson, J. V. *Anal. Chem.* **2002**, 74, 576 A-584 A.

(94) Macpherson, J. V.; Jones, C. E.; Barker, A. L.; Unwin, P. R. *Anal. Chem.* **2002**, 74, 1841-1848.

(95) Mirkin, M. V.; Nogala, W.; Velmurugan, J.; Wang, Y. *Phys. Chem. Chem. Phys.* **2011**, 13, 21196-21212.

(96) Martin, R. D.; Unwin, P. R. *Anal. Chem.* **1998**, 70, 276-284.

(97) Unwin, P. R.; Bard, A. J. *J. Phys. Chem.* **1992**, 96, 5035-5045.

(98) Zhou, F.; Unwin, P. R.; Bard, A. J. *J. Phys. Chem.* **1992**, 96, 4917-4924.

(99) Zhou, F.; Bard, A. J. *J. Am. Chem. Soc.* **1994**, 116, 393-394.

(100) Treichel, D. A.; Mirkin, M. V.; Bard, A. J. *J. Phys. Chem.* **1994**, 98, 5751-5757.

(101) Demaille, C.; Unwin, P. R.; Bard, A. J. *J. Phys. Chem.* **1996**, 100, 14137-14143.

(102) Fan, F. R. F.; Mirkin, M. V.; Bard, A. J. *J. Phys. Chem.* **1994**, 98, 1475-

1481.

(103) Mirkin, M. V.; Fan, F.-R. F.; Bard, A. J. *Science* **1992**, 257, 364-366.

(104) Guo, J.; Amemiya, S. *Anal. chem.* **2005**, 77, 2147-2156.

(105) Zhan, W.; Bard, A. J. *Anal. Chem.* **2006**, 78, 726-733.

(106) Sun, P.; Laforge, F. O.; Abeyweera, T. P.; Rotenberg, S. A.; Carpino, J.; Mirkin, M. V. *Proc. Natl. Acad. Sci.* **2008**, 105, 443-448.

(107) Barker, A. L.; Gonsalves, M.; Macpherson, J. V.; Slevin, C. J.; Unwin, P. R. *Anal. Chim. Acta* **1999**, 385, 223-240.

(108) Wei, C.; Bard, A. J.; Mirkin, M. V. *J. Phys. Chem.* **1995**, 99, 16033-16042.

(109) Shao, Y.; Mirkin, M. V. *J. Electroanal. Chem.* **1997**, 439, 137-143.

(110) Li, F.; Chen, Y.; Sun, P.; Zhang, M.; Gao, Z.; Zhan, D.; Shao, Y. *J. Phys. Chem. B* **2004**, 108, 3295-3302.

(111) Quentel, F.; Mircẽski, V.; L'Her, M. *Anal. Chem.* **2005**, 77, 1940-1949.

(112) Shao, Y.; Mirkin, M. V. *J. Phys. Chem. B* **1998**, 102, 9915-9921.

(113) Zhang, Z.; Yuan, Y.; Sun, P.; Su, B.; Guo, J.; Shao, Y.; Girault, H. H. *J. Phys. Chem. B* **2002**, 106, 6713-6717.

(114) Sun, P.; Zhang, Z.; Gao, Z.; Shao, Y. *Angew. Chem., Int. Ed.* **2002**, 41, 3445-3448.

(115) Chen, C.-C.; Zhou, Y.; Baker, L. A. Annu. Rev. *Anal. Chem.* **2012**, 5, 207-228.

(116) Takahashi, Y.; Murakami, Y.; Nagamine, K.; Shiku, H.; Aoyagi, S.; Yasukawa, T.; Kanzaki, M.; Matsue, T. *Phys. Chem. Chem. Phys.* **2010**, 12, 10012-10017.

(117) Edwards, M. A.; Williams, C. G.; Whitworth, A. L.; Unwin, P. R. *Anal. Chem.* **2009**, 81, 4482-4492.

(118) Chen, C.-C.; Baker, L. A. *Analyst* **2011**, 136, 90-97.

(119) McKelvey, K.; Perry, D.; Byers, J. C.; Colburn, A. W.; Unwin, P. R. *Anal. Chem.* **2014**, 86, 3639-3646.

(120) Rodolfa, K. T.; Bruckbauer, A.; Zhou, D.; Schevchuk, A. I.; Korchev, Y. E.;

Klenerman, D. *Nano Lett.* **2006**, 6, 252-257.

(121) Ebejer, N.; Schnippering, M.; Colburn, A. W.; Edwards, M. A.; Unwin, P. R. *Anal. Chem.* **2010**, 82, 9141-9145.

(122) Kinnear, S. L.; McKelvey, K.; Snowden, M. E.; Peruffo, M.; Colburn, A. W.; Unwin, P. R. *Langmuir* **2013**, 29, 15565-15572.

(123) Sheppard, C. J.; Shotton, D. M. *Confocal laser scanning microscopy*; BIOS Scientific Publishers, 1997.

(124) Halbhuber, K.-J.; König, K. *Annals of Anatomy-Anatomischer Anzeiger* **2003**, 185, 1-20.

(125) Fiedler, S.; Hagedorn, R.; Schnelle, T.; Richter, E.; Wagner, B.; Fuhr, G. *Anal. Chem.* 1995, 67, 820-828.

(126) Amatore, C.; Bonhomme, F.; Bruneel, J.-L.; Servant, L.; Thouin, L. *J. Electroanal. Chem.* **2000**, 484, 1-17.

(127) Macpherson, J. V.; Unwin, P. R. *J. Phys. Chem.* **1995**, 99, 14824-14831.

(128) Compton, R. G.; Unwin, P. *Philos. Trans. R. Soc. London, Ser. A* **1990**, 330, 1-45.

(129) Compton, R.; Pritchard, K. *Philos. Trans. R. Soc. London, Ser. A* **1990**, 330, 47-70.

(130) Amaechi, B.; Higham, S. *J. Dent.* **2005**, 33, 243-252.

(131) Barbour, M.; Rees, J. *J. Dent.* **2004**, 32, 591-602.

(132) Browne, D.; Whelton, H.; O'Mullane, D. *J. Dent.* **2005**, 33, 177-186.

(133) Raue, L.; Klein, H. In *Solid State Phenomena*; Trans Tech Publ, 2010, pp 281-286.

(134) Anderson, P.; Hector, M.; Rampersad, M. *Int. J. Paediat. Dent.* **2001**, 11, 266-273.

(135) Holler, B.; Friedl, K.-H.; Jung, H.; Hiller, K.-A.; Schmalz, G. *Clin. Oral. Invest.* **2002**, 6, 137-144.

(136) Mirkin, M. V.; Fan, F.-R. F.; Bard, A. J. *J. Electroanal. Chem.* 1992, 328,

47-62.

(137) Cornut, R.; Griveau, S.; Lefrou, C. *J. Electroanal. Chem.* **2010**, 650, 55-61.

(138) Snowden, M. E.; Güell, A. G.; Lai, S. C. S.; McKelvey, K.; Ebejer, N.; O'Connell, M. A.; Colburn, A. W.; Unwin, P. R. *Anal. Chem.* **2012**, 84, 2483-2491.

(139) Dickinson, E. J.; Ekström, H.; Fontes, E. *Electrochem. Commun.* **2014**, 40, 71-74.

(140) Godino, N.; Borrisé, X.; Muñoz, F. X.; del Campo, F. J.; Compton, R. G. *J. Phys. Chem. C* **2009**, 113, 11119-11125.

(141) Lavacchi, A.; Bardi, U.; Borri, C.; Caporali, S.; Fossati, A.; Perissi, I. *J. Appl. Electrochem.* **2009**, 39, 2159-2163.

(142) Oleinick, A.; Zhu, F.; Yan, J.; Mao, B.; SvirâĂĽ, I.; Amatore, C. *Chem. Phys. Chem.* **2013**, 14, 1887-1898.

(143) Odijk, M.; Wiedemair, J.; van Megen, M.; Olthuis, W.; van den Berg, A. *In Sensors*, 2010 IEEE; IEEE, 2010, pp 918-922.

(144) Claussen, J. C.; Hengenius, J. B.; Wickner, M. M.; Fisher, T. S.; Umulis, D. M.; Porterfield, D. M. *J. Phys. Chem. C* **2011**, 115, 20896-20904.

(145) McGeouch, C.-A.; Edwards, M. A.; Mbogoro, M. M.; Parkinson, C.; Unwin, P. R. *Anal. Chem.* **2010**, 82, 9322-9328.

(146) McGeouch, C.-A.; Peruffo, M.; Edwards, M. A.; Bindley, L. A.; Lazenby, R. A.; Mbogoro, M. M.; McKelvey, K.; Unwin, P. R. *J. Phys. Chem. C* **2012**, 116, 14892-14899.

(147) Nadappuram, B. P.; McKelvey, K.; Al Botros, R.; Colburn, A. W.; Unwin, P. R. *Anal. Chem.* **2013**, 85, 8070-8074.

(148) Edwards, M. A.; Whitworth, A. L.; Unwin, P. R. *Anal. Chem.* **2011**, 83, 1977-1984.

(149) Zhou, Q.; Wang, Y.; Tallman, D. E.; Jensen, M. B. *J. Electrochem. Soc.* **2012**, 159, H644-H649.

(150) Santillo, M.; Ewing, A.; Heien, M. *Anal. Bioanal. Chem.* **2011**, 399, 183-190.

(151) Amatore, C.; Lemmer, C.; Perrodin, P.; Sella, C.; Thouin, L. *Electrochem. Commun.* **2011**, 13, 1459-1461.

(152) Amatore, C.; Pebay, C.; Thouin, L.; Wang, A.; Warkocz, J. S. *Anal. Chem.* **2010**, 82, 6933-6939.

(153) Ellis, J. S.; Strutwolf, J.; Arrigan, D. W. M. *Phys. Chem. Chem. Phys.* **2012**, 14, 2494-2500.

(154) Strutwolf, J.; Arrigan, D. M. *Anal. Bioanal. Chem.* **2010**, 398, 1625-1631.

Chapter 2

Simultaneous Nanoscale Surface Charge and Topographical Mapping

Perry D.; **Al Botros R.**; Momotenko D.; Kinnear S. L. and Unwin P. R.

ACS Nano 2015, in press DOI: 10.1021/acsnano.5b02095

2.1 Abstract

Nanopipettes are playing an increasingly prominent role in nanoscience, for sizing, sequencing, delivery, detection and mapping interfacial properties. Herein, the question of how to best resolve topography and surface charge effects when using a nanopipette as a probe for mapping in scanning ion conductance microscopy (SICM) is addressed. It is shown that using a bias modulated (BM) SICM scheme it is possible to map the topography faithfully, while also allowing surface charge to be estimated. This is achieved by applying zero net bias between the electrode in the SICM tip and the one in bulk solution for topographical mapping, with just a small harmonic perturbation of the potential to create an AC current for tip positioning. Then a net bias is applied, whereupon the ion conductance current becomes sensitive to surface charge. Practically this is optimally implemented in a hopping-cyclic voltammetry mode where the probe is approached at zero net bias at a series of pixels across the surface to reach a defined separation, and then a triangular potential waveform is applied and the current response is recorded. Underpinned with theoretical analysis, including finite element modelling of the DC and AC components of the ionic current flowing through the nanopipette tip, the powerful capabilities of this approach are demonstrated with the probing of interfacial acid-base equilibria and high resolution imaging of surface charge heterogeneities, simultaneously with topography, on modified substrates.

2.2 Introduction

Surface charge density plays an important role in interfacial processes and properties, and being able to probe surface charge in a simple, robust manner could find great application in mineralogy,[1−3] colloidal science,[4−7] materials science, including the study of electrode surfaces,[8] and in living systems[4,9−16] where surface

charge is known to play a key role. While zeta potential measurements[17−18] and potentiometric titrations[19−21] give important information on the charge of colloids in solutions, the charge on extended surfaces is more difficult to probe, with relatively few techniques available. Since surfaces are often characterised by both heterogeneous charge distributions and topographical features, scanning probe microscopes (SPMs), such as force microscopy (FM)[22−26] and scanning ion conductance microscopy (SICM),[27−32] are potentially attractive as a means of probing local surface charge. At the same time, because the response of these techniques depends on both topography and surface charge (and other properties) there is a wider consideration about the operation of these SPMs, and the extent to which these different effects are convoluted in the response.

This chapter describes how SICM can be used to (i) measure topography largely free from surface charge effects and (ii) how the corresponding charge on the surface can be probed semi-quantitatively. SICM uses a positionable nanopipette to examine electrolyte-substrate interfaces without requiring a direct mechanical contact with the substrate itself, making it a powerful approach for the investigation of soft (biological) samples.[27,32,33] Traditionally in SICM, a bias is applied between a quasi-reference counter electrode (QRCE) in the nanopipette tip and a second QRCE in bulk solution to generate a direct ionic current (DC). Away from the surface, the total resistance of this conductimetric cell is dominated by the contribution from the narrow tip opening. As the tip approaches the surface to within a tip diameter, the resistance contribution from the tip-to-substrate gap increases and causes the value of ionic current to drop.[27] This provides a means of monitoring the surface topography, using various schemes such as distance modulation (DM)[27,28,30,34] and the hopping (backstep) mode[32,35,36] in which a specific tip current value is used to maintain a fixed tip-surface separation during scanning. In DM-SICM, a harmonic oscillation to the vertical (z axis) position is applied and an alternating current signal (AC) is induced, the amplitude of which can be used

for positionable feedback.[27,28,30,34] Typically, under high electrolyte conditions any double layer formed at charged interfaces is considered to be compressed to an undetectable level[37] and so it has been argued that surface charge does not convolute recorded signals, enabling topography to be faithfully reproduced[29] within the framework of traditional SICM experiments.

For lower electrolyte conditions (most prominently, below 10 mM) the diffuse double layer (DDL) at charged interfaces expands further into solution, with a Debye length of a few nanometers, and even more in media with lower dielectric constants and/or lower ionic strength.[38] This effect leads to ion current rectification phenomena at nanopipette tips in bulk solution[39–41] as well as surface induced rectification,[42,43] once a nanopipette approaches towards a charged surface. Indeed, near a surface, there is a polarity-dependent current enhancement or diminution, due to the double layer at the surface modulating the transport of ions travelling through the nanopipette opening,[42,44] in contrast to the expectations of the operation of conventional SICM.[27] This phenomenon has recently been explored and used to map surface charge heterogeneities using a classical DM-SICM setup.[44] However, there are a number of issues with this technique. The mechanical oscillation of the tip in DM-SICM, limits the range of working distances achievable with the nanopipette and consequently the sensitivity and resolution. Furthermore, the high-speed motion of the probe and fluid exerts mechanical forces on the sample, which may influence its response, for example when living cells are studied. The requirement of a large bias between the two QRCEs has also been suggested to lead to fluidic instabilities which impact on the surface.[43] Finally, for smaller probes, it becomes especially difficult to separate topography and surface charge.[44]

We have recently proposed an alternative approach for positionable feedback control of nanopipettes in SICM, whereby the tip-to-substrate separation is controlled through the application of an oscillating bias between the two QRCEs to generate an AC signal.[45] It has been demonstrated that at high electrolyte con-

centrations, bias modulated (BM)-SICM provides a stable feedback for tracking surface topography with oscillation around 0 V between the two QRCEs, at a range of frequencies using either the AC amplitude or AC phase signals. In this paper, we reveal the capabilities of BM-SICM for accurate tracing of the surface topography at charged substrates, at low electrolyte concentrations, by minimising (virtually eliminating) polarity dependent effects of surface charge in the conductimetric response. Moreover, we further highlight the possibility of probing and mapping unevenly distributed charge at interfaces by sensing of the local ionic environment within a double layer. This is achieved through the use of a hopping approach and CV measurement at each pixel in an image, with certain biases between the two QRCEs shown to highlight surface charge in a sensitive manner while, for others, the current response is insensitive to the surface charge, thus revealing only the topography with high precision. With the aid of finite element method (FEM) modelling, we verify the experimental observations and demonstrate the sensitivity of the AC voltammetric response to the double layer and charge at target surfaces. As well as independent and simultaneous topographical and surface charge imaging, this work provides a robust platform for future local nanoscale impedance experiments.

2.3 Materials and Methods

2.3.1 Solutions

Milli-Q reagent grade water (resistivity *ca.* 18.2 MΩ cm at 25° C) was used for all solutions. For the BM-SICM approach curve measurements to glass, impedance studies and BM-SICM imaging, 10 mM KCl (Sigma-Aldrich, pH 6.5) solutions were prepared. To produce the polystyrene-glass substrate for imaging, polystyrene (Sigma-Aldrich) was dissolved in chloroform (Fisher Scientific) giving a solution (0.66 mg mL^{-1}) into which a glass slide was dip-coated (30 s) to create a polystyrene film. A solution of 3-aminopropyl triethoxysilane (APTES, Sigma Aldrich) in toluene

(2 µL mL^{-1}) was used for glass surface modification for some experiments (dip-coated for 5 min). All impedance measurements and approach curve studies carried out on APTES samples were done in a slightly acidic solution of HCl (pH 3.4, Fisher Scientific) and KCl (9 mM). Solutions with varying ratios of KCl to HCl (keeping 10 mM constant ionic strength) were used to explore the effect of pH on the surface charge of glass. Approach curve measurements were also carried out towards glass in 1 - 100 mM KCl solutions to test the limits at which surface charge effects could be observed.

2.3.2 Nanopipettes

Nanopipettes (∼75 nm radius, inner taper angle 2.5 - 3.5°, dimensions measured with a Zeiss Supra55VP field emission scanning electron microscope) were pulled from borosilicate glass capillaries (o.d. 1.2 mm, i.d. 0.69 mm, Harvard Apparatus) using a laser puller (P-2000, Sutter Instruments; pulling parameters: Line 1: Heat 330, Fil 3, Vel 30, Del 220, Pul -, Line 2: Heat 330, Fil 3, Vel 40, Del 180, Pul 120). We deliberately chose to use a relatively large tip to produce a well-defined probe that was easily characterised. Although surface charge effects would be expected to be less prominent than on smaller tips;[42,44] they are still shown to be significant with major implications for nanoscale SICM imaging as we discuss herein.

2.3.3 Substrates

Glass bottomed petri dishes with detachable cover slips (3512, WillcoWells) were used as glass samples, either as received, after sonication in acetone (10 min), sonication in water (10 min) and plasma ashing in oxygen (1 min, 100 W), or after functionalisation with either polystyrene or APTES. The polystyrene samples were dip coated to produce a heterogeneous thin neutral polystyrene film with exposed negatively charged glass regions, under the condition of the measurements (aerated, unbuffered, 10 mM KCl, pH 6.5).

2.3.4 Instrumentation

The basic instrumentation has been described elsewhere.[45,67] Briefly, movement of the SICM probe in the direction normal to the substrate was controlled using a piezoelectric positioning stage of range 38 µm (P-753-3CD, Physik Intrumente) with lateral movement of the substrate controlled using a two-axis piezoelectric positioning system with a range of 300 µm (Nano-BioS300, Mad City Labs Inc.) The current-to-voltage converter used to measure currents was custom built. A lock-in amplifier (SR830, Stanford Research Systems) was used to generate the oscillating signal for BM-SICM approaches and to extract the phase and amplitude of the AC ion current. Data recording, as well as the probe position and voltage output control, was performed using a custom written LabVIEW (2013, National Instruments) program through an FPGA card (7852R, National Instruments). Impedance measurements were carried out using a Gamry Femtostat (FAS2-38039), with spectra acquired using Gamry Framework Data Acquisition Software (6.04).

2.3.5 Bias Modulated-Scanning Ion Conductance Microscopy Approaches

An oscillating bias (10 mV rms amplitude, 270 Hz) was applied between the two QRCEs about mean biases of -0.3 V, 0 V and +0.3 V. All potentials quoted herein refer to the potential of the QRCE inside of the nanopipette with respect to the bulk QRCE. Nanopipettes were approached towards glass and APTES-coated substrates at 10 nm s^{-1} and the DC, AC phase and AC amplitude of the ionic current were recorded simultaneously. Approaches towards glass were also carried out in 10 mM electrolyte concentration with the pH varying between 2.1 (10 mM HCl) and 6.5 (10 mM KCl) to vary the surface charge on the glass substrate.

2.3.6 Bias Modulated-Scanning Ion Conductance Microscopy Imaging

BM-SICM images were acquired with a positionable nanopipette in a hopping mode, while applying a small oscillation to the bias (10 mV rms amplitude, 270 Hz) about 0 V. In this mode, the probe was translated towards the surface at each image pixel at 700 nm s^{-1} until the surface was detected through a 0.5° increase in the AC phase signal. The piezo height at this point was used to generate topographical maps (as under these conditions the SICM response was relatively insensitive to the surface charge effects; vide infra). The bias between the QRCEs was then swept linearly up to +0.4 V reversed to -0.4 V and finally returned to 0 V at a rate of 1 V s^{-1}, and the AC phase and DC recorded, enabling polarity-dependent surface charge mapping. As well as movies of SICM response vs. applied potential (presented over the range -0.4 V to +0.4 V), representative maps at specific potentials as an average of several maps over potentials within ±5 mV of the stated bias value were extracted, by taking average values of the AC and DC response for each pixel in the map.

2.3.7 Atomic Force Microscopy

Contact mode atomic force microscopy (AFM) (Catalyst, Bruker-Nano), using silicon tips on a nitride lever (SNL-10, Veeco), was employed for the analysis of sample substrates.

2.4 FEM Simulations

A two-dimensional axisymmetric finite element method (FEM) model was constructed to mimic a nanopipette in bulk and in the vicinity of a charged surface (with a varying tip-to-substrate separation distance).

2.4.1 Model Description

A schematic representation (not to scale) of the two-dimensional axisymmetric (FEM) model is depicted in Figure 2.1, showing the tip of a nanopipette, with $r_0 = 75$ nm radius, with a half-cone angle $\alpha = 2.3°$ and wall thickness $w = 50$ nm (similar to that used herein) for all simulations. The geometrical parameters of the nanopipette probe were extracted from corresponding SEM images (see Figure 2.1 b). In order to eliminate effects of the domain size on the numerical results, a relatively large section of the pipette (200 µm long) was simulated in a square domain (160 µm × 160 µm) of the axisymmetric geometry representing solution bulk.

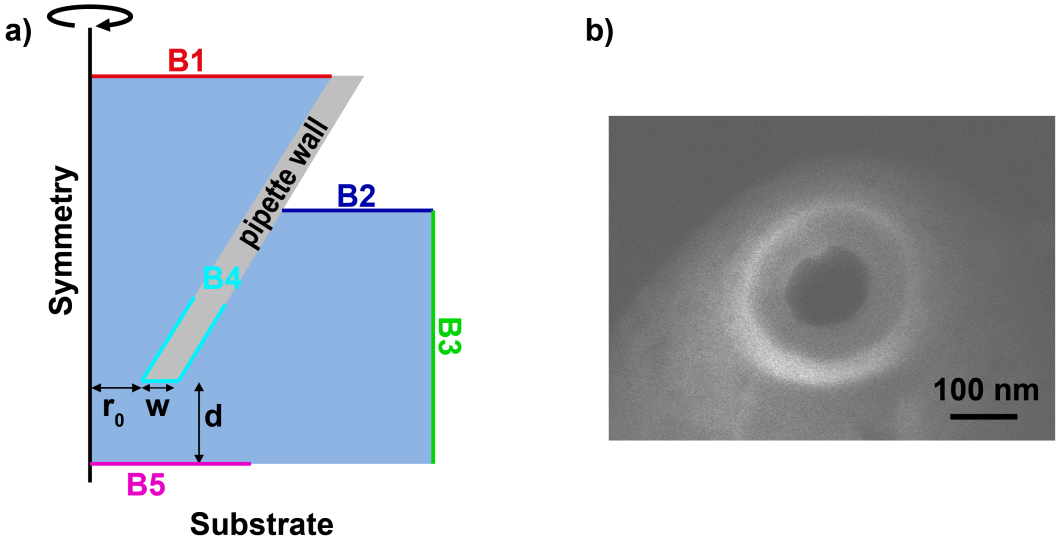

Figure 2.1: a) Representation of the 2D axisymmetric FEM model of a nanopipette at a distance, d, from a substrate. b) SEM micrograph showing the end of a typical nanopipette probe.

The numerical model was constructed in the Comsol Multiphysics (v4.4) software package, using the *Transport of diluted species* and *Electrostatics*, with harmonic bias perturbation boundary conditions to simulate the AC behavior of BM-SICM setup. Electrical properties of the bulk materials, water and borosilicate glass, were simulated through their respective dielectric constants (78 and 4.7, re-

spectively). The electrostatic charge on the nanopipette walls was assumed to be constant in the simulations, with a surface charge density value of -1.125 mC m^{-2} as in previous work,[40,42,44] while the charge on the substrate was varied. The set of boundary conditions is summarised in Table 2.1.

Table 2.1: Summarised boundary conditions for the FEM model.

Boundary	**Concentration condition**	**Potential/ charge condition**
B1	$c_i = c_{0,i}$	$V = V_{DC} + V_{AC}$
B2	$J_i = 0$	$V = 0$
B3	$c_i = c_{0,i}$	$V = 0$
B4	$J_i = 0$	σ = -1.125 mC m^{-2}
B5	$J_i = 0$	$\sigma = \sigma_{substrate}$

The equivalent circuit that represents the used electrochemical cell is illustrated in Figure 2.2a, where R_b is the total resistance of the electrolyte solution inside and outside the nanopipette. R_{tip} is the resistance arising of the tip opening and the tip-surface separation. C_{tip} is the capacitance across the nanopipette glass walls. The current tends to flow through the tip's resistance component of the parallel RC at low frequencies (less than 500 Hz), and through both capacitance and resistance components at moderate frequencies, while at high frequencies it flows through the capacitance (see Figure 2.2b-d).

2.4.2 Impedance Measurements

To ensure adequacy of the numerical description of both the DC and AC characteristics of the system, the simulation results were compared to experimental impedance measurements of the nanopipette suspended in bulk solution.

Impedance spectra at different frequencies (0.1 Hz - 100 kHz) were acquired, with 9 points per decade, in 10 mM KCl solutions in a two-electrode cell configuration. The Gamry Femtostat was connected between the two QRCEs: one in the nanopipette and one in bulk solution. Impedance measurements were performed with a 10 mV rms oscillation around 0 V mean bias. As evident from Figure 2.3a

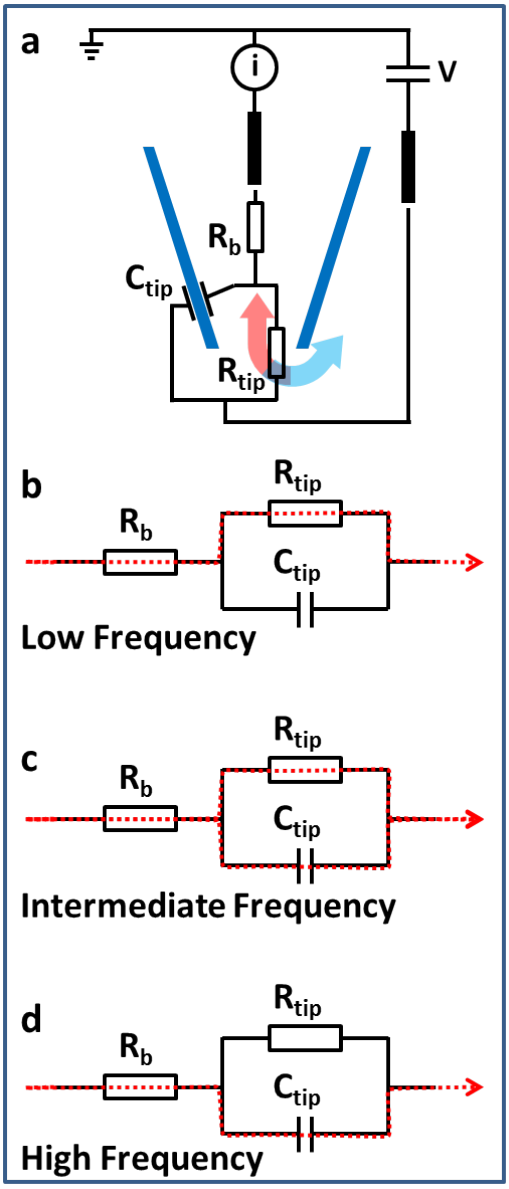

Figure 2.2: a) Schematic of the equivalent electrical circuit (a parallel RC component in series with a resistor), with the current flow paths at b) low, c) intermediate, and d) high frequencies.

and b, depicting experimental and theoretical Nyquist and Bode plots, experimental measurements are very well correlated with predictions from numerical modelling.

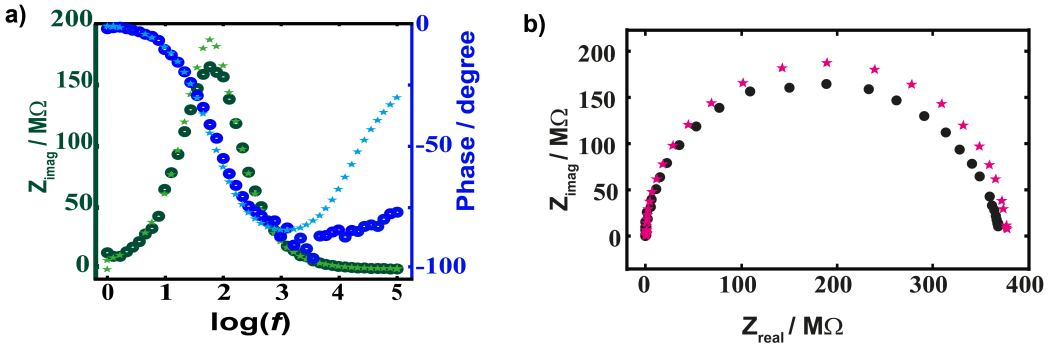

Figure 2.3: Comparison between experimental (stars) and FEM calculated impedance response of the nanopipette (circles), in the form of Bode (a) and Nyqueist (b) plots. Note that the axes in (a) are colored on the graph on the Bode plots in accordance with the graph line colors.

2.5 Results and Discussion

2.5.1 Bias Modulated-SICM as an Ion-Sensing Probe of Double Layers

An uncompensated surface charge in electrolyte solutions leads to the formation of a diffuse double layer, consisting of co- and counterions that balance the charge. The approach herein is to probe the ionic atmosphere of the double layer electrochemically (conductimetrically) with a nanopipette and derive surface charge information. At low electrolyte concentrations, glass (or quartz) nanopipettes with small tip openings exhibit perm-selectivity[39,40] towards counter ions of the DDL, that have enhanced concentration near the charged nanopipette walls. In combination with asymmetric mass-transport rates inside and outside nanopipettes (taking into account the geometrical configuration of the probe) the absolute value of ionic current driven through the opening becomes polarity dependent and this diode-like behavior is known as ion current rectification (ICR).[39−41,46,47]

When a nanopipette approaches a charged surface, the rectifying characteristics of the probe can be modified due to the presence of the DDL at the surface.[42,44] As a result, the surface-induced rectification contributes significantly to the overall

mass-transport properties of the nanopipette and, in principle, this effect can be employed for probing and mapping surface charge.[44] However, as mentioned in the introduction, the DC or AC components of ionic current, are also distance-dependent and this presents a conundrum as to how to separate charge and distance effects in the conventional DM-SICM scheme. Essentially in DM-SICM the ionic current driven through the nanopipette cannot necessarily be reliably employed for either task - probing the surface charge or tracking the topography.[44] For surfaces with large topographical features and relatively low surface charge densities, the implications of this may not be noticeable,[44] but as the resolution of the technique is advanced with smaller nanopipettes being utilised and smaller topographical features being probed,[36,48] the resulting effects of surface charge heterogeneities on the DM-SICM feedback, may become much more apparent.

Herein, we present an elegant way to resolve both surface topography and charge by using BM-SICM (Figure 2.4a). In a BM-SICM configuration, a small harmonic oscillation of potential is applied to induce an AC ionic current component, which can be used for vertical probe positioning even in the absence of mean bias applied between two QRCEs.[45] Additionally, by applying an additional bias, $\triangle V$, we show herein that one can control the extent to which the SICM current response is sensitive (or not) to surface charge. In essence for $\triangle V = 0$, the BM-SICM response faithfully maps topography (Figure 2.4b), due to minimal surface induced rectification about 0 V, while for $\triangle V \neq 0$ the SICM response becomes surface charge sensitive. Note that by maintaining $\triangle V = 0$ on approach for *topographical imaging* in this work, the scenario of traditional SICM experiments is avoided where, based on recent work,[42,44] an applied bias upon approach to heterogeneously charged substrates, may result in a non-constant working distance and hence distorted topography (Figure 2.4c).

To demonstrate the efficacy of BM-SICM for probe positioning near a surface, independent of surface functionality, a series of nanopipette approaches towards

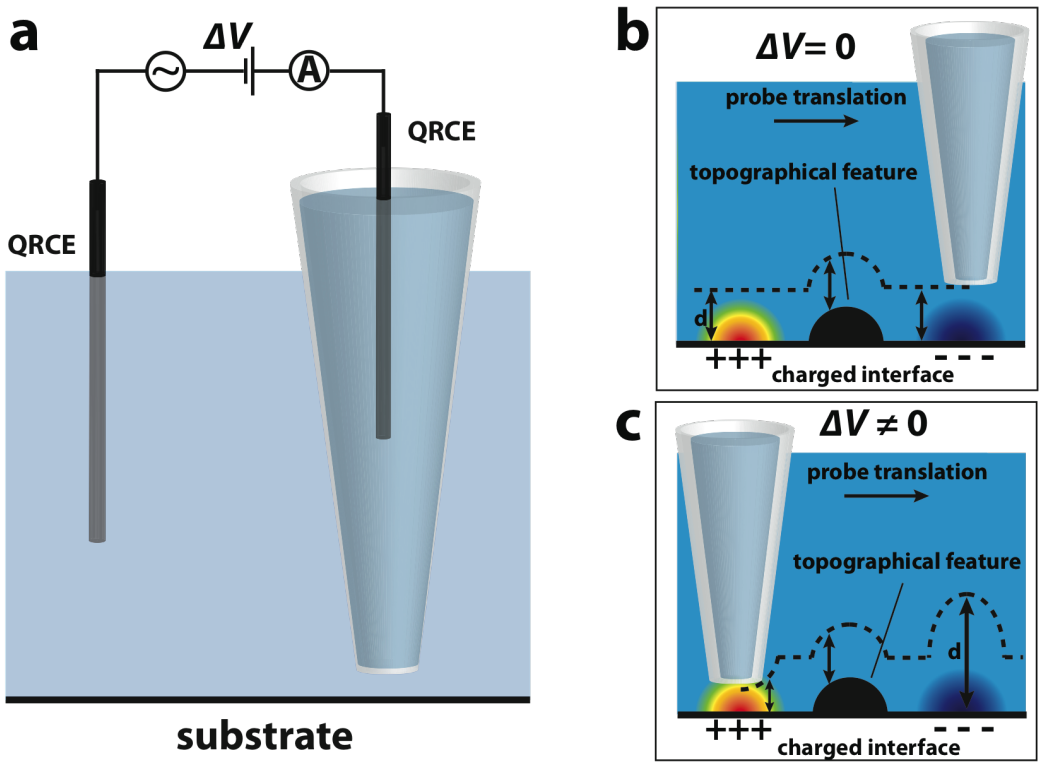

Figure 2.4: Concept of simultaneous topographical and charge mapping with a positionable nanopipette. a) Schematic representation of the bias-modulation SICM (BM-SICM) setup. Graphical representation (not to scale) demonstrating deconvoluted (b) and hypothetically convoluted (c) scanning over a sample containing topographical (shown in black) and charge features (double layer over positively and negatively charged areas are shown in rainbow and blue gradients, respectively). The possible probe trajectory for a fixed set point (target distance, d) is shown as a dashed line.

positively (APTES) and negatively (glass) charged substrates was carried out at different nanopipette biases, applied to the probe. Here the distance, d, was defined with respect to the distance of closest approach, *ca.* 25 nm or less. For simulations, d is the absolute tip-substrate distance. These approach curves, and all experimental and simulation studies herein, were performed using an oscillation frequency of 270 Hz. This frequency was selected based on our recent work[45] and impedance studies performed herein that highlights a frequency domain where the AC phase is most sensitive to changes in both system capacitance and resistance. This region is where

the slope of the Bode plot of AC phase against frequency is greatest, which can be seen to exist between 100 Hz and 1 kHz, for the experimental conditions of the experiments herein (Figure 2.3). Below this frequency range, the phase is zero, as the current solely passes through the resistive component of the system. Above this frequency range the current is dominated by the capacitive component of the system.

As expected, based on recent DM-SICM studies,[42,44] at close probe-substrate separations in BM-SICM surface-induced rectification influences the mass-transport of ions, leading to surface-enhanced or diminished ion current values, compared to the bulk to which currents are normalised (Figure 2.5a and b), depending on the substrate charge and the SICM bias polarity. The AC phase shift (which we define throughout as the distance-dependent phase with respect to that with the nanopipette in bulk) is particularly sensitive to the presence of surface charge at the substrate when $\triangle V \neq 0$ (see Figure 2.5c and d), an aspect we explore further below with FEM simulations. The AC amplitude also exhibits a dependence on the substrate surface charge, albeit weaker due to the small driving voltage oscillation, seen to be enhanced under the same conditions as the DC enhancement and diminished with decreasing DC values. The AC amplitude approach curves in Figure 2.6 were recorded simultaneously with the data in Figure 2.5. The shape of these approaches can be seen to correlate with the shape of the DC approach curves, increasing with negative tip bias and decreasing at positive tip bias, upon approach to a negatively charged substrate such as glass.

Interestingly, although these effects are manifested at low ionic strength, for reasons outlined in the introduction, they can be seen at relatively high ionic strength. Approaches performed at electrolyte with higher salt concentration, and negative tip bias towards a negatively charged glass substrate, show that even at 100 mM (see Figure 2.7 for data), at very small tip-substrate separations, the DC and AC ion components are still sensitive to surface charge. This indicates that special

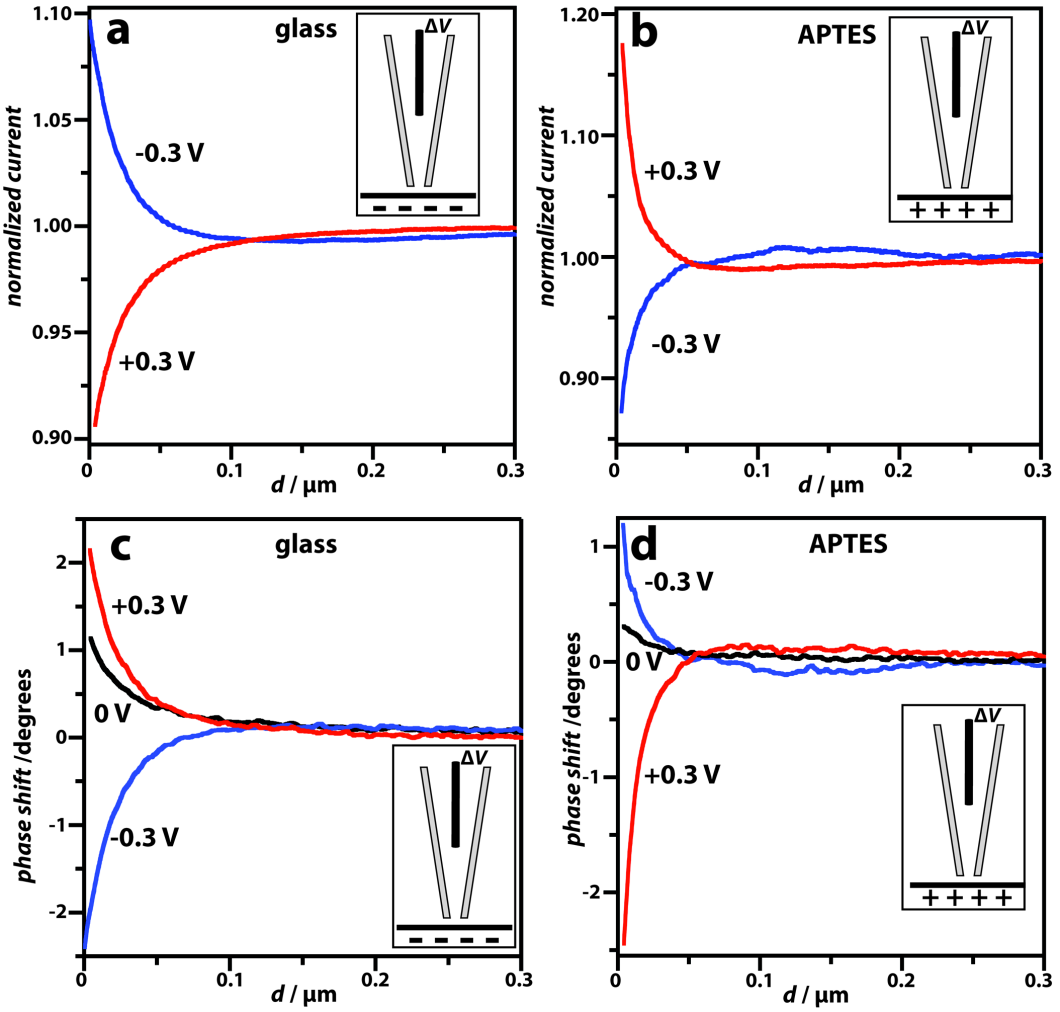

Figure 2.5: Experimental approach curves depicting: normalised DC ion current (a) and (b); and phase shift (c) and (d) behavior as a function of the probe-to-substrate distance, d, recorded with *ca.* 75 nm radius nanopipette over negatively charged glass and positively charged APTES substrates at +0.3 V (red lines), -0.3 V (blue lines) and 0 V (black lines) bias offset ($\triangle$V) values. Schematic illustrations, as insets, depict the nanopipette approaching variously charged substrates for the corresponding plots. The DC ionic currents are normalised to the respective values at solution bulk, while the phase shifts are reported with respect to the corresponding bulk values. The DC data at 0 V are not presented, as there is no significant ion flow.

care has to be taken when SICM is implemented for recording substrate topography as it can be potentially convoluted with the surface charge. This may particularly be the case for nanoscale pipettes (*e.g.* $<$ 30 nm diameter)[32,48] where charge effects

will be magnified. Whilst this may be a problem in a traditional SICM arrangement, when the surface is approached at 0 V net bias, using bias-modulated SICM, this effect is minimised and the topography can be accurately tracked. These data have important implications for how topographical SICM experiments are designed (to avoid charge effects), but could also be exploited to allow for the probing of the double layer at biological samples *in vivo*, which require a physiological environment (relatively high ionic strength) for viability. Note that the data are especially significant as we have used a relatively large SICM tip for these studies, and the effects seen at high ionic strength would be magnified with smaller tip sizes deployed at closer sample distances.

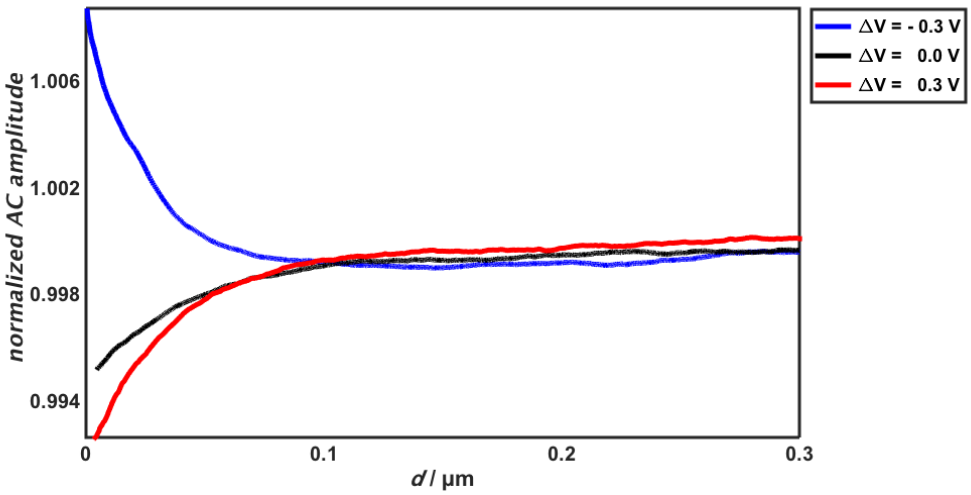

Figure 2.6: Typical BM-SICM AC amplitude approach curve to negatively charged glass substrate at different potentials (-0.3, 0 and +0.3 V bias for blue, black and red lines, respectively).

A major observation in Figure 2.5 is that with no mean bias ($\triangle V = 0$, with just a small amplitude oscillation of the bias between the QRCEs) the phase shift is intrinsically a *distance-dependent quantity* and is relatively *insensitive to surface charge*. The phase of the AC current (with respect to the bulk response) shifts slightly positive over both the negatively charged glass substrate and positively charged APTES functionalism substrate (Figure 2.5c and d). In order to account

for these AC effects, and to assess BM-SICM for topographical and charge mapping, finite element simulations were used to study the AC and DC SICM response towards a harmonic perturbation of the electric potential.

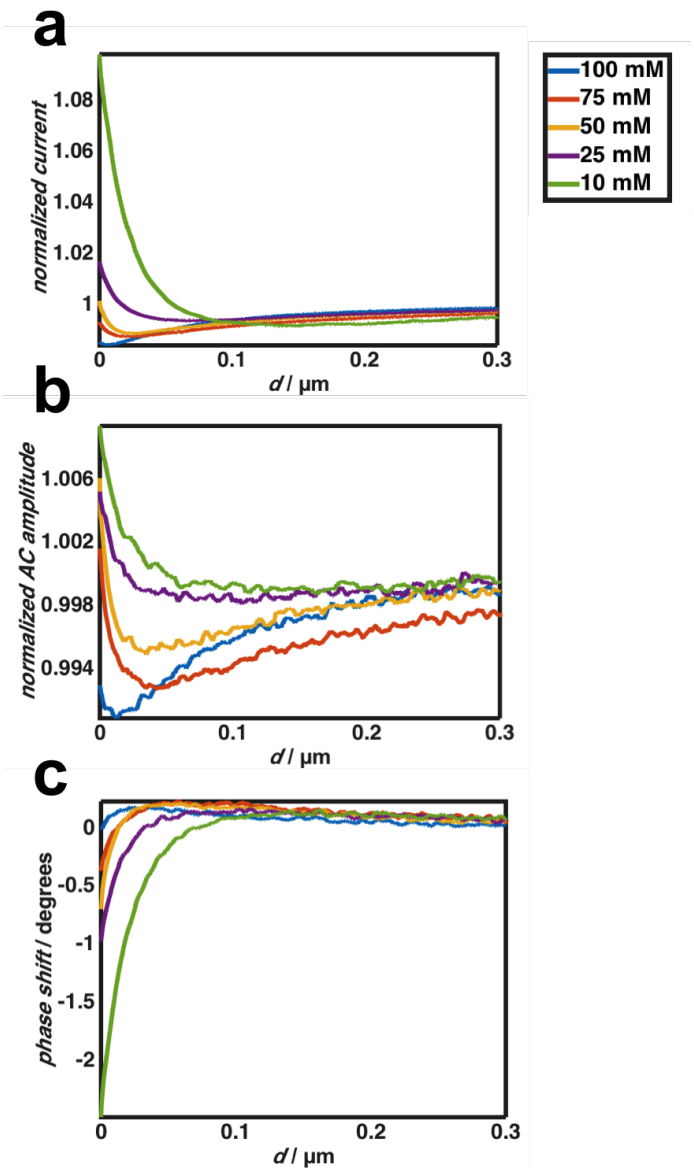

Figure 2.7: a) Normalised DC ion current, b) normalised AC amplitude and c) relative phase shift acquired with *ca.* 75 nm radius nanopipette probe during BM-SICM approaches to a negatively charged glass substrate with -0.3 V tip bias and varying supporting electrolyte concentrations. Green, purple, yellow, red and blue curves correspond to 10, 25, 50, 75 and 100 mM KCl (see also the legend on the figure).

2.5.2 Theory and Simulations

The simulation of the harmonic perturbation of the DDL due to an applied alternating potential is a complicated task, especially in a nanopore or nanopipette configuration, and a typical treatment of this problem is performed in terms of equivalent electrical circuits.[45,49] Here, we adopt a more general approach by studying the ionic transport and ion distributions, from which we can derive the resulting impedance response, using finite element method modelling.

Ions are considered as point charges, while ionic transport is assumed to follow the classical Nernst-Planck relationship, where the flux J_i of species, i, is given as

$$J_i = -D_i \bigtriangledown c_i - z_i \frac{F}{RT} D_i c_i \bigtriangledown \phi \tag{2.1}$$

while the Poisson equation describes the electrical potential ϕ:

$$\bigtriangledown^2 \phi = -\frac{F}{\varepsilon \varepsilon_0} \Sigma z_i c_i \tag{2.2}$$

here c_i denotes the species concentration, while D_i, z_i, F, R, T, ε and ε_0 specify constants: system diffusion coefficient of i, its charge number, the Faraday constant, gas constant, temperature, relative permittivity and vacuum permittivity, respectively.

Throughout this work a surface charge density on the nanopipette tip was assumed to be -1.125 mC m^{-2} (140 nm^2 per ionised site), consistent with previously reported simulations.[40–42,50,51] However, the actual density of ionisable sites strongly depends on the nature of the material and could vary within the range of microcoulombs to a few hundreds of millicoulombs per squared meter of a surface.[42,52–55]

The system of differential equations 2.1 and 2.2 was solved with appropriate boundary conditions (Figure 2.1 and Table 2.1), for a particular $\triangle V$ and assuming

flux conservation in a first step (eq. 2.3)

$$\bigtriangledown J_i = 0 \tag{2.3}$$

Then, for AC analysis, a harmonic bias modulation was applied between the two QRCEs in the form of a linearised perturbation in the frequency domain,

$$\bigtriangledown J_i = j\omega c_i \tag{2.4}$$

for AC analysis, where j is the imaginary unit and ω is the angular frequency.

This approach provides a powerful framework to study the impedance response both in bulk (see for example Figure 2.3) and with a nanopipette positioned at different separations from a charged or uncharged substrate. As highlighted earlier in Figure 2.5, the experimental phase shift with zero net bias, $\triangle V = 0$, as a function of distance appeared relatively insensitive to the surface charge, while for an applied bias ($\triangle V \neq 0$) there was a surface-charge dependent phase shift.

An example snapshot of the simulated electric field that is running through the end of the nanopipette's glass wall is illustrated in Figure 2.8a, note that the x and y axis has different scale for illustration purposes only. The graph in Figure 2.8b shows the numerical change in the electric field inside the glass wall against hight for the total simulated domain.

Figure 2.9a shows the phase shift of simulated approach curves towards substrates with applied surface charge of $\pm$ 30 mC m^{-2} (5 nm^2 per ionised site) and 0 mC m^{-2}. It can be seen that the model predicts the phase shift of the induced harmonic ion current to be almost independent of surface charge when there is no DC bias offset between the QRCEs, similar to the experimental observations in Figure 2.5c and d. This effect has a very important consequence for careful (and accurate) probe positioning over a sample surface, as the phase shift value is an intrinsically sensitive quantity that evidently depends predominantly on the tip-to-

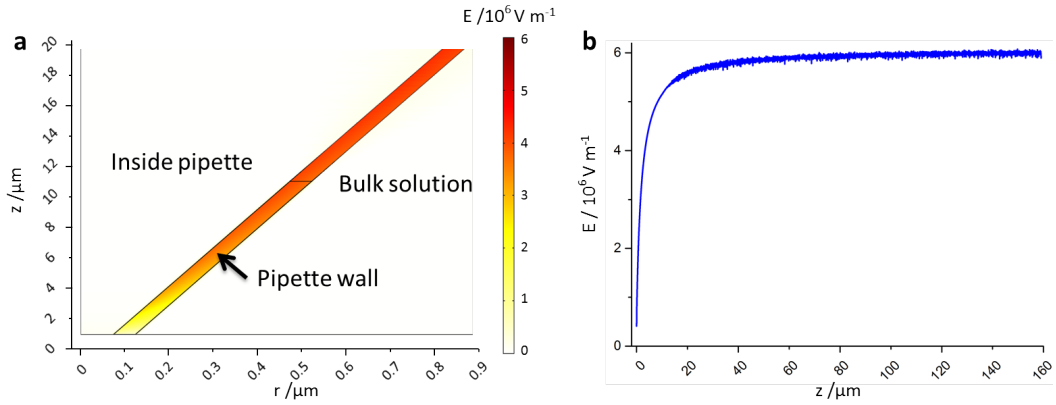

Figure 2.8: a) A snapshot of an electric field map at the end of the nanopipette resulting from simulation (note different scales on x and y axis), b) The change in electric field against hight for a cross section line that was drawn at the centre of the nanopipette wall along the whole domain.

substrate distance when $\triangle V = 0$. Under these conditions, Figure 2.9a (and Figures 2.5c and 2.5d) make it clear that with $\triangle V = 0$, the phase shift can be used as a set point for determining topography and being able to position the probe at close tip-to-substrate separations, which is important for enhancing the resolution of SICM.[56,57]

In a similar way to the experimental approaches at non-zero bias (Figure 2.5), the model predicts a dramatic change of the phase-distance behavior for $\triangle V \neq 0$. Figure 2.9b depicts theoretically predicted approach curves that demonstrate the sensitivity of the AC phase to surface charge. The AC phase shift can be seen to be negative under conditions when an enhanced ionic current is observed, that is when negative $\triangle V$ is applied to the tip QRCE with a negatively charged substrate. In this case the system resistance, upon approaching the substrate, decreases and so more current flows through the resistive component of the system, resulting in the phase tending more towards 0 degrees, thus explaining the negative phase shift from the bulk value, which is between 0 and 90 degrees (Figure 2.3). It can further be seen that the magnitude of the effect scales with the surface charge density, as would be expected. As the polarity of the bias is reversed, so that the nanopipette

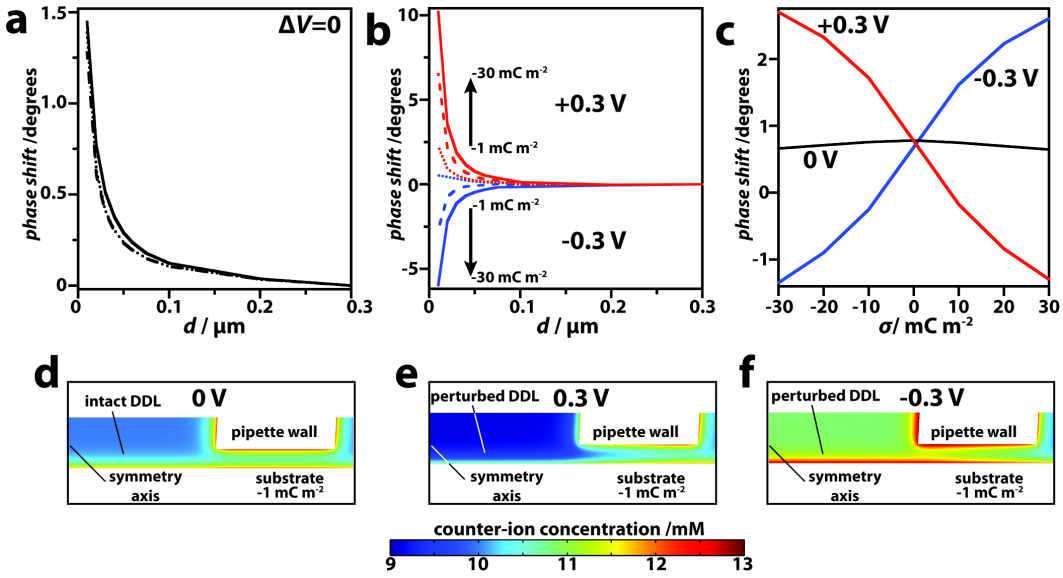

Figure 2.9: a) Simulated BM-SICM approach curves in the absence of mean bias offset ($\triangle V = 0$) at 270 Hz, 10 mV rms amplitude bias modulation over a substrate carrying surface charge densities σ of 0 (solid), -30 (dotted) and +30 (dashed) mC m^{-2}. b) A series of simulated approaches towards a negatively charged surface (σ values -30 (solid), -10 (dashed) and -1 (dotted) mC m^{-2} with the arrows indicating an increase of the absolute magnitude of surface charge density) at bias values of +0.3 V (red lines) and -0.3 V (blue lines). c) Theoretically predicted values of the phase shift of the ion current passing through a 75 nm radius nanopipette positioned at 25 nm from a charged surface at 0 V, -0.3 V and +0.3 V bias (black, blue and red lines, respectively). d-f) Calculated steady-state concentration profiles of DDL counter-ion, for a DC bias only, near a nanopipette tip positioned 10 nm above a charged interface (σ = -1 mC m^{-2}) at d) 0 V, e) +0.3 V and f) -0.3 V bias. Note that only half of the symmetric nanopipette cross-section is shown.

QRCE is positive, the negatively charged substrate now induces a diminution of the ionic current and a positive shift in the phase is observed. In this case, the system resistance increases as the tip approaches, so more current flows through the capacitive component of the system and the phase tends to increase towards 90 degrees. Thus, a positive phase shift from that with the nanopipette in bulk is observed. The simulated DC signal mirrors this behavior (Figure 2.10) with the DC current increasing compared to the bulk at close tip-substrate distances (negatively charged substrate) with positive bias on the nanopipette QRCE, but decreasing at negative bias.

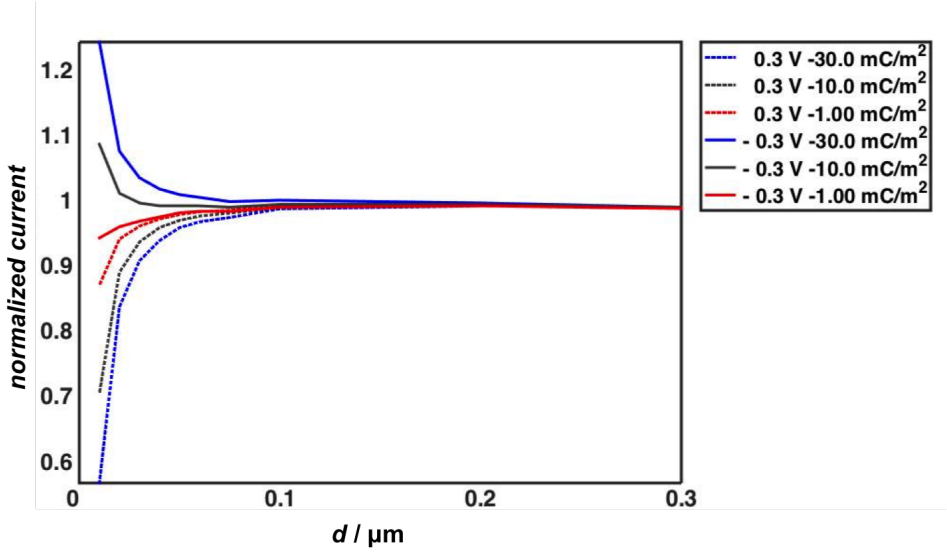

Figure 2.10: Simulated DC approach curves to negatively charged substrates at positive and negative tip bias (see the legend for the description of color code).

From these data it is clear that even a relatively small surface charge (down to 1 mC m^{-2}, equivalent to 160 nm^2 per ionised site) leads to strong variation of the phase shift with bias, that is particularly noticeable when the probe is brought in a close proximity to a substrate (especially, at distances below one tip radius, $d < r_{tip}$). This effect, revealed with an applied bias, can therefore be employed for mapping surface charge with the nanopipette held at a constant distance above the specimen during scanning, as considered below.

Figure 2.9c shows the phase shift with a 75 nm radius nanopipette positioned 25 nm above a charged substrate, as a function of surface charge density for 3 biases, $\triangle V$ = +0.3 V, 0 V and -0.3 V. The plots clearly illustrate the sensitivity of the technique, at a constant probe-to-substrate distance, to distinguish between values of surface charge. Importantly, at 0 V bias, a wide range of surface charges have little influence on the phase, making this condition ideal for detecting surface topography, as discussed above. The sensitivity (magnitude) of the phase to a particular surface charge is similar at both positive and negative bias polarities, although the technique offers slightly higher sensitivity in cases when surface-induced rectification acts to

enhance the ionic current (*e.g.* at negative tip bias over a positively charged surface or at positive tip bias over a negatively charged surface).

The reasons for the striking effect of bias on the phase response (Figures 2.9) and DC current response of BM-SICM (Figure 2.5) with charged surfaces becomes apparent from the distribution of electrical potential and ion concentrations near the tip opening (when held in the proximity of a surface). With a 0 V bias offset there is almost no perturbation of the DDL at the substrate, which remains intact. The application of bias, however, is known to lead to ICR inside the nanopipette itself[39–41] (when it is freely suspended in bulk) and a surface-induced rectification.[44] This causes a drastic change in the nanopipette conductance state depending on bias polarity and surface charge due to a significant change of ionic conductivities (and therefore, the overall resistance) within and near the tip opening (see Figure 2.9e and f for $\triangle V$ values of +0.3 V and -0.3 V, respectively). In turn, the AC ion current components, particularly the phase shift, which are highly sensitive to the overall resistance, as explained above, also demonstrate a strong dependence on the nature of the charged interface.

2.5.3 Probing Acid-Base Equilibria at Interfaces

To illustrate the capabilities of BM-SICM for sensing variations of surface charge, a series of approaches towards glass substrates was carried out as a function of bulk pH (surface titration experiments).

The electrostatic charge on glass and silica surfaces is typically attributed to the presence of silanol groups (SiOH) due to the following acid-base equilibrium:

$$-SiOH \rightleftharpoons -SiO^- + H^+ \tag{2.5}$$

The dissociation process, however, is rather complicated and depends on the particular type of silica and any surface treatment. In a first approximation, the

degree of dissociation depends on the inherent properties of the glass-electrolyte interface (given by the intrinsic dissociation constant, K_{int}) as well as the electrostatic potential on the surface, ψ_0 :[58]

$$\frac{[H^+]\Gamma_{SiO^-}}{\Gamma_{SiOH}} = K_{int} exp[\frac{F\psi_0}{RT}] \tag{2.6}$$

A broad range of silica interfaces show a pK_{int} in the range 7 - 7.5[52,54] and the surface charge density σ can be estimated, using equation 2.6 along with mass-conservation, which defines the surface concentrations of protonated and deprotonated sites (Γ_{SiOH} and Γ_{SiO^-}, respectively)

$$\sigma = -e\Gamma_{SiO^-} = -e\Gamma_{total}\frac{K_{int}10^{pH}exp[\frac{F\psi_0}{RT}]}{1 + K_{int}10^{pH}exp[\frac{F\psi_0}{RT}]} \tag{2.7}$$

where Γ_{total} represents the total number of silanol groups per unit area and e is the elementary charge. The surface potential can be calculated from the Grahame equation (for monovalent electrolyte ions present at c_0 bulk concentration):[58]

$$\sigma = (8RT\varepsilon\varepsilon_0 c_0)^{1/2} sinh[\frac{F\psi_0}{2RT}] \tag{2.8}$$

Solution of equations 2.7 and 2.8 provides the self-consistent surface charge density value. However, surface acid-base equilibria on other types of silica are characterised by two dissociation constants[53,59] with corresponding pK_a of 4.5 and 8.5. These values are associated with two different types of titratable silanol groups, present at the surface at 19% and 81% of the total number of ionised sites, respectively.[53,59] The total surface charge density is therefore given through both contributions.

It follows that under ambient conditions (pH $\sim$ 7) a small fraction of silanol groups are ionised, resulting in a negatively charged surface. The experimental approaches of phase shift vs. tip to surface distance, d, shown in Figure 2.11 for an applied bias $\triangle V$ = -0.3 V to the nanopipette and the DC data in Figure 2.12,

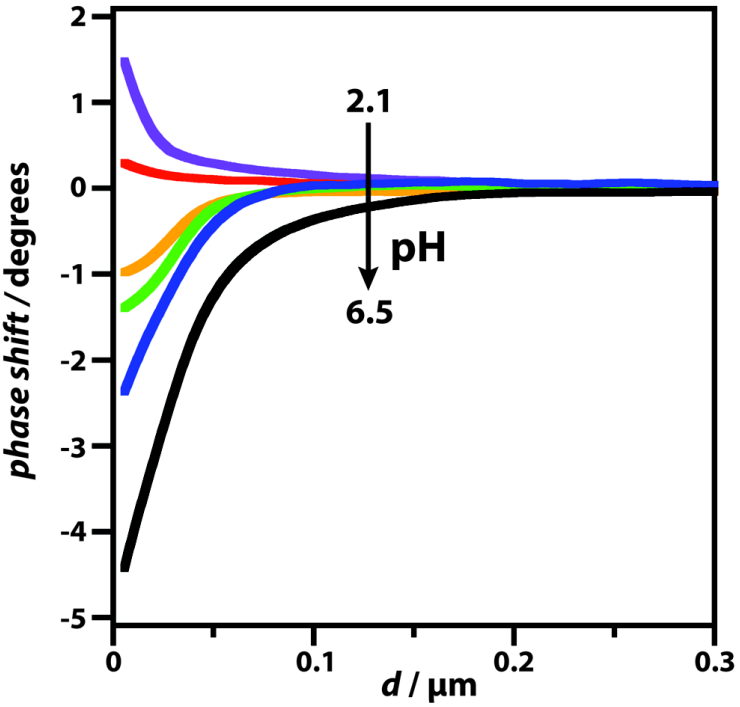

Figure 2.11: Experimental approach curves recorded with *ca.* 75 nm radius nanopipettes over a glass substrate at different solution pH (2.1, 2.5, 3.3, 3.7, 4.3 and 6.5 for purple, red, orange, green, blue and black lines, respectively) performed with a bias, $\triangle V$ = -0.3 V applied to the nanopipette QRCE with respect to that in bulk solution. The arrow indicates an increase of the solution pH.

confirm the presence of a negative surface charge under these conditions, as surface-enhanced rectification induces a significant decrease of the AC phase value (and increase in the DC value, Figure 2.12), when the nanopipette is brought into the vicinity of the substrate.

In more acidic solutions, increasing protonation of the silanol groups leads to an overall decrease of (absolute) surface charge density. Experimental phase shift-distance approach curves (Figure 2.11) under these conditions (pH = 2.1 - 4.3), reveal a smaller surface-enhanced rectification at lower pH. At pH values around 2.1 - 2.5 the AC phase shift-distance curves approach the behavior expected at an uncharged interface, in good agreement with a point of zero charge found on most of silica materials (typically, in the pH range 2 - 4).[60] Approach curves shown in

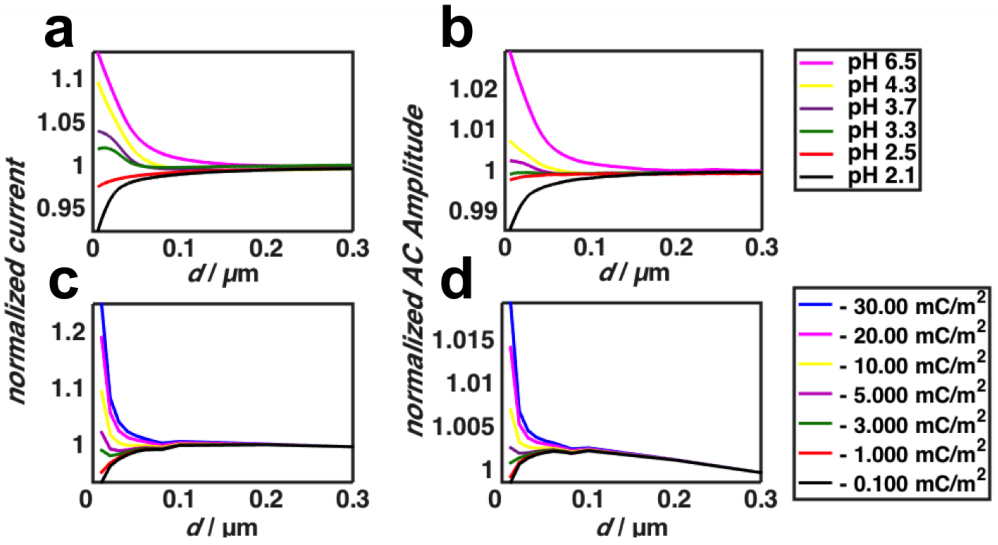

Figure 2.12: Experimental DC (a) and AC amplitude (b) and theoretical DC (c) and AC amplitude (d) approach curves to a glass substrate bathed in solutions of varying pH (see the legend for the color code on the graphs).

Figure 2.11 evidence an almost linear variation of near-surface phase shift with pH over the range studied. Based on our simulations presented above (Figure 2.9c), this behavior suggests a linear-like titration of surface charges with pH. Dedicated modelling in the future could provide further insight into the protonation of this type of surface, although it needs to be recognised that other processes can complicate the analysis and interpretation. Although the electric field from the SICM probe is in the kV cm^{-1} range, a field of this range is unlikely to induce changes in the local acid disassociation constants, as the Wein effect occurs at hundreds of kV cm^{-1}.[61–63] However local ion mobilities, particularly of protons at surfaces,[64,65] maybe high and would need to be taken into account, with the tip-induced field possibly altering local pH values.

2.5.4 Surface Charge Mapping

Simultaneous mapping of surface charge distributions along with independent recording of surface topography is a particular advantage of the SICM technique described

herein: an AC phase shift at 0 V mean bias can be used for a positionable feedback control, whereas measurements at $\triangle V \neq 0$ allow the detection of surface charge. We implemented this concept using a hopping voltammetric scan strategy, where the nanopipette was approached towards the substrate until a set value of a feedback parameter (phase shift, 0.5° used herein) was reached, followed by the recording of a cyclic voltammogram at that position (for which we present the linear part between -0.4 and +0.4 V) to sense the charge. The probe was then moved away from the surface and to the next pixel such that a spatial array of voltammograms was recorded. At each pixel, a voltammogram was recorded when the probe was away from the surface (d = 500 nm) and this response was subtracted from the surface voltammogram to reveal only the surface ICR.

The capability of this approach was validated for a partial polystyrene film on a glass substrate, comprising heterogeneously distributed pinholes (exposing the glass) in the polystyrene layer. This substrate thus comprised both negatively charged glass regions, in 10 mM KCl solution, and neutral areas (uncharged polymer film). The topography recorded from the initial approaches to the substrate at $\triangle V = 0$ is shown in Figure 2.13a. This matches well to the typical topography recorded using AFM (Figure 2.13b). Taking into account the working distance (given by the set point value, corresponding to *ca.* 25 nm), SICM allows careful examination of substrate topography independently of surface charge. Even the smaller nanoscale pits in the film are apparent in the BM-SICM topography, an advance on our recent DM-SICM studies[44] in terms of resolution.

Rectification of the AC current, particularly the phase, appears to be very beneficial for ion sensing within the DDL of a surface. Phase-bias curves shown on Figure 2.14a can provide a *fingerprint* of surface-induced rectification in a similar way that current-voltage curves are used to characterise ICR in nanostructures.[40,41,51] The charge state of the substrate clearly plays a key role in the rectifying characteristics. The curves for bulk solution and over an uncharged polystyrene film are

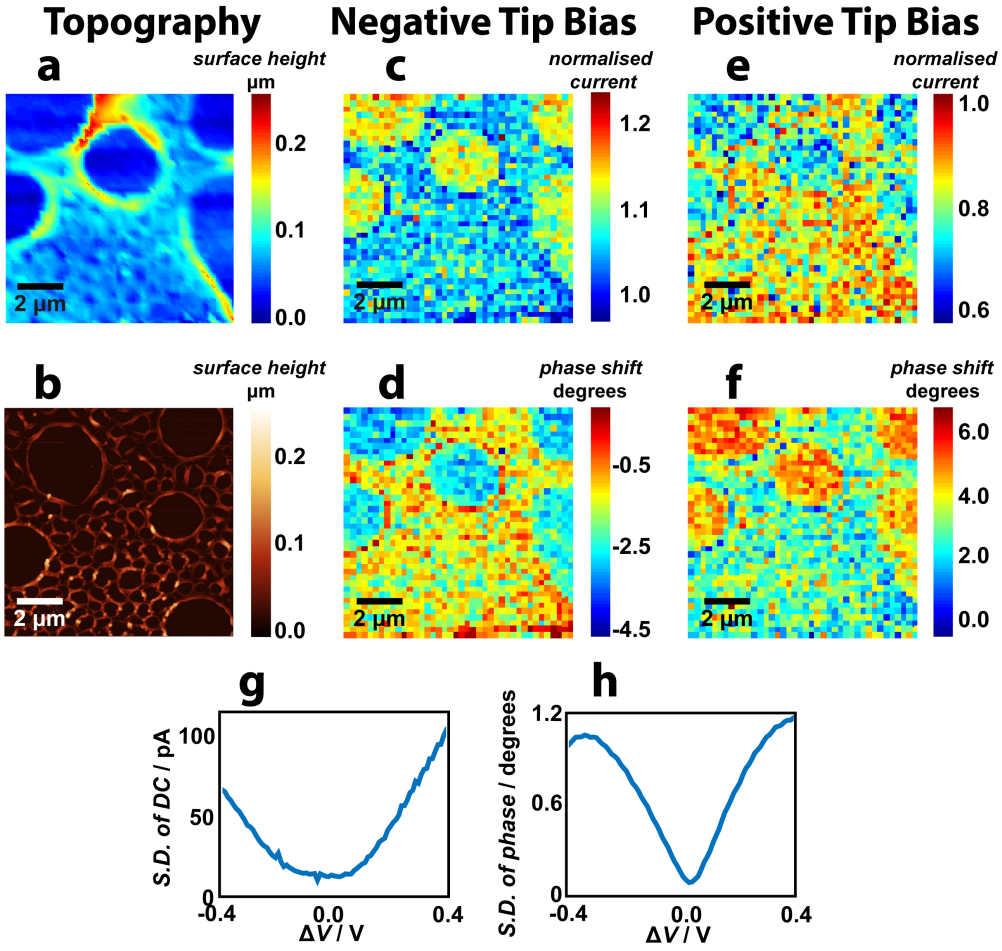

Figure 2.13: Simultaneous surface charge and topographical mapping over a non-uniform polystyrene film on glass. a) Topography image recorded with a ∼75 nm radius nanopipette operated in a hopping mode at 0 V bias offset and b) an AFM image of a similar area of a substrate. c)-f) Example images of the normalised DC component and AC phase shift (with the response in bulk subtracted) of the ion current at -0.3 V and +0.3 V mean bias values. Standard deviation of g) ion currents and h) bulk-corrected AC phase shift calculated across each image in a set of image frames acquired at 81 equally spaced bias values over the linear regions scanned between -0.4 and +0.4 V.

very similar, proving the absence of surface charge on a polystyrene surface. The intrinsic rectifying properties of the glass nanopipette lead to slight rectification (as manifested in the phase shift change with $\triangle V$) but this is independent of the

tip-substrate separation over polystyrene. In contrast, there is considerable surface-induced rectification with the nanopipette over glass, consistent with the presence of negative charge.

Recorded voltammograms in bulk solution allow for the subtraction of the rectifying behavior of the probe itself from the measurement at surface proximity (as used to present the imaging data). As evident from Figure 2.14b, in such a case, the neutral polystyrene substrate exhibits almost no surface-driven ICR. In the case of a charged surface, *e.g.* glass, the effect of the surface-induced rectification is clear in the phase-bias response.

Significantly, the protocol used produces voltammetric data that can be represented as 81 image frames (phase and DC as a function of x, y position) at a set of different bias values at 10 mV intervals. Maps of the DC current at the surface, normalised by that in bulk, and AC phase shift at the surface with respect to bulk (subtracted) at -0.3 V and +0.3 V are presented in Figure 2.13c - f. (A full image sequence is given in a form of video files DC_CV_Polystyrene and Phase_CV_Polystyrene). These images, free from topographical effects, are highly revealing of the charge distribution across the surface, which is evidently very heterogeneous, from both the DC current and phase maps. In particular, it can be seen that there is an increase in the ion current magnitude, when a higher conductance state is formed. That is, with a negative tip bias applied to the nanopipette over negatively charged regions (Figure 2.13c), where the normalised current magnitude ratio attains values between 1.1 and 1.2; or current diminution with positive tip bias in negatively charged regions where the normalised current attains values <0.8 (Figure 2.13e).

The corresponding phase behavior (Figures 2.13d and f) shows the interfacial charge effect with stronger contrast due to the fact that any change in the resistance is detected as a change in the ratio between the capacitive and resistive behavior of the nanopipette (and better signal to noise due to measurement with the lockin

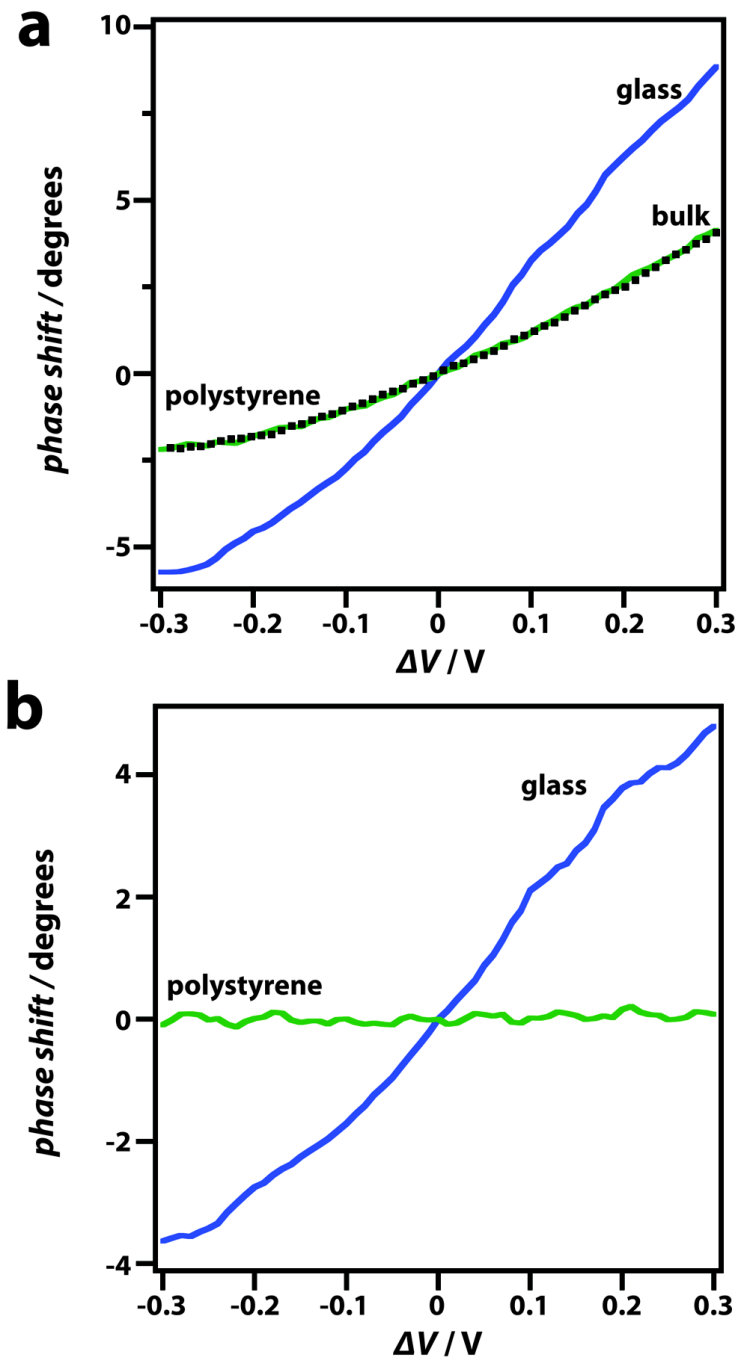

Figure 2.14: a) Experimental phase shift-voltage characteristics of a nanopipette (75 nm radius) in a bulk solution (black dotted line), and positioned over an uncharged polystyrene film (green solid line) and negatively charged glass (blue solid line). b) Phase shift-voltage curves near polystyrene and glass with bulk data subtracted.

amplifier). When the nanopipette experiences a low conductance state, the capacitance provides a larger contribution, which ideally has 90° degrees phase shift with respect to the driving voltage, while at a high conductance state a nanopipette acts more like as a resistor (0° degrees phase shift for resistor circuit component).

The change of the conductance state of the nanopipette is also seen in voltammograms recorded at each pixel during imaging. As follows from the image sequences (see Figure 2.14 and the video files provided on a CD), the AC phase shift flips from negative to positive as the bias ($\triangle V$) is scanned from negative to positive values through 0 V. With the bias *ca.* 0 V, however, the phase signal across both the glass and polystyrene regions of the sample is close to the set point value because of the insensitivity of the phase to surface charge when $\triangle V = 0$, a key feature of this technique that we have described.

These data allow the standard deviation of every pixel value of each DC and phase image in the sequence to be calculated, with results shown in Figures 2.13g and h. It is clear that around $\triangle V = 0$, the images are relatively featureless (small standard deviation), but increase with a higher magnitude of applied potential, consistent with the greater contrast between the heterogeneously charged regions seen at ± 0.3 V. Interestingly, the region where the standard deviation attains a minimum is relatively broad (-0.2 V - 0.1 V) for the DC signal, highlighting the lower sensitivity of the DC signal (Figure 2.13g) towards surface charge compared to the AC phase signal (Figure 2.13h), where the minimum of the standard deviation vs. potential plot is much sharper.

2.6 Conclusions

This work provides a robust framework for nanoscale mapping of surface charge variations at substrates through sensing the ionic atmosphere of the diffuse double layers formed at interfaces with a simple nanopipette approach. We have explored

the versatility of bias-modulated SICM for independent and accurate characterisation of the topographical and charge properties of surfaces, using the capability of BM-SICM for performing experiments in the absence of a mean applied bias. In this situation, the nanopipette can be carefully positioned over the sample at a desired distance, using a set point value of the AC phase shift of the ionic current, which is shown to be a distance-dependent quantity, essentially unaffected by surface charge that makes it ideal for topographical mapping.

At non-zero bias, however, BM-SICM becomes an extremely sensitive tool for probing surface charge *via* surface-induced rectification. Our experimental findings, supported by finite element simulations, suggest that AC components of the ionic current, and, in particular, the phase shift are very responsive to the local resistance and, correspondingly, variations in surface charge. The possibility of imaging heterogeneities of surface charge makes this technique indispensable for surface science, to unravel structure-functional relationships and to provide insights on interfacial processes and adsorption equilibria that modify the charge. Here, we have been able to resolve topography, free from surface-charge effects, and obtain semi-quantitative insights into surface charge. Further quantitative analysis will require extremely detailed characterisation of tip geometry and charge (which is often not the precise conical shape assumed in this and other work), and the charge/ICR characteristics of the nanopipette itself, as well as considerations of changes in ion mobility near surfaces. For future studies, transmission electron microscopy of glass nanopipettes[66] should allow better understanding of the probe geometry and, in perspective, this nanopipette approach should offer detailed quantification of surface charges.

2.7 References

1. Sahin, Ö.; Nusret Bulutcu, A. *J. Cryst. Growth* **2002**, 241, 471-480.

2. Lin, N. H.; Shih, W.-Y.; Lyster, E.; Cohen, Y. *J. Colloid Interface Sci.* **2011**, 356, 790-797.

3. Bodhak, S.; Bose, S.; Bandyopadhyay, A. *Acta Biomater.* **2009**, 5, 2178-2188.

4. Hirsch, V.; Kinnear, C.; Moniatte, M.; Rothen-Rutishauser, B.; Clift, M. J. D.; Fink, A. *in Vitro. Nanoscale* **2013**, 5, 3723-3732.

5. Chan, D. Y.; Pashley, R. M.; White, L. R. A *J. Colloid Interface Sci.* **1980**, 77, 283-285.

6. Ohshima, H.; Healy, T. W.; White, L. R. *J. Colloid Interface Sci.* **1982**, 90, 17-26.

7. Tufenkji, N.; Elimelech, M. *Langmuir* **2005**, 21, 841-852.

8. Cuesta, A. *Surf. Sci.* **2004**, 572, 11-22.

9. Manzini, M. C.; Perez, K. R.; Riske, K. A.; Bozelli Jr, J. C.; Santos, T. L.; da Silva, M. A.; Saraiva, G. K. V.; Politi, M. J.; Valente, A. P.; Almeida, F. C. L., et al. *Biochim. Biophys. Acta, Biomembr.* **2014**, 1838, 1985-1999.

10. Chen, L.; Mccrate, J. M.; Lee, J. C.; Li, H. *Nanotechnology* **2011**, 22, 105708.

11. Chung, T.-H.; Wu, S.-H.; Yao, M.; Lu, C.-W.; Lin, Y.-S.; Hung, Y.; Mou, C.-Y.; Chen, Y.-C.; Huang, D.-M. *Biomaterials* **2007**, 28, 2959-2966.

12. Xiao, K.; Li, Y.; Luo, J.; Lee, J. S.; Xiao, W.; Gonik, A. M.; Agarwal, R. G.; Lam, K. S. *Biomaterials* **2011**, 32, 3435-3446.

13. Dobrovolskaia, M. A.; Patri, A. K.; Simak, J.; Hall, J. B.; Semberova, J.; De Paoli Lacerda, S. H.; McNeil, S. E. *in Vitro. Mol. Pharmaceutics* **2011**, 9, 382-393.

14. Asati, A.; Santra, S.; Kaittanis, C.; Perez, J. M. *ACS Nano* **2010**, 4, 5321-5331.

15. Ghosh, P. S.; Kim, C.-K.; Han, G.; Forbes, N. S.; Rotello, V. M. *ACS Nano* **2008**, 2, 2213-2218.

16. Bakhti, M.; Snaidero, N.; Schneider, D.; Aggarwal, S.; Möius, W.; Janshoff, A.;

Eckhardt, M.; Nave, K.-A.; Simons, M. *Proc. Natl. Acad. Sci. U. S. A.* **2013**, 110, 3143-3148.

17. Arjmandi, N.; Van Roy, W.; Lagae, L.; Borghs, G. *Anal. Chem.* **2012**, 84, 8490-8496.

18. Sprycha, R. *J. Colloid Interface Sci.* **1989**, 127, 1-11.

19. Szekeres, M.; Tombácz, E. *Colloids Surf., A* 2012, 414, 302-313. 20. Gibson, G. T. T.; Mohamed, M. F.; Neverov, A. A.; Brown, R. S. *Inorg. Chem.* **2006**, 45, 7891-7902.

21. Sánchez, J.; del Valle, M. *Crit. Rev. Anal. Chem.* **2005**, 35, 15-29.

22. Heinz, W. F.; Hoh, J. H. *Biophys. J.* **1999**, 76, 528-538.

23. Miyatani, T.; Okamoto, S.; Rosa, A.; Marti, O.; Fujihira, M. *Appl. Phys. A Mater. Sci. Process.* **1998**, 66, S349-S352.

24. Miyatani, T.; Horii, M.; Rosa, A.; Fujihira, M.; Marti, O. *Appl. Phys. Lett.* **1997**, 71, 2632-2634.

25. Hillier, A. C.; Kim, S.; Bard, A. J. *J. Phys. Chem.* **1996**, 100, 18808-18817.

26. Manne, S.; Cleveland, J.; Gaub, H.; Stucky, G.; Hansma, P. *Langmuir* **1994**, 10, 4409-4413.

27. Chen, C. C.; Zhou, Y.; Baker, L. A. *Annu. Rev. Anal. Chem.* **2012**, 5, 207-28.

28. Happel, P.; Thatenhorst, D.; Dietzel, I. D. *Sensors* **2012**, 12, 14983.

29. Rheinlaender, J.; Geisse, N. A.; Proksch, R.; Schäffer, T. E. *Langmuir* **2010**, 27, 697-704.

30. Shevchuk, A. I.; Gorelik, J.; Harding, S. E.; Lab, M. J.; Klenerman, D.; Korchev, Y. E. *Biophys. J.* **2001**, 81, 1759-1764.

31. Hansma, P.; Drake, B.; Marti, O.; Gould, S.; Prater, C. *Science* **1989**, 243, 641-643.

32. Novak, P.; Li, C.; Shevchuk, A. I.; Stepanyan, R.; Caldwell, M.; Hughes, S.; Smart, T. G.; Gorelik, J.; Ostanin, V. P.; Lab, M. J. *Nat. Methods* **2009**, 6, 279-281.

33. Korchev, Y.; Milovanovic, M.; Bashford, C.; Bennett, D.; Sviderskaya, E.; Vodyanoy, I.; Lab, M. *J. Microsc.* **1997**, 188, 17-23.

34. Ushiki, T.; Nakajima, M.; Choi, M.; Cho, S.-J.; Iwata, F. *Micron* **2012**, 43, 1390-1398.

35. Yang, X.; Liu, X.; Zhang, X.; Lu, H.; Zhang, J.; Zhang, Y. *Ultramicroscopy* **2011**, 111, 1417-1422.

36. Takahashi, Y.; Murakami, Y.; Nagamine, K.; Shiku, H.; Aoyagi, S.; Yasukawa, T.; Kanzaki, M.; Matsue, T. *Phys. Chem. Chem. Phys.* **2010**, 12, 10012-10017.

37. Klenerman, D.; Korchev, Y. E.; Davis, S. J. *Curr. Opin. Chem. Biol.* **2011**, 15, 696-703.

38. Bard, A. J.; Faulkner, L. R. *Electrochemical Methods: Fundamentals and Applications*. Wiley New York: 1980; Vol. 2.

39. Wei, C.; Bard, A. J.; Feldberg, S. W. **1997**, 69, 4627-4633.

40. Momotenko, D.; Cortes-Salazar, F.; Josserand, J.; Liu, S.; Shao, Y.; Girault, H. H. *Phys. Chem. Chem. Phys.* **2011**, 13, 5430-5440.

41. White, H. S.; Bund, A. *Langmuir* **2008**, 24, 2212-2218.

42. Sa, N.; Lan, W.-J.; Shi, W.; Baker, L. A. *ACS Nano* **2013**, 7, 11272-11282.

43. Clarke, R. W.; Zhukov, A.; Richards, O.; Johnson, N.; Ostanin, V.; Klenerman, D. *J. Am. Chem. Soc.* **2013**, 135, 322-9.

44. McKelvey, K.; Kinnear, S. L.; Perry, D.; Momotenko, D.; Unwin, P. R. *J. Am. Chem. Soc.* **2014**.

45. McKelvey, K.; Perry, D.; Byers, J. C.; Colburn, A. W.; Unwin, P. R. *Anal. Chem.* **2014**, 86, 3639-46.

46. Sa, N.; Baker, L. A. *J. Am. Chem. Soc.* **2011**, 133, 10398-10401.

47. Siwy, Z.; Heins, E.; Harrell, C. C.; Kohli, P.; Martin, C. R. *J. Am. Chem. Soc.* **2004**, 126, 10850-10851.

48. Shevchuk, A. I.; Frolenkov, G. I.; Sánchez, D.; James, P. S.; Freedman, N.; Lab, M. J.; Jones, R.; Klenerman, D.; Korchev, Y. E. *Angewandte Chemie* **2006**, 118,

2270-2274.

49. Feng, J.; Liu, J.; Wu, B.; Wang, G. *Anal. Chem.* **2010**, 82, 4520-4528.

50. Sa, N.; Baker, L. A. *J. Electrochem. Soc.* **2013**, 160, H376-H381.

51. Kubeil, C.; Bund, A. *J. Phys. Chem. C* **2011**, 115, 7866-7873.

52. Behrens, S. H.; Grier, D. G. *J. Chem. Phys* **2001**, 115, 6716-6721.

53. Fisk, J. D.; Batten, R.; Jones, G.; O'Reill, J. P.; Shaw, A. M. *J. Phys. Chem. B* **2005**, 109, 14475-14480.

54. Sabia, R.; Ukrainczyk, L. *J. Non-Cryst. Solids* **2000**, 277, 1-9.

55. Zhuravlev, L. *Langmuir* **1987**, 3, 316-318.

56. Weber, A. E.; Baker, L. A. *J. Electrochem. Soc.* **2014**, 161, H924-H929.

57. Edwards, M. A.; Williams, C. G.; Whitworth, A. L.; Unwin, P. R. *Anal. Chem.* **2009**, 81, 4482-4492.

58. Stumm, W.; Morgan, J. J. *Aquatic Chemistry: Chemical Equilibria and Rates in Natural Waters.* John Wiley & Sons, 2012; Vol. 126.

59. Powell, H. V.; Schnippering, M.; Mazurenka, M.; Macpherson, J. V.; Mackenzie, S. R.; Unwin, P. R. *Langmuir* **2008**, 25, 248-255.

60. Papirer, E. *Adsorption on Silica Surfaces.* CRC Press: 2000.

61. Eckstrom, H. C.; Schmelzer, C. *Chem. Rev.* **1939**, 24, 367-414.

62. Onsager, L.; Kim, S. K. Wien *J. Phys. Chem.* **1957**, 61, 198-215.

63. Onsager, L. *J. Chem. Phys* **1934**, 2, 599-615.

64. Slevin, C. J.; Unwin, P. R. *J. Am. Chem. Soc.* **2000**, 122, 2597-2602.

65. Lockwood, G. K.; Garofalini, S. H. *J. Phys. Chem. C* **2014**, 118, 29750-29759.

66. Zhou, L.; Zhou, Y.; Baker, L. A. *Electrochemical Society Interface* **2014**, 47.

67. Nadappuram, B. P.; McKelvey, K.; Al Botros, R.; Colburn, A. W.; Unwin, P. R. *Anal. Chem.* **2013**, 85, 8070-8074.

Chapter 3

Confocal Fluorescence Visualisation: Application to Proton Attack at the Treated Enamel Substrate

Al Botros R.; Bawazeer T. M.; Paulose Nadappuram B.; Peruffo M.;
Colburn A. W.; and Unwin P. R.

in preparation

3.1 Abstract

Herein we report the first use of confocal laser scanning microscopy (CLSM) coupled with scanning electrochemical microscopy (SECM) as a means of time dependent visualisation and quantification of proton dispersion at surfaces. This technique provides high spatial and temporal resolution allowing millisecond analysis of proton induced enamel dissolution and treatment effects on substrates. The study included generation of protons near treated and untreated enamel surfaces, which were immersed in a fluorescein solution, through the electrochemical oxidation of water, and subsequently, recording the associated pH changes. The CLSM permitted the measuring of pH profiles through recording of changes in fluorescent intensity along the gap between the UME and the substrate, thus, enabling the prediction of protons absorption by the sample surface. A finite element method (FEM) model was constructed to analyse and better understand the experimental results.

3.2 Introduction

The capability to unveil surface reaction rates of heterogeneous reactions at solid-liquid interface is of great importance and have wide applications in a number of industrial fields such as corrosion,[1,2,3] electrochemical sensors, electrochemical reactors,[4] fuel cells[4,5] and minerals dissolution.[6,7]

Reaction processes at a surface often involve a flux of molecules/ions from bulk or a source dispersing towards the reactive sites where the reaction of interest takes place. The ability to visualise and analyse this flux of reactants, *i.e.* diffusion profiles around the active sites, is crucial for obtaining a deeper insight on the reaction process. This potentially permits the extraction of reaction rates in an indirect fashion, and investigates any secondary processes occurring close to the surface, such as the formation of transitory species.

Various analytical techniques has been used to probe reaction kinetics at surfaces, including interferometry,[8,9] and channel flow cell (CFC).[10−12] Interferometry measures the refractive index gradient of a medium, which relies on the solute concentration gradient in a solution. It has high spatial resolution wherein concentration profiles can be measured with submicron resolution. The drawbacks of this technique is that, it has low sensitivity, thus relatively high concentrations should be used (0.1 M), as well as being non-selective as the change in concentration for any solute would affect the signal.[13] The channel flow cell (CFC) method has proven a powerful technique in studying dissolution through delivering a very high mass transport. However, the visualisation of diffusion profiles requires further analysis through coupling CFC with different techniques such as magnetic resonance imaging, which has a low spatial and temporal resolution,[14] and UV-visible spectroscopy, where the absorption spectra can be obtained at steady state. Still, obtaining dynamic information about diffusion profiles changing with time are more challenging.[15]

SECM is extensively used for studying dissolution processes and kinetics[16−20] and visualisation of concentration profiles have been probed down to the micron size. For example previous work on enamel dissolution performed using SECM, coupled with finite element method modelling, allowed the rate of acid attack at a steady state condition to be quantified.[6,21] However, the temporal resolution of SECM images is quite low as acquiring an image can take from tens of minutes to up to hours,[22] which makes instantaneous tracking of diffusion fields and activities challenging.

Attempts to visualise dynamic proton fluxes have been performed using micro-electrode ion flux estimators (MIFE) where it is possible to simultaneously measure the flux of several different ion species.[23] Nevertheless, it also requires other *ex-situ* visualisation techniques such as SEM, interferometry or profilometry[24] but their use is limited due to their relatively low temporal resolution (*ca.* 5 s).[25] This

is particularly slow in comparison to techniques such as confocal laser scanning microscopy (CLSM) which has a temporal resolution in the order of milliseconds.[26] Recently, Unwin and co-workers have successfully employed fluorescence confocal laser scanning microscopy CLSM to monitor the concentration profile at an electrode surface during an electrochemical reaction.[27–29]

In this chapter, we describe the use of CLSM, coupled with SECM, as a new approach for visualising and quantifying the proton dispersion at the electrode surface, as well as their interaction with enamel surfaces to obtain time transient kinetics for enamel acid dissolution. The effect of a well-known enamel erosion inhibitor fluoride[30–32] have been investigated, through dynamic time dependent measurements. The effect of the temporary barriers formed due to treatment on the enamel surface has been assessed. The CLSM-SECM technique was supported by the theoretical treatment of finite element method modelling (FEM) to reach better understanding of dissolution under different experimental conditions. As highlighted herein, coupling CLSM with SECM turns out to be an even more powerful technique, with higher temporal (milliseconds) and spatial (sub-micron) resolution, thus extending the range of processes that can be investigated.

3.3 Experimental

3.3.1 Materials and Solutions

All aqueous solutions were prepared using Mili-Q water with typical resistivity > 18.2 MΩ cm at 25° C (Millipore Corporation). The CLSM experiments were carried out in 8 µM disodium fluorescein aqueous solutions in 0.1 M solution of KNO_3, 66 µM $CaCl_2$, and 20 µM Na_2HPO_4. pH of the solution was adjusted to ∼7.8 using 0.1 M $NaOH$. Treatment solution was 26 mM (1000 ppm) NaF. All chemicals were purchased from Sigma-Aldrich and used as received.

3.3.2 Sample Preparation

Glass surface samples were prepared by flame sealing glass capillaries (o.d. 2.0 mm, i.d. 1.16 mm, Harvard Apparatus), then polishing them back on a polishing wheel to a roughness of 3.0 µm root mean squared (RMS). Samples were then polished further down on polishing pads with 50 nm diamond lapping particles (Buehler, Germany) to 1.5 ± 0.6 nm RMS.

The process of preparing enamel samples were described in previous work.[33] Briefly, Bovine enamel blocks (6×6 mm) were cut to manageable size 2×2 mm and polished on a polishing wheel to a roughness of 3.0 µm (RMS), then they were polished further down on microcloths (Struers,UK - grade MD-Dura) with 50 nm diamond lapping particles (Buehler, Germany) to produce a roughness of 1.5 ± 0.6 nm (RMS). Enamel specimens were then rinsed and mounted onto glass capillaries (*o.d.* 2.0 mm, *i.d.* 1.16 mm, Harvard Apparatus) using Araldite (Huntsman International LLC, UK). Samples to be treated were placed in treatment solution (1000 ppm, NaF) for two minutes then rinsed with Mili-Q water.

3.3.3 Experimental Setup

The confocal fluorescence imaging was performed *via* a Leica TCS SP5X Supercontinuum laser scanning confocal microscope mounted on a Leica DMI6000 CS inverted microscope using 488 nm excitation wavelength (Ar laser) and detector window 480-570 nm, and 8000 Hz line scanning frequency with a 10 ×/ 0.3 HC PL Fluotar dry lens. Figure 3.1a depicts a schematic of the experimental set-up for proton flux visualisation at the electrode surface. The horizontal Teflon cell with two facing apertures housing the ultra-micro electrode (UME) and the substrate holder was fitted to the microscope stage, where a glass window on the bottom of the cell allowed visualisation of the gap between the electrode surface and the sample surface. The UME tip was positioned vertically at a fixed distance (20 µm) from

the substrate surface *via* XYZ-micropositioner (PI Instrument, XYZ translation) for optimum displacement. Figure 3.1b is a zoom in on the gap between the UME and substrate.

Two types of CLSM images were acquired. The *xyt* images, where a series of *xy* frames were recorded with time, each image was 512×512 pixel and took 0.43 s to be recorded (Figure 3.1d). In the *xyt* mode optical micrographs of the UME and the sample were recorded in each experiment (Figure 3.1c), and overlaying of them allowed the accurate positioning of the Pt disc at the center of the image for qualitative study. However, for quantitative analysis, *xt* images were acquired by continuously scanning a single line, 10 µm away from the UME surface for a fixed period of time. The signal was line averaged over four lines to improve the signal to noise ratio and normalised at the maximum intensity (temporal resolution $\sim$ 2 ms), where the resulting image of 1024×2048 pixel would take 4 s to be recorded. Figure 3.1b outlines the scanned line in the *xt* images. A two electrode galvanosatic arrangement with a platinum reference/counter electrode, and a UME as working electrode (25 µm diameter Pt disc, RG 10, was fabricated as reported previously)[34] were used herein. Anodic current was applied at the working electrode to produce a proton flux *via* water oxidation

$$H_2O \rightleftharpoons 2H^+ + \frac{1}{2}O_2 + 2e^- \tag{3.1}$$

Well-defined proton flux for high resolution time (sub-millisecond) was achieved *via* a home-built galvanostat with a less than 1 ms rise time for 20 nA current (Figure 3.2). To ensure time correlation between CLSM and electrochemical application, the galvanostat was triggered by using the CLSM (Leica Trigger Unit connected to the galvanostat using a DAQpad-6015, National Instruments).

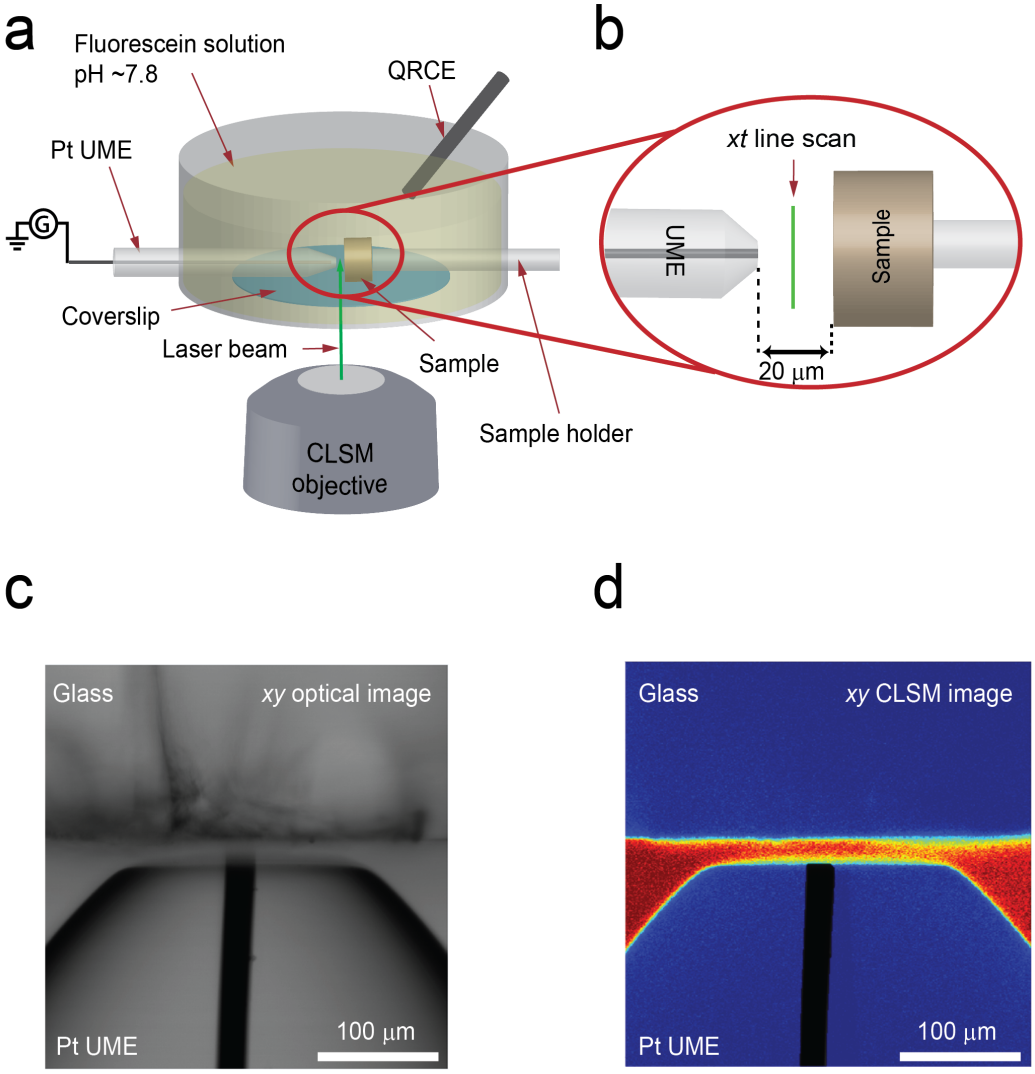

Figure 3.1: A schematic (not to scale) of the CLSM-SECM set-up where (a) the Teflon cell with the UME and sample inserted in and immersed in fluorescein solution, (b) schematic of the gap between the UME and the sample detailing the *xt* scan line, (c) Typical optical image of the Pt UME and a glass sample depicting the 20 µm gap in between, (d) An *xy* confocal image (fluorescence intensity) of the gap between the Pt UME and a glass surface (note that the Pt wire inside the UME is not visible in the fluorescence image, instead the optical image has been overlapped with the confocal image for illustration purposes).

The Galvanostat

Production of protons *via* water oxidation was achieved using a home-built galvanostat. The galavanostat consisted of a control unit and a locally positioned head unit

to minimise noise interference. Bipolar current range was controlled *via* range selection and a reference voltage from the control unit. The principal active element of the galvanostat circuit employed an ultralow input bias current operational amplifier AD549L (Analogue Devices Inc, Norwood, MA, USA) where the reference electrode is held at a virtual ground and the desired current is delivered from the working electrode. The control unit incorporated a precision voltage reference REF102BP (Texas Instruments Inc, Dallas, TX, USA), precision analogue switch MAX325CPA (Maxim Integrated Products, Sunnyvale, CA, USA) with external trigger, external reference input and saturation monitor circuitry. A triangular wave/pulse generator was employed (Colburn Electronics, Coventry, UK) as an external potential source to set the applied current. A range of currents were applied to the probe tip, from 10 to 40 nA to obtain different proton fluxes. This galvanostat was tested and showed a rise time of *ca.* 1 ms for current of 20 nA (Figure 3.2). To ensure time correlation between CLSM and the electrochemical application, the galvanostat was triggered by the CLSM (Leica Trigger Unit connected with galvanostat past DAQpad-6015, National Instruments).

3.3.4 FEM Simulation

A two-dimensional axisymmetric finite element method (FEM) model has been built to mimic the experimental setup of the proton diffusion profile generated at the UME in bulk, as well as in proximity of the sample surface. Simulations were constructed in Comsol Multiphysics (version 5.0), using the *transport of diluted species* and *chemical reaction engineering* modules. All simulations were run using a workstation (Dell Precision T3610 CTO Base, 64 GB RAM, Intel® Xeon® Processor E5-1620 v2, operating system windows 8).

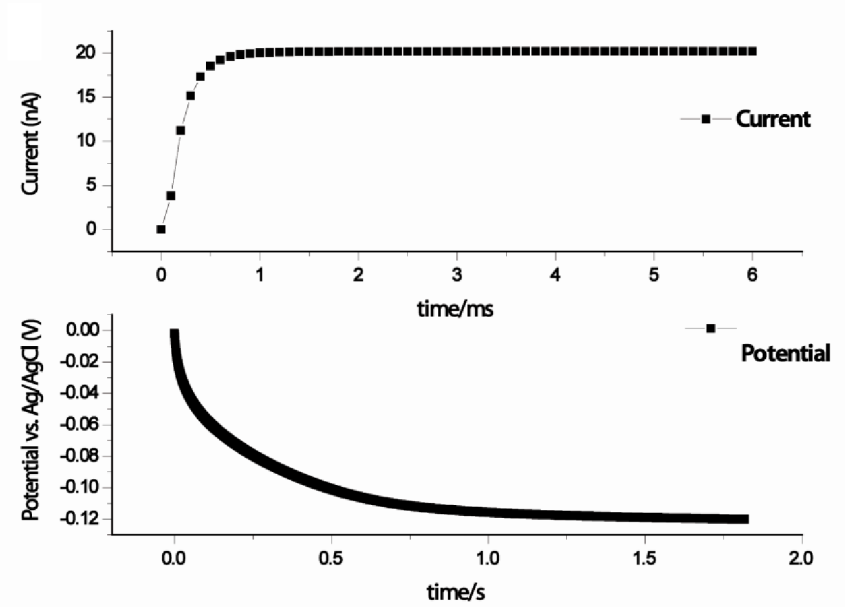

Figure 3.2: Illustration of anodic current *vs.* time (top), and UME potential *vs.* time (bottom). Note different time scale on each graph.

FEM Model Details

The geometry of the model mimicked the experimental setup, employing an ultra-microelectrode UME of radius $r_0 = 12.5$ µm with a glass shield of radius $r_1 = 125$ µm (RG = 10). For simulations of bulk experiments (Figure 3.3a) the height and width of the simulated bulk domain were $h = 150$ mm and $w = 75$ mm respectively, and no sample was present in those simulations. For simulations where an enamel sample was present, the geometry is represented in Figure 3.3b and the domain height is $h = 75$ mm, boundary B3 represent the enamel sample with a radius $r_2 = 3$ mm which is situated at $d = 20$ µm away from the UME surface. All the boundary conditions are listed in Table 3.1.

The solution in all simulations contained fluorescein, phosphate buffer, calcium ions, potassium nitrate as back ground electrolyte and carbonic acid resulting from the dissolved atmospheric CO_2. All equilibrium and dissociation constants were corrected for activity coefficient and all species initial concentrations were cal-

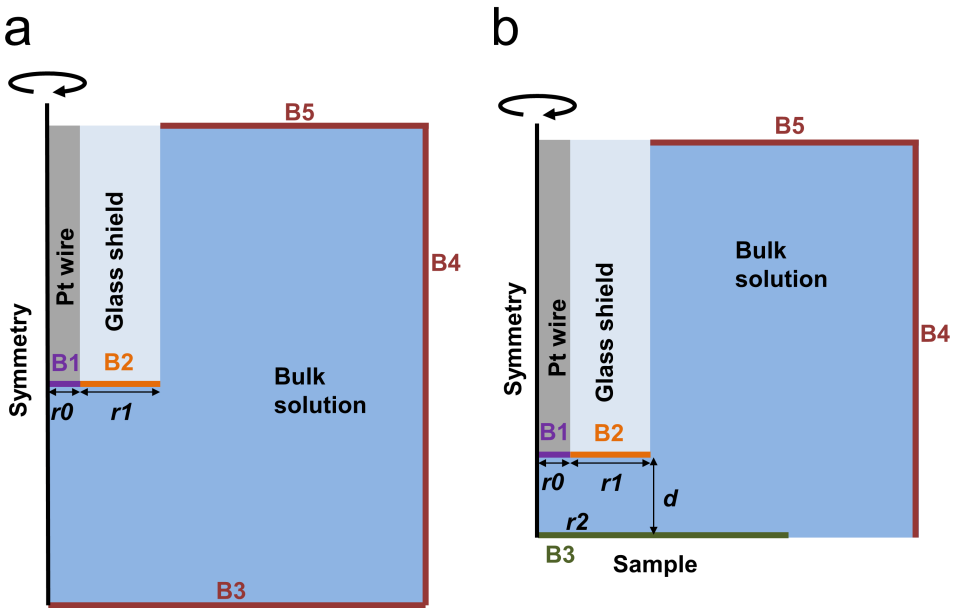

Figure 3.3: Schematic not to scale of the finite element method model geometry illustrating all boundaries and axis of symmetry for a) bulk experiment simulations, b) acid attack on enamel sample simulations.

Table 3.1: Boundary Conditions applied in the FEM model.

Boundary	**Bulk simulation condition/Fig 3.3a**	**Sample simulation condition/Fig 3.3b**
B1	$J_{H^+} = i_0/(nF\pi r_0^2)$	$J_{H^+} = i_0/(nF\pi r_0^2)$
B2	$J_i = 0$	$J_i = 0$
B3	$c_i = c_{0,i}$	$J_{H^+} = -k_0\ [H^+]$ $J_{HPO_4^{2-}} = \frac{6}{8}\ k_0\ [H^+]$ $J_{Ca^{2+}} = \frac{10}{8}\ k_0\ [H^+]$
B4-B5	$c_i = c_{0,i}$	$c_i = c_{0,i}$

culated using MINEQL+ Chemical Equilibrium Modeling System (v4.6). Instantaneous concentrations were governed by the equilibria listed in Table 3.2.

Table 3.2: List of all the equilibrium reactions governing the various species in the FEM model.[6,27,35]

Eq	**Reaction**	$\mathbf{p}K_{eq}/\mathbf{p}K_a$
R3.1	$CO_{2(g)} + H_2O_{(l)} \rightleftharpoons H_2CO_{3(aq)}$	1.466
R3.2	$H_2CO_{3(aq)} \rightleftharpoons H^+_{(aq)} + HCO^-_{3(aq)}$	6.351
R3.3	$HCO^-_{3(aq)} \rightleftharpoons H^+_{(aq)} + CO^{2-}_{3(aq)}$	10.330
R3.4	$CaCO_{3(aq)} \rightleftharpoons Ca^{2+}_{(aq)} + CO^{2-}_{3(aq)}$	10.330
R3.5	$H_2O_{(l)} \rightleftharpoons H^+_{(aq)} + OH^-_{(aq)}$	13.997
R3.6	$H_3PO_{4(aq)} \rightleftharpoons H^+_{(aq)} + H_2PO^-_{4(aq)}$	2.16
R3.7	$H_2PO^-_{4(aq)} \rightleftharpoons H^+_{(aq)} + HPO^{2-}_{4(aq)}$	7.21
R3.8	$HPO^{2-}_{4(aq)} \rightleftharpoons H^+_{(aq)} + PO^{3-}_{4(aq)}$	12.32
R3.9	$H_2Fl_{(aq)} \rightleftharpoons H^+_{(aq)} + HFl^-_{(aq)}$	4.3
R3.10	$HFl^-_{(aq)} \rightleftharpoons H^+_{(aq)} + Fl^{2-}_{(aq)}$	6.4

3.4 Results and Discussions

3.4.1 Theory and Simulation

The enamel acid induced dissolution has received extensive attention due to its wide implication in oral science which would aid the development of new dental restorative materials.[6,36] Confocal spectroscopy has previously been applied to many aspects of oral health including dental erosion,[37,38] monitoring the differences between fluoridated and non-fluoridated permanent and deciduous enamel,[39] visualising enamel

rods[40] and monitoring fluid flow through dentine tubules and substances which subsequently block the tubules,[41] although the application were only at steady state conditions.

Enamel is mainly composed of calcium hydroxyapatite, $Ca_{10}(PO_4)_6(OH)_2$, (HAP) while the remaining being organic material and water. An acidic medium can dissolve hydroxyapatite crystals as per equation 3.2, which is usually defined as surface demineralisation.[42]

$$Ca_{10}(PO_4)_6(OH)_{2(s)} + 8H^+_{(aq)} \rightleftharpoons 10Ca^{2+} + 6HPO_4^{2-} + 2H_2O \tag{3.2}$$

An interesting property of HAP is the ability to exchange its hydroxyl groups with anions such as fluoride ions, forming fluorapatite or calcium di-fluoride at the surface and decrease the rates of apatite mineral dissolution in acid media.[43,44]

The FEM model described herein was built to better understand the first-order heterogeneous attack of protons (produced at the electrode surface) on the enamel surface. The enamel surface was considered to be flat throughout the experiment due to the short time it is exposed to the proton flux (4 s).

Briefly, the finite element model produces a concentration map within the domain of all the relevant species as a function of time, wherein dissolution rate constants describe the first-order heterogeneous attack of protons (produced at the UME) on the enamel surface. The flat surface of the enamel sample consumes the protons generated at the electrode following the overall reaction equation 3.2. The dissolution leads to a flux of soluble species at the surface, with the shape of the surface considered to stay flat over time of the experiment (4 s) as the dissolution occurs. Ions are considered as point charges, Ionic transport was considered to be merely controlled through diffusion, as high background electrolyte eliminates the effect of ion migration under the electric field. Fick's second law equation was solved

for all species in the simulated domains to generate a concentration map over time:

$$(\frac{\partial c_i}{\partial t}) = D_i \bigtriangledown^2 c_i + R_i \tag{3.3}$$

where c_i and D_i represent the concentration and diffusion coefficient of species i respectively. R_i is the net generation from equilibration reactions in solution, $\bigtriangledown$ is the gradient operator in axisymmetric cylindrical co-ordinates. A list of diffusion coefficients used are reported in Table 3.3. All species in solution were under equilibrium conditions arising from water, carbonic acid and phosphoric acid dissociation equilibria governed by the equations illustrated in Table 3.2 .

Table 3.3: List of diffusion coefficients of various species in the FEM model.[45]

Species	Ca^{2+}	H^+	OH^-	K^+	Cl^-	H_2CO_3
Diffusion coefficient (10^{-9} m^2 s^{-1})	0.792	7.8	5.273	1.957	2.032	1.185
Species	HCO_3^-	CO_3^{2-}	H_3PO_4	$H_2PO_4^-$	HPO_4^{2-}	PO_4^{3-}
Diffusion coefficient (10^{-9} m^2 s^{-1})	1.185	0.932	0.882	0.959	0.759	0.759

3.4.2 Fluorescence Intensity / pH Calibration Curve

Fluorescein (pKa = 6.43)[46] is used herein as a visual pH indicator, its pH sensitivity lies between 5 and 7, with no fluorescence under pH 5 and no increase in fluorescence at pH above 7 as illustrated in Figure 3.4. The calibration curve for intensity *vs.* pH was obtained by measuring the intensity of fluorescence for a fluorescein solution (8 µm Fluorescein, 0.1 M KCl) at different pH values. The curve demonstrates a sigmoidal relationship[47] which is in agreement with previous work.[27–29] In order to obtain the fitting parameters for the curve, a background *xt* image of the full fluorescence solution was taken before applying the anodic current in each

experiment. A zero fluorescence image was captured after each experiment at a pH value between 1 and 2. Fluorescein is found to be most sensitive at 50% fluorescence intensity which corresponds to pH 6.1 as illustrated in Figure 3.4. To measure the pH changes induced by the water oxidation at the UME surface, a pH 6.1 front was tracked over time in means of radial distance from the UME center. This enables the plotting of radial distance increase over time to facilitate the visualisation of the proton diffusion profile.

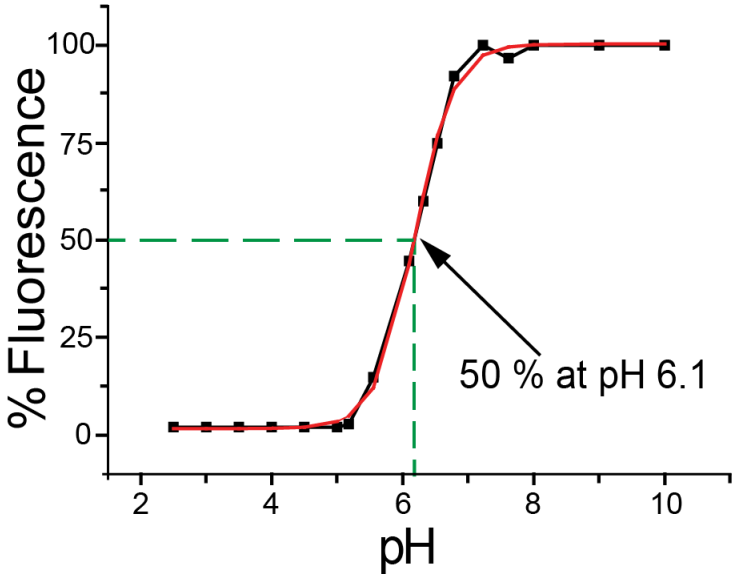

Figure 3.4: Illustration of experimental pH *vs.* intensity of fluorescence (black line) after fluorescein excitation at 488 nm and detection at 530 nm. And sigmoidal Boltzmann fit (red line).[29]

3.4.3 CLSM visualising of enamel dissolution

CLSM enables the tracking of pH changes as a function of change in fluorescence intensity of a pH sensitive fluorophore . Herein, Fluorescein is used (pk_a 6.43)[46] where no fluorescence was observed below pH 5 and no increase in fluorescence intensity occurred above pH 7. The background image was subtracted from the experimental image to cancel any shadowing effect casted by the relatively big enamel sample

(2×2 mm).

Figure 3.5 (a1-a5) illustrates how protons gradually spread along the glass surface, which forms a largely impermeable barrier, filling the gap between the UME and the glass substrate before diffusing into bulk solution. The second series of images, Figure 3.5 (b1-b5), shows the same current applied to the tip of the UME, with an enamel substrate. In the case of enamel, the overall spread of protons was confined due to the uptake of protons during the dissolution of the sample. A large spread of protons is indicative of an inert surface, whereas a small spread of protons represents significant proton flux towards the substrate due to a dissolution process as per equation 3.2.

The schematics in Figure 3.5 (c and d), highpoint the impact upon the shape of the pH profile next to glass and enamel surfaces, which indicates that the flux of protons produced was consumed by the enamel surface. This visualisation highlights clearly how CLSM can be used to distinguish between essentially inert and reactive interfaces. The lateral spread of protons, taken at 50% fluorescence intensity equivalent to pH = 6.1 (Figure 3.4), is tracked and plotted as a radial distance from the center of the electrode against time for analysis and for FEM theoretical fitting.

In spite of the apparent difference in proton profile spreading between the two samples, this imaging mode suffers from low temporal resolution with $\sim$ 0.43 s required to record one image. For higher time resolved experiments a transient xt scan of the fluorescence intensity between the tip of the UME and the enamel surface was recorded by scanning a single line at 10 µm distance from the electrode over time as illustrated schematically in Figure 3.1b (temporal resolution $\sim$ 2 ms).

3.4.4 Bulk Experiments and Model Validation

The FEM model was validated by experimentally generating a pH profile dispersion map in the absence of any sample for a range of anodic currents. Bulk solution experiments were performed where the UME was positioned in the Teflon cell without

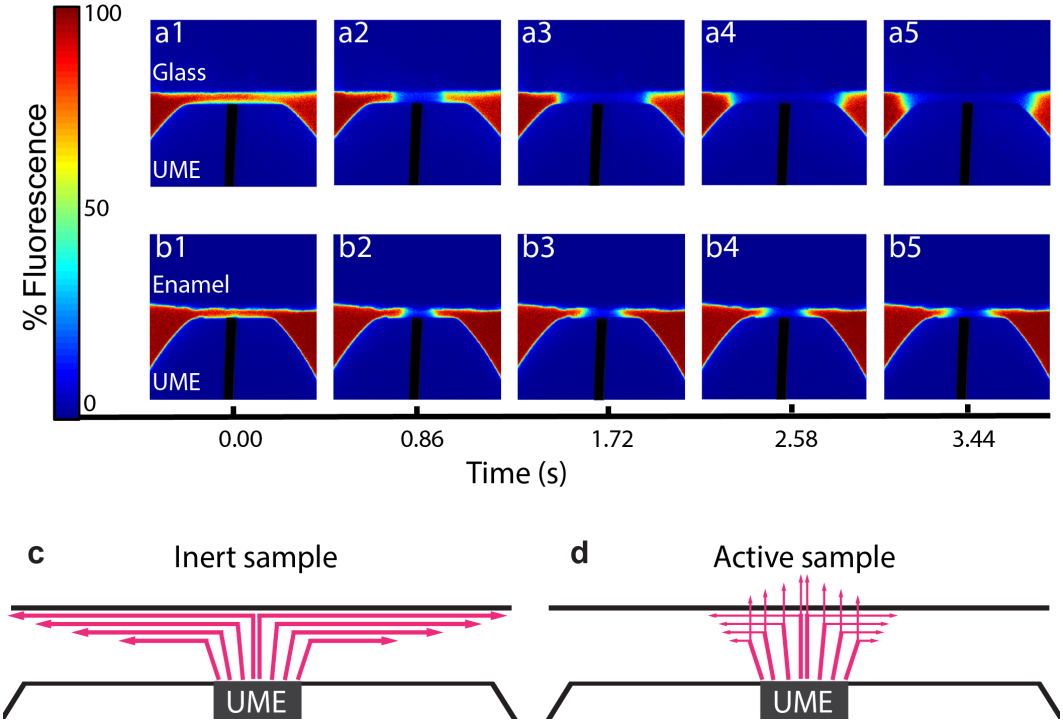

Figure 3.5: A series of *xy* confocal frames for an inert glass surface showing the wide spreading of the dynamic proton diffusion profile, for times a1) 0 s, a2) 0.86 s, a3) 1.72 s, a4) 2.58 s, a5) 3.44 s. And another series for an active enamel substrate depicting the intake of protons at the substrate surface, thus decreasing the lateral diffusion of the proton profile, also at times b1) 0 s, b2) 0.86 s, b3) 1.72 s, b4) 2.58 s, b5) 3.44 s. c) An illustration highlighting the effect of an inert sample that causes a wide proton dispersion next to the surface. d) Another illustration of the active sample that consumes protons, causing the proton dispersion profile to shrink.

a sample. The cell was filled with the fluorescein solution and a series of anodic currents 10, 20 and 30 nA were applied while acquiring the *xt* images (Figure 3.6a - c). A numerical FEM model mimicking an electrochemical water oxidation reaction at a UME surface in bulk solution was constructed. All species concentrations along with activity corrected equilibrium and dissociation constants for the fluorescence solution composition were obtained using MINEQL+ Chemical Equilibrium Modeling System software (v 4.6). Subsequently, the experimental results were fitted with the theoretical model analysis for bulk measurements. Figure 3.6d illustrates the experimental radial distance of the pH 6.1 front over time for three anodic currents

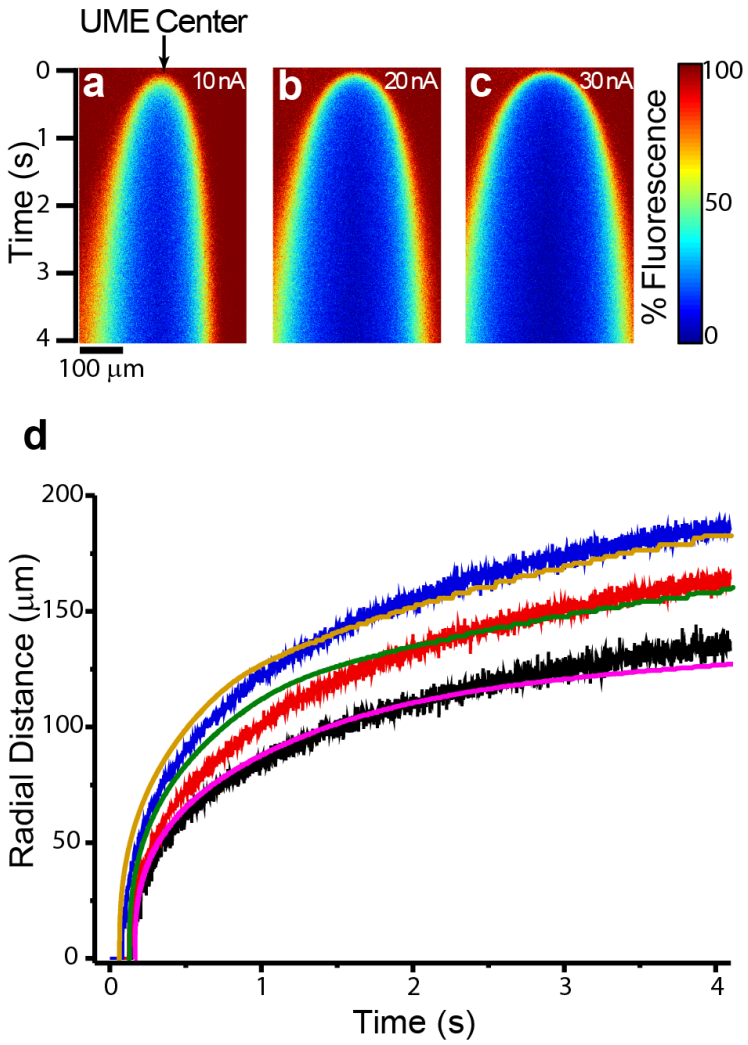

Figure 3.6: Confocal *xt* images illustrating the change in fluorescence intensity at a single scanned line over time, when a UME is situated in bulk solution without a substrate, for an anodic current of a) 10 nA. b) 20 nA. and c) 30 nA. d) Experimental profiles of the radial distance *vs.* time dependence at 50% intensity (pH = 6.1) in bulk solution under an anodic current of 10 nA (black line), 20 nA (red line) and 30 nA (blue line). And theoretical radial distance *vs.* time under an anodic current of 10 nA (pink line), 20 nA (green line) and 30 nA (brown line).

(see caption for color code), an increase in the value of the applied current results in a larger radial distance of the pH 6.1 front, corresponding to wider dispersion of the proton profile as expected. After four seconds the radial distance of the pH 6.1 reaches 135 ± 3, 162 ± 3 and 186 ± 3 µm for 10, 20 and 30 nA respectively.

The theoretical fitting produced through the FEM model predicts similar values for the pH front radial distance after four seconds, however for the first 1.5 seconds the model predicts higher values for the radial distance, this could be due to many factors, such as processes occurring on the platinum surface that are not accounted for in the model, or natural convection in the otherwise macroscopically still solution as suggested by Amatore et al.[48] Nevertheless, the predicted values of the proton profile dispersion by the FEM model are still in good agreement with the experimental data.

3.4.5 Enamel Dissolution

Shown in Figure 3.7a-3.7d are *xt* fluorescence images of untreated enamel surface for a 10, 20, 30 and 40 nA anodic currents. The high proton intake of the enamel surface results in a long delay of the proton profile dispersion, where for 10 nA the pH 6.1 front do not reach the scanned line even after 4 seconds (fluorescence intensity of *xt* image at 10 nA is higher than 50%, Figure 3.7a). However, for subsequent currents the radial distance increases with increasing current value, due to the higher proton fluxes generated at the electrode surface.

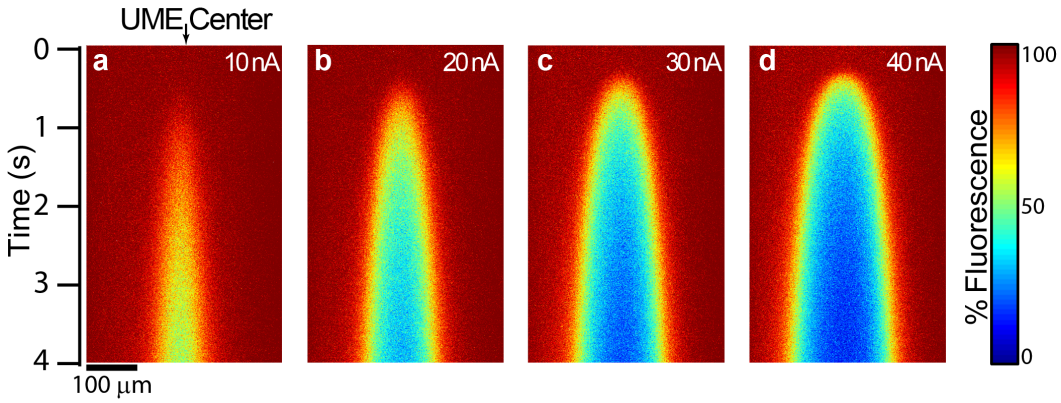

Figure 3.7: Confocal *xt* images illustrating the fluorescence intensity at the scan line over time, for an untreated enamel substrate, and an anodic current of a) 10 nA. b) 20 nA. c) 30 nA. and d) 40 nA.

The fluoride-treated enamel presents a lower proton intake, where the proton

dispersion extends to larger radial distance than the untreated enamel ones, as depicted in Figure 3.8a-3.8d. For a 10 nA current the pH 6.1 front reaches the scanned line after less than half a second, showing the inherent differences between an untreated surface, and a fluoride-treated surface.

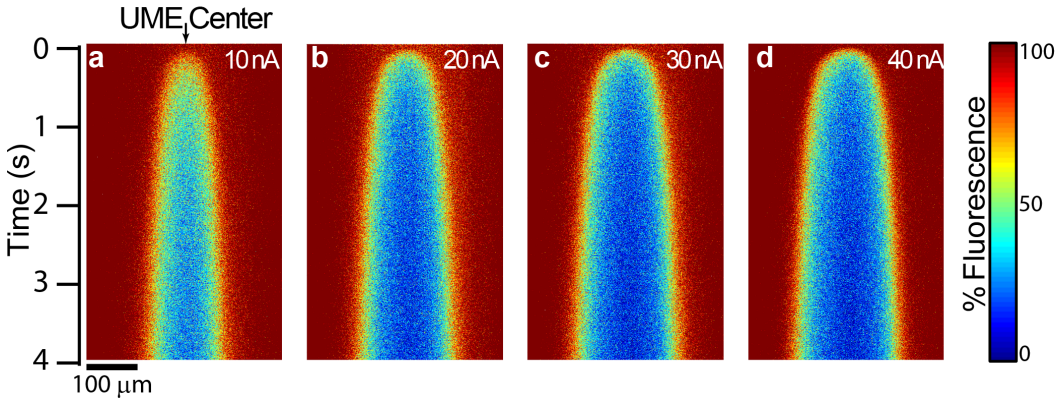

Figure 3.8: Confocal *xt* images illustrating the fluorescence intensity at a single scanned line with time, for fluoride-treated enamel substrate, under an anodic current of a) 10 nA. b) 20 nA. c) 30 nA. and d) 40 nA.

Figure 3.9a-3.9c illustrates the advances of the pH 6.1 front over time for fluoride-treated (red line) and untreated (black line) samples at 20, 30 and 40 nA. The fluoride-treated enamel demonstrates not just a larger radial distance of the proton profile dispersion but also a shorter delay in pH 6.1 front reaching the scanned line. The proton profile diffusion expansion is attributed to lower proton intake by the fluoride-treated samples compared to the pristine enamel. Values of radial distance of the pH 6.1 front for both untreated and fluoride-treated enamel are listed in Table 3.4. This highlights the distinct inhibitory impact that fluoride has upon the size and shape of the proton profiles produced. Fluoride-treated enamel provides more resistance to acid attack than untreated enamel alone. For 20 nA generation current, untreated enamel pH profile spreads to 23 ± 5 µm compared to the fluoride-treated profile which spreads to 61 ± 5 µm, giving a rise of *ca.* 38 µm due to lower intake of protons which last for the whole 4 second experiment. Interestingly, For 30 nA the difference in radial distance between fluoride-treated

and untreated sample drops to *ca.* 19 µm, and for 40 nA it drops further down to 10 µm. Hence, by decreasing the anodic current, thus the proton flux, the fluoride barrier lasts longer as displayed in Figure 3.9.

Table 3.4: Experimental radial distance of pH 6.1 front for untreated and fluoride-treated enamel at 20, 30 and 40 nA anodic current.

Anodic current i (nA)	**Untreated enamel radial distance µm**	**Treated enamel radial distance µm**
20	23 ± 5	61 ± 5
30	62 ± 5	81 ± 5
40	80 ± 5	90 ± 5

Another note, is the extended delay for the pH 6.1 front to reach the scanned line at untreated enamel samples, which varies from 3.31 ± 0.3 s at 20 nA to 1.61 ± 0.3 s at 30 nA and 1.19 ± 0.3 s at 40 nA, compared to the much shorter delays for fluoride-treated enamel, 0.50 ± 0.1 s at 20 nA and 0.26 ± 0.1 s at 30 and 0.19 ± 0.1 s at 40 nA (see Figure 3.9, and Table 3.5). The amount of protons generated inside the small gap between the UME and the enamel during the delay time could be calculated easily using the following equation:

$$[H^+]^* = \frac{i}{F} t_{delay} \tag{3.4}$$

where i is the applied anodic current, F is the Faraday constant and t_{delay} is the delay time for the pH 6.1 front to reach the scanned line. Values of the delay times along calculated equivalent protons are listed in Table 3.5 *vide infra.* Higher proton consumption is evident for the untreated-enamel, *ca.* 5 times higher, than those for fluoride-treated samples.

Table 3.5: List of time delays and consumed protons values for fluoride-treated and untreated enamel samples corresponding to different anodic currents.

Anodic current i (nA)	**Surface Treatment**	**Time delay (s)**	**Protons equivalent (mol)**
20	Untreated	3.31 ± 0.3	6.7 ± 1.2 $\times 10^{-13}$
30	Untreated	1.61 ± 0.3	5.0 ± 1.2 $\times 10^{-13}$
40	Untreated	1.19 ± 0.3	4.9 ± 1.2 $\times 10^{-13}$
20	Fluoride	0.50 ± 0.1	1.0 ± 0.4 $\times 10^{-13}$
30	Fluoride	0.26 ± 0.1	0.8 ± 0.4 $\times 10^{-13}$
40	Fluoride	0.19 ± 0.1	0.8 ± 0.4 $\times 10^{-13}$

3.4.6 Insights from Simulations

The finite element model produces pH profile maps as a function of time, corresponding to different dissolution rate constants (k_0) for enamel samples. Snapshots of the produced pH maps for a 20 nA current and $k_0 = 0.03$ cm s^{-1} at 1, 50, 100 and 1000 ms time intervals are illustrated in Figure 3.10 as an example. These theoretical data were used to plot radial distance of the pH 6.1 front from the electrode center against time, a set of curves are shown for a 30 nA current and a range of k_0 values in Figure 3.11. The displacement of theoretical 50% intensity profiles expand with time, as expected for a proton induced dissolution process, plus a shorter radial distance with increasing k_0 is reported. This is because a greater rate constant leads to higher consumption of protons at the substrate surface. Figure 3.9 shows the experimental displacements of 50% intensity profiles (pH 6.1) at untreated and fluoride-treated enamel for a current of 20, 30 and 40 nA, which are compared to the theoretical fitted profiles described earlier. Therefore, in case of treated samples, the presence of the fluoride inhibitor significantly retards the rate of enamel dissolution.

The fluoride treatment protects the enamel surface by forming fluorapatite which increases the proton spread on the surface and considerably slows the dissolution rate. The experimental and the simulated 50% intensity profiles for enamel samples are different, where the initial rise curves are more pronounced and much sharper compared to the experimental ones. Radial distance curves are still being analysed through the simulations at the time of writing this thesis.

As mentioned previously, all experiments were carried out at three currents, 20 nA, 30 nA and 40 nA. For all the applied currents, the generated radial distance curves suffers from a time delay of the proton profile advances as mentioned in the previous section. Those delays are significantly longer at an untreated than at fluoride-treated enamel. This could be attributed to the buffering effect resulting from the dissolution of enamel at pH = 7.8. The definite composition of the gap solution is not yet defined, but previous studies on bones dissolution reveals that HAP (the main mineral in both enamel and bone composition) would dissolve at neutral pH values (pH = 7). The concentration of calcium ions were found to be 210±80 µM at 1 mm distance from the bone sample. However, in our experiment the gap of interest is very small (20 µm), this would give rise to accumulation of phosphate buffer in the solution in between, that is generated from the sample surface due to enamel dissolution, which would explain the delay.

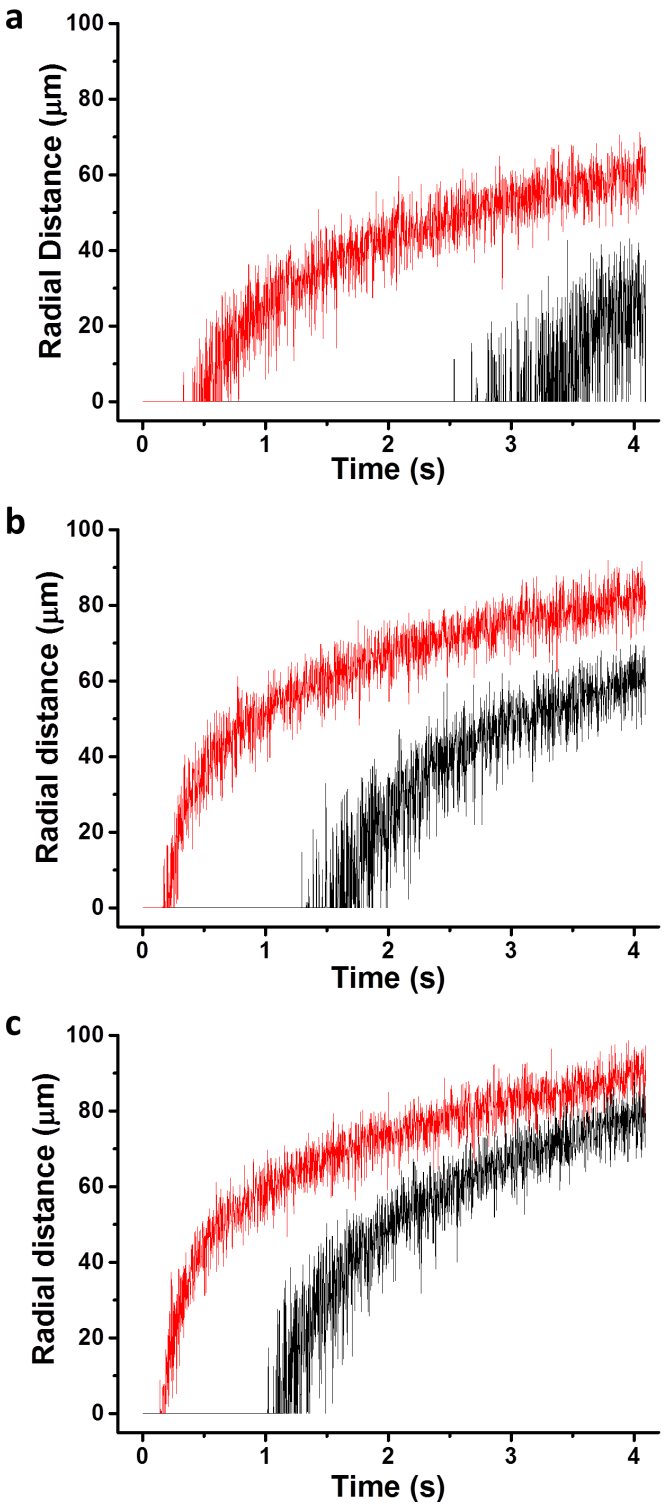

Figure 3.9: Radial distance *vs.* time experimental profiles dependence at 50% intensity (pH = 6.1) for untreated enamel (black lines) and fluoride-treated enamel (red lines) under an anodic current of a) 20 nA, b) 30 nA and c) 40 nA.

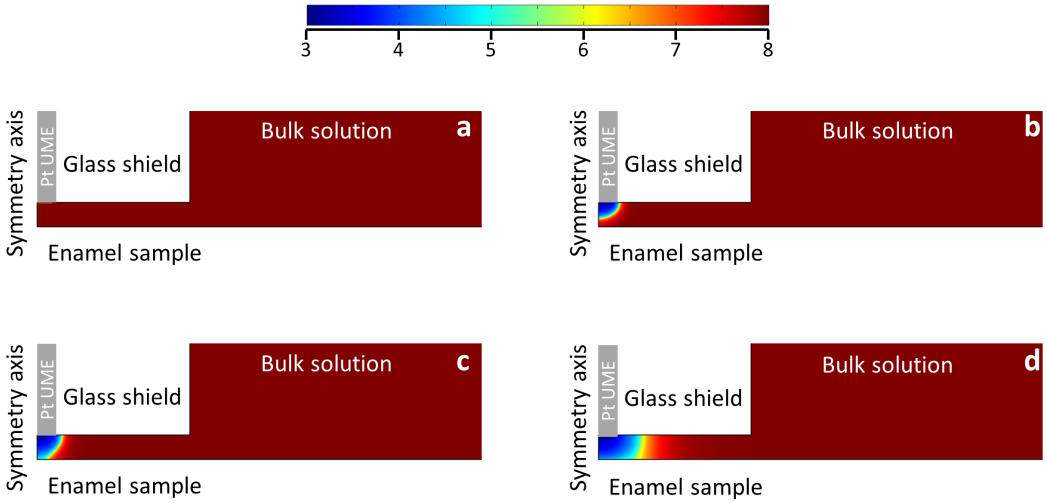

Figure 3.10: Snapshots of the theoretical pH profile maps produced through the FEM model for k_0 value of 0.03 and 20 nA at a) 1 ms, b) 50 ms, c) 100 ms and d) 1 s time intervals.

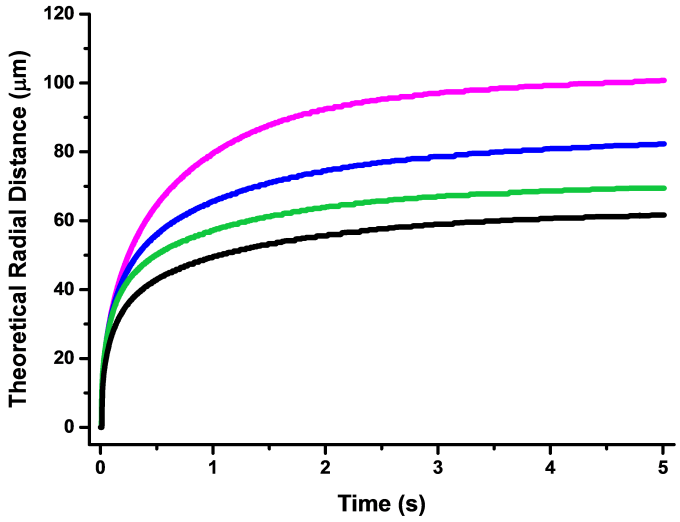

Figure 3.11: Radial distance *vs.* time theoretical profiles dependence at 50% intensity (pH = 6.1) for k_0 value of 0.001 (pink line), 0.003 (blue line), 0.008 (green line) and 0.010 cm s^{-1} (black line) under 30 nA anodic current.

3.5 Conclusions

SECM -CLSM was successfully employed to image proton diffusion in a thin layer of solution at the surface of enamel. This new technique provides an analytical method with high spatial and temporal resolution permitting millisecond analysis of treatment effects on enamel substrates. It permits direct visualisation of the surface reaction and presents itself as a new technique for assessing the proton dispersion on surfaces and indeed for assessing the effectiveness of inhibitors on substrates. A method has been developed which uses microelectrode generated pH challenges combined with CLSM to image proton diffusion and dissolution at the surface of enamel. Localised dissolution of dental enamel has been achieved by the application of a proton flux to the enamel surface from a UME positioned in close proximity to the enamel surface. It has been shown that fluoride change the morphology of the fluorescent profile that forms compared to untreated enamel due to its barrier effect. A time delay was detected in all enamel experiments for the pH 6.1 front advances towards the scanning line (10 µm away from the tip). This delay is thought to be related to a surface phenomenon where a change in the composition of the gap solution is induced by the sample surface, as mechanical polishing of the enamel may change the chemical composition at the surface.

Modelling of the data using the finite element method model has indicated that acid erosion does occur at both untreated and treated enamel surfaces, but the dissolution rate was slower in case of the treated sample. A range of the dissolution rate constants were varied for simulations at three different currents of 20, 30 and 40 nA in a bet to fit the pH profile transient. However, the time delay was not predicted by the theoretical model due to the lack of information of solution composition inside the tip-substrate gap at the moment. Plans are made to investigate the composition using other techniques to extract further informations that could be used in the simulation.

These experiments broaden the potential applications of CLSM-SECM in assessing the proton dispersion on surfaces and indeed for assessing the effectiveness of inhibitors on substrates. Further work will seek to apply the technique to investigate lateral proton diffusion near different substrates.

3.6 References

(1) Pidaparti, R.; Neblett, E.; Miller, S.; Alvarez, J. *Smart. Mater. Struct.* **2008**, 17, 015001.

(2) Lillard, R. S.; Willcutt, G. J.; Pile, D. L.; Butt, D. P. *J. Nucl. Mater.* **2000**, 277, 250-262.

(3) Lillard, S.; Gac, F.; Paciotti, M.; Ferguson, P.; Willcutt, G.; Chandler, G.; Daemen, L. In *Effects of Radiation on Materials: 20th International Symposium*, Rosinski, S. T. G. M. L. A. T. R. K. A. S., Ed., 2001, pp 631-643.

(4) Kreuer, K. D. *Chem. Mater.* **1996**, 8, 610-641.

(5) Wu, H. P.; McCreery, R. L. *Anal. Chem.* **1989**, 61, 2347-2352.

(6) McGeouch, C.-A.; Edwards, M. A.; Mbogoro, M. M.; Parkinson, C.; Unwin, P. R. *Anal. Chem.* **2010**, 82, 9322-9328.

(7) Bengtsson, A.; Sjoberg, S. *Pure Appl. Chem.* **2009**, 81, 1569-1584.

(8) McLarnon, F. R.; Muller, R. H.; Tobias, C. W. *Appl. Opt.* **1975**, 14, 2468-2472.

(9) Tvarusko, A.; Watkins, L. S. *Electrochim. Acta.* **1969**, 14, 1109-1118.

(10) Compton, R. G.; Unwin, P. R. *J. Electroanal. Chem., Interfac. Electrochem.* **1986**, 205, 1-20.

(11) Snowden, M. E.; Unwin, P. R.; Macpherson, J. V. *Electrochem. Commun.* **2011**, 13, 186-189.

(12) Mbogoro, M. M.; Snowden, M. E.; Edwards, M. A.; Peruffo, M.; Unwin, P. R. *J. Phys. Chem.* C **2011**, 115, 10147-10154.

(13) Jan, C. C.; McCreery, R. L. *Anal. Chem.* **1986**, 58, 2771-2777.

(14) Zhang, C.; Werth, C. J.; Webb, A. G. *J. Contam. Hydrol.* **2008**, 100, 116-126.

(15) Tam, K. Y.; Wang, R. L.; Lee, C. W.; Compton, R. G. *Electroanalysis* **1997**, 9, 219-224.

(16) Macpherson, J. V.; Unwin, P. R. *J. Phys. Chem.* **1994**, 98, 1704-1713.

(17) Macpherson, J. V.; Unwin, P. R. *J. Phys. Chem.* **1994**, 98, 11764-11770.

(18) Macpherson, J. V.; Unwin, P. R. *J. Phys. Chem.* **1995**, 99, 3338-3351.

(19) Macpherson, J. V.; Unwin, P. R. *Prog. React. Kinet. Mech.* **1995**, 20, 185-244.

(20) Macpherson, J. V.; Unwin, P. R. *J. Phys. Chem.* **1996**, 100, 19475-19483.

(21) McKelvey, K.; Snowden, M. E.; Peruffo, M.; Unwin, P. R. *Anal. Chem.* **2011**, 83, 6447-6454.

(22) Cornut, R.; Poirier, S.; Mauzeroll, J. *Anal. Chem.* **2012**, 84, 3531-3537.

(23) Newman, I. A. *Plant. Cell. Environ.* **2001**, 24, 1-14.

(24) Shellis, R. P.; Finke, M.; Eisenburger, M.; Parker, D. M.; Addy, M. *Eur. J. Oral Sci.* **2005**, 113, 232-238.

(25) Shabala, L.; Roos, T.; McMeekin, T. *Microbiol. Aus.* **2004**, 3, 39-40.

(26) Pawley, J. *Handbook of biological confocal microscopy, 3rd ed.*; Springer: Winconsin, 2006.

(27) Rudd, N. C.; Cannan, S.; Bitziou, E.; Ciani, L.; Whitworth, A. L.; Unwin, P. R. *Anal. Chem.* **2005**, 77, 6205-6217.

(28) Cannan, S.; Macklam, I. D.; Unwin, P. R. *Electrochem. Commun.* **2002**, 4, 886-892.

(29) Grime, J. M. A.; Edwards, M. A.; Rudd, N. C.; Unwin, P. R. *Proc. Natl. Acad. Sci. U. S. A.* **2008**, 105, 14277-14282.

(30) Arends, J.; Christoffersen, J.; Christoffersen, M. R.; Schuthof, J. *Caries Res.* **1983**, 17, 455-457.

(31) Attin, T.; Meyer, K.; Hellwig, E.; Buchalla, W.; Lennon, A. M. *Arch. Oral Biol.* **2003**, 48, 753-759.

(32) Wiegand, A.; Meier, W.; Sutter, E.; Magalhaes, A. C.; Becker, K.; Roos, M.; Attin, T. *Caries Res.* **2008**, 42, 247-254.

(33) Parker, A. S.; Patel, A. N.; Al Botros, R.; Snowden, M. E.; McKelvey, K.; Unwin, P. R.; Ashcroft, A. T.; Carvell, M.; Joiner, A.; Peruffo, M. *J. Dent.* **2014**, 42, S21-S29.

(34) Wightman RM., W. D., Bard AJ. *Electroanalytical Chemistry*; Dekker: New

York, 1989; Vol. 15.

(35) McGeouch, C.-A.; Peruffo, M.; Edwards, M. A.; Bindley, L. A.; Lazenby, R. A.; Mbogoro, M. M.; McKelvey, K.; Unwin, P. R. *J. Phys. Chem. C* **2012**, 116, 14892-14899.

(36) Lippert, F.; Parker, D. M.; Jandt, K. D. *Surf. Sci.* **2004**, 553, 105-114.

(37) Hjortsjo, C.; Jonski, G.; Thrane, P. S.; Saxegaard, E.; Young, A. *Caries Res.* **2009**, 43, 449-454.

(38) Heurich, E.; Beyer, M.; Jandt, K. D.; Reichert, J.; Herold, V.; Schnabelrauch, M.; Sigusch, B. W. *Dent. Mater.* **2010**, 26, 326-336.

(39) Sonju Clasen, A. B.; Ogaard, B.; Duschner, H.; Ruben, J.; Arends, J.; Sonju, T. *Advances in dental research* **1997**, 11, 442-447.

(40) Radlanski, R. J.; Renz, H.; Willersinn, U.; Cordis, C. A.; Duschner, H. *Eur. J. Oral Sci.* **2001**, 109, 409-414.

(41) Williams, C. G.; Macpherson, J. V.; Unwin, P. R.; Parkinson, C. *Anal. Sci.* **2008**, 24, 437-442.

(42) Margolis, H. C.; Zhang, Y. P.; Lee, C. Y.; Kent, R. L.; Moreno, E. C. *J. Dent. Res.* **1999**, 78, 1326-1335.

(43) Amjad, Z.; Koutsoukos, P. G.; Nancollas, G. H. *J. Dent. Res.* **1981**, 60, 450-450.

(44) LeGeros, R. Z. *J. Dent. Res.* **1990**, 69 Spec No, 567.

(45) Haynes, W. M. *CRC Handbook of Chemistry and Physics, 93rd Edition*; Taylor & Francis, 2012.

(46) Sjöback, R.; Nygren, J.; Kubista, M. *Spectrochim. Acta, Part A* **1995**, 51, L7-L21.

(47) Marquardt, D. W. *J. Soc. Ind. Appl. Math.* **1936**, 11, 431-441.

(48) Amatore, C.; Szunerits, S.; Thouin, L.; Warkocz, J.-S. *J. Electroanal. Chem.* **2001**, 500, 62-70.

(49)Bergera, C.E.M.; Horrocks, B.R.; Datta, H.K. *Electrochim. Acta* **1999**, 44,

2677-2683.

Chapter 4

Dual Functional Ion Selective Microelectrode - Scanning Ion Conductance Microscopy (ISME-SICM) Probe: Fabrication and Characterisation

Al Botros R.; Souza Castro P.; Paulose Nadappuram B.; Colburn A. W.;
Bertotti M. and Patrick R. Unwin

In preparation

4.1 Abstract

Herein, we report the fabrication and use of a dual channel probe, combining the topographical mapping and localised delivery capabilities of a scanning ion conductance microscopy (SICM) probe with an ion selective microelectrode (ISME) for simultaneous topography and ion concentration profiling of surfaces and interfaces. These probes were fabricated from a laser pulled sharp-ended glass theta pipette, where one of the barrels of the pipette was filled with electrolyte solution and a QRCE was inserted in it to produce the SICM part. The other barrel was silanised prior to being filled with calcium ionophore, then an electrical contact was established to form the ISME tip. Two types of electrical contact were constructed for the later barrel; a liquid-based contact through a QRCE inserted in back filled $CaCl_2$ solution, and a solid-contact through a poly 4,3-ethylenedioxythiophene (PEDOT) coated carbon microfiber that was inserted directly in the membrane. The solid-contact gave a higher stability with time, thus was used for the imaging of samples. The capabilities of the SICM-ISMEs were demonstrated by employing them to investigate the dissolution of calcite microcrystals under different environments. This enabled the extraction of kinetics information related to the dissolution fluxes at different pH values through coupling probe measurements with finite element method (FEM) modelling. The obtained values were in good agreement with literature reported ones.

4.2 Introduction

The detecting of ion concentration in aqueous media and across surface-liquid interfaces using ion selective electrodes (ISEs) is of great importance in a wide range of fields, such as clinical analysis, environmental sciences, agriculture and toxicity detection.[1–5] Thus, global interest in understanding and further improving

the functionality of ISEs has produced a massive volume of work over the last few decades.[6–8] Conventional potentiometric microelectrodes are fabricated from silanised laser pulled sharp-ended glass capillaries filled with ionophore membrane and an inner solution that contains a certain concentration of the ion of interest. A QRCEs is then inserted in the aqueous based solution to form the electrical contact.[9] Innovations in this field involved introducing new ionophore membrane and inner filling solution compositions to provide higher selectivity and lower detection limits.[1] A major development step was introducing the solid-contact which involved inserting an electrode directly into the membrane.[10] To obtain high stability measurements, the electrode is coated with a conductive polymer such as poly(3,4-ethylenedioxythiophene) (PEDOT),[11] polypyrrole,[12] polythiophene,[13] and polyaniline.[14] Miniaturising of ISEs is receiving more interest, as detecting traces of ions in smaller volumes is becoming increasingly important. Ion selective microelectrodes (ISMEs) have been explored for decades due to their low cost, ease of fabrication, high sensitivity and compact size.[15,16] However, potentiometric probe miniaturisation is limited by the stability of measurements according to the size of the tip due to high interfacial resistance.[17]

Scanning ion conductance microscopy (SICM), is an imaging technique which utilises a glass micro- or nanopipette filled with electrolyte solution and a QRCE inserted within the filling solution. A current runs between the QRCE in the pipette and that in bulk solution with a value corresponding to the resistance of both the solution and the end of the probe.[18] The direct current value can be used as a feedback signal to maintain a set distance between the surface and the probe, thus tracking the topography of the substrate.[19] Furthermore, modulating the probe z-position generates an alternating current component (i_{AC}) that when used as a feedback signal provides a robust distance control with high resolution.[20] Another application of the SICM technique includes localised delivery, where the reagent of interest is added to the probe inner filling solution and delivered locally and directly

to the studied surface.[21]

Herein, we couple the ISME and SICM capabilities to make a dual function probe, that measures the concentration of ions and tracks the topography simultaneously. The size of the fabricated probes ranged from 1.5 to 3 µm in diameter. The fabrication of such probes at the micron scale has been reported previously, however, no data have been reported due to the complexity of their fabrication.[16] In this work, the ISME-SICM probe was used successfully for imaging calcite microcrystals during the dissolution process at neutral pH 6.8, and under acid induced dissolution conditions. Kinetic information were extracted with the use of finite element method simulations, allowing the calculation of surface dissolution fluxes. Values extracted from the model were in good agreement with those reported in literature.

4.3 Experimental

4.3.1 Materials

Potassium chloride (KCl), calcium chloride dihydrate ($CaCl_2.2H_2O$), sodium bicarbonate ($NaHCO_3$), ethanol (C_2H_5OH), 4,3-ethylenedioxythiophene ($EDOT$), dichlorodimethylsilane ($(CH_3)_2SiCl_2$), calcium ionophore I (cocktail A- $ETH1001$), N-(Trimethylsilyl)dimethylamine ($TMSDMA$), and 1-butyl-3-methyl-imidazolium-hexafluorophosphate ($BMIM^+PF_6^-$) were obtained from Sigma-Aldrich. Hydrochloric acid (HCl), sodium hydroxide ($NaOH$) and sulfuric acid (H_2SO_4) were purchased from Fischer Chemistry. All chemicals used were reagent grade. All solutions were freshly prepared using Milli-Q water (Millipore Corp.) with resistivity of *ca.* 18.2 MΩ cm at 25°C.

4.3.2 Preparation of ISME-SICM Probes

The ISME-SICM probes were fabricated using borosilicate theta capillaries (30-0114, Harvard Apparatus). Prior to fabrication, the capillaries were cleaned by soaking them in a 1 M H_2SO_4 solution for 24 hours followed by a thorough washing with water and ethanol to completely remove traces of acid. The capillaries were then dried in an oven, for 4 hours at 180° C and were stored in air tight containers until used. The cleaned capillaries were pulled into sharp pointed pipettes (typical diameter 1.5 - 3 µm) by a laser puller (P-2000, Sutter Instruments) using a custom-developed program (Line 1: Heat 450, Fil 3 Vel 23, Del 150, Pul 30, Line 2: Heat 415, Fil 2 Vel 18, Del 150, Pul 50, Line 3: Heat 430, Fil 2 Vel 18, Del 135, Pul 40).

To fabricate the probe, one of the barrels of the pulled pipette was silanised by holding the end of the probe at 200° C and passing TMSDMA vapor through the barrel for 5 minutes, while maintaining a constant flow of argon (4 bar) through the other barrel. The probes were then baked at 120° C in an oven for 1 hour to complete the silanisation process. The unsilanised barrel, filled with electrolyte and inserted with an Ag|AgCl QRCE, formed part of the ion conductance cell for SICM feedback control. The silanised barrel filled with calcium ion selective membrane formed the potentiometric electrode for calcium concentration measurements. Two different electric contact configurations were employed herein to achieve electrical connection to the ion selective membrane, namely the liquid-contact (Figure 4.1b and c) and solid-contact (Figure 4.1d and e). In the case of the liquid-contact, the barrel containing the ion selective membrane was back filled with 100 mM $CaCl_2$ solution (inner filling solution)[1] and an Ag|AgCl QRCE was inserted into the solution to complete the contact (Figure 4.1b). In the second configuration, a solid-contact was prepared from a carbon microfiber (6 µm of diameter, glued to a thin copper wire using silver epoxy) by electro polymerisation of EDOT. The electropolymerised end was then inserted to about 50 -100 µm depth into the ion selective membrane

(Figure 4.1e).

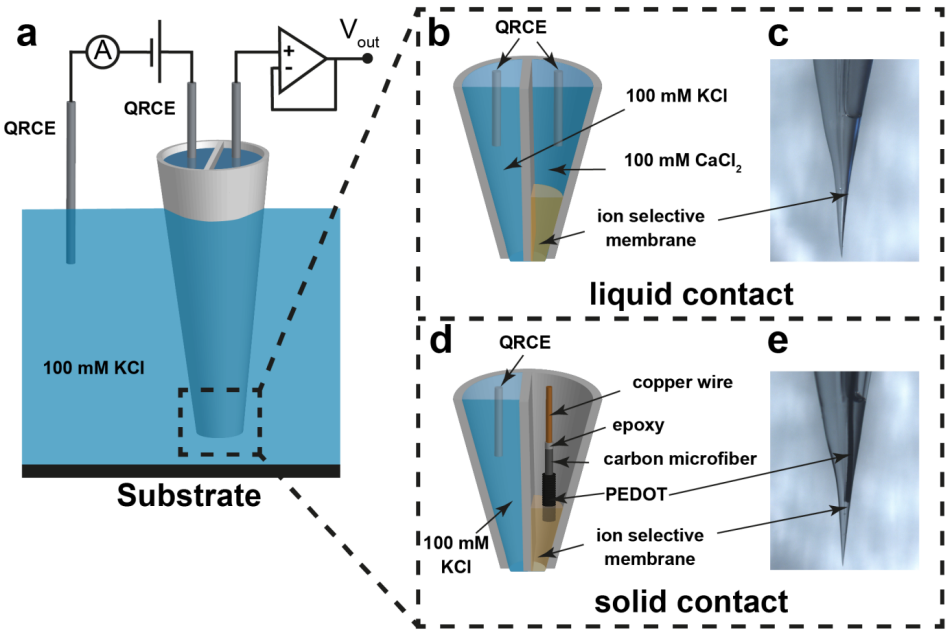

Figure 4.1: a) Schematic representation of an ISME-SICM experiment setup. b) Schematic of an ISME-SICM probe employing liquid-based contact. The barrel containing the ion selective membrane (right barrel) was back filled with 100 mM $CaCl_2$ solution (inner filling solution) and an Ag|AgCl QRCE was inserted into the solution to complete the contact. c) Optical micrograph of a typical ISME-SICM probe employing liquid-based contact. d) Schematic of an ISME-SICM probe employing solid-contact. The barrel containing the ion selective membrane (right barrel) was inserted with a carbon microfiber coated with PEDOT to complete the contact. e) Optical micrograph of a typical ISME-SICM probe employing solid contact.

Preparation of PEDOT solid-contact

The PEDOT solid-contacts were prepared by following a method described previously.[22] Briefly, a 100 mM 3,4-ethylenedioxythiophene (EDOT) was dissolved in 1-Butyl-3-methylimidazolium hexafluorophosphate ($BMIM^+PF_6^-$) ionic liquid solvent, and nitrogen gas was purged through the solution for 10 minutes to remove any traces of oxygen. The carbon fiber, working electrode, was dipped into the solution along with a Ag|AgCl QRCE and a platinum wire as a reference and a counter electrodes respectively. Electropolymerisation of EDOT at the carbon microfiber was achieved

through cyclic voltammetry, wherein the potential of the carbon fiber was swept from -0.9 to 1.3 V at a scan rate of 50 mV s^{-1}. The electropolymerised EDOT (PEDOT) was further doped by sweeping the potential from -0.9 to 0.8 V at a scan rate of 50 mV s^{-1}. Figure 4.2a and 4.2b display a typical cyclic voltammogram recorded during the electropolymerisation of EDOT and the doping of PEDOT respectively. The doped PEDOT was then tested by recording cyclic voltammograms in 100 mM KCl from -0.4 to 0.5 V (vs. Ag|AgCl) at a scan rate of 50 mV s^{-1} (Figure 4.2c). An optical micrograph of a typical PEDOT solid-contact after doping is shown in Figure 4.2d.

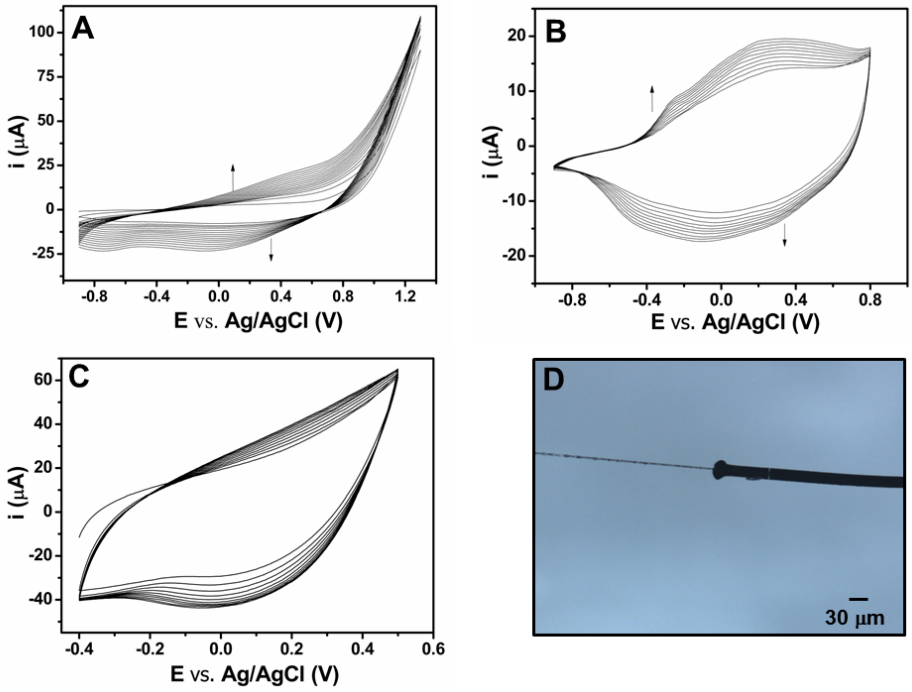

Figure 4.2: Solid-contact preparation by electropolymerisation of EDOT in carbon microfiber using 100 mM EDOT in $BMIM^{+}PF_6^{-}$, scan rate 50 mV s^{-1}. a) Cyclic voltammograms recorded during the electropolymerisation of EDOT at the carbon microfiber. b) Cyclic voltammograms recorded during the doping of PEDOT at the carbon microfiber in $BMIM^{+}PF_6^{-}$ ionic liquid, scan rate 50 mV s^{-1}. c) Cyclic voltammogram of the doped PEDOT in 100 mM KCl solution, scan rate 50 mV s^{-1}. d) Optical micrograph of typical PEDOT coated carbon microfiber.

4.3.3 Preparation of Calcite Microcrystals

The calcite microcrystal samples were prepared by a precipitation process described previously.[23] Briefly, equal volumes of solutions of 10 mM calcium chloride and 10 mM sodium bicarbonate (pH 10.5) were mixed in a petri dish and left closed in a clean environment for 4 hours. The microcrystals formed at the base of the dish, with typical dimensions *ca.* 25 µm × 25 µm surface area and 15 - 20 µm height, were washed thoroughly with Milli-Q water and dried with a stream of nitrogen and left undisturbed for a week prior to use.[23]

4.3.4 Instrumentation

The probe was mounted on a piezoelectric positioner (P-611, 3S Nanocube), which in turn was mounted on an inverted optical microscope (Axiovert 40 CFL, Zeiss). The current in the SICM barrel was measured using a home-build current-to-voltage converter. A lock-in amplifier (SR830, Stanford Research Systems) was used to generate the driving signal for the oscillation of the probe position and to determine the magnitude and phase of the AC ion current. Data recording as well as the probe position and voltage output control, were carried out using a self-written LabVIEW (2013, National Instruments) program through an FPGA card (7852R, National Instruments). The output impedance of ion selective electrodes is very high, typically ranging from 107 to 109 Ω. Any current drawn from the electrode to make a voltage measurement leads to an error generated by the voltage drop due to the electrode impedance. To minimise such errors, the effective input impedance of the measuring amplifier must be very much higher than the output impedance of the ion selective electrode so that current draw is minimised. A custom-built voltage follower was employed incorporating a unity gain buffer stage using a LMP7721 operational amplifier (Texas Instruments Inc) which offers input bias current *ca.* 3 fA and effective input impedance of 8 × 1014 Ω. The amplifier was in the SOIC-8

package and mounted on a PTFE based printed circuit board with input guard ring traces to preserve the low current performance of the device.

4.3.5 ISME-SICM Measurement Protocol

All electrical measurements were performed inside a Faraday cage. For the ISME-SICM experiments, the SICM barrel was filled with either 100 mM KCl (pH 6.8) solution for dissolution at neutral pH, or with a 100 mM KCl solution containing 0.1 mM HCl (pH 3.8) for the acid induced dissolution experiments. The probe-substrate distance was controlled using an AC amplitude feedback control scheme that is described previously.[18] Briefly, a bias of 0.1 V was applied to the Ag|AgCl QRCEs inside the SICM barrel versus the QRCE in the bulk solution, to induce an ion DC current. The probe z-position was oscillated (200 nm peak-peak amplitude, 69.23 Hz) to generate an alternating current (i_{AC}) component on the ion current (i_{DC}) when the probe is positioned close to the sample. This i_{AC} was measured via a lock-in amplifier (SR830, Stanford Research Systems), and the magnitude of i_{AC} was used as a feedback signal to detect and to control the separation between the probe and the sample surface. The probe was approached to the surface until the AC ion current magnitude increased to the set-point employed (equivalent to a probe-surface separation of 300 nm), afterwards the probe was scanned over the calcite surface in hopping mode to record the topography and the change in calcium ion concentration during calcite microcrystal dissolution. The AC ion current and x, y and z positions were recorded throughout the scan and the values at the closest approach to the surface were used to construct simultaneous 3D maps of topography and calcium ion concentration around the calcite microcrystal. All the probes used herein were calibrated before and after each scan, in a 100 mM KCl solution (pH 6.8) containing calcium chloride of concentrations varying between 0.1 µM and 10 mM.

4.4 Theory and Simulations

A three dimensional finite element method (FEM) model was constructed to mimic the calcite microcrystal dissolution under the experimental conditions implemented herein. Microcrystals geometry parameters (x-y) were obtained through light micrograph of the sample, while height measurements were extracted from SICM approaches. Information regarding micropipette geometry were acquired through SEM micrographs. Simulations were generated in Comsol Multiphysics package (v4.4). All simulations were run using a workstation (Dell Precision T3610 CTO Base, 64 GB RAM, Intel® Xeon® Processor E5-1620 v2, operating system windows 8).

4.4.1 Finite element method FEM model details

The dissolution of calcite is strongly pH dependent. The following three reactions occur simultaneously on the calcite surface as proposed by Plummer et al.[24]

$$CaCO_{3(s)} + H^{+}_{(aq)} \rightleftharpoons Ca^{2+}_{(aq)} + HCO^{-}_{3(aq)} \tag{4.1}$$

$$CaCO_{3(s)} + H_2CO_{3(aq)} \rightleftharpoons Ca^{2+}_{(aq)} + 2HCO^{-}_{3(aq)} \tag{4.2}$$

$$CaCO_{3(s)} + H_2O_{(l)} \rightleftharpoons Ca^{2+}_{(aq)} + HCO^{-}_{3(aq)} + OH^{-}_{(aq)} \tag{4.3}$$

Solution composition for the experimental setup were calculated using MINEQL+ (chemical equilibrium modelling software, version 4.6), along with the activity corrected dissociation and equilibrium constants. The following equilibria in Table 4.1, describing the calcite dissolution in calcium carbonate aqueous solutions, while being open to the atmosphere, were implemented in the model. Simulations were constructed in Comsol Multiphysics package (version 4.4).

Table 4.1: Equilibria data for the calcite-H_2O system open to the atmosphere.[25]

Eq	**Reaction**	$\mathbf{p}K_{eq}/\mathbf{p}K_a$
R4.1	$CO_{2(g)} + H_2O_{(l)} \rightleftharpoons H_2CO_{3(aq)}$	1.466
R4.2	$H_2CO_{3(aq)} \rightleftharpoons H^+_{(aq)} + HCO^-_{3(aq)}$	6.351
R4.3	$HCO^-_{3(aq)} \rightleftharpoons H^+_{(aq)} + CO^{2-}_{3(aq)}$	10.330
R4.4	$CaCO^-_{3(aq)} \rightleftharpoons Ca^{2+}_{(aq)} + CO^{2-}_{3(aq)}$	10.330
R4.5	$H_2O_{(l)} \rightleftharpoons H^+_{(aq)} + OH^-_{(aq)}$	13.997

Calcite dissolution at neutral pH

A 3D FEM model that mimicked the calcite microcrystal geometry in an aqueous solution was designed (Figure 4.3), implementing the equilibria in Table 4.1. The *transport of diluted species* and the *chemical reaction engineering* modules were used to construct the numerical model. Under the conditions of this experiment (neutral pH), the dissolution process described by Equation 4.3 dominates. The ISME-SICM probe effect on the dissolution were considered to be negligible, thus it were not included in the model.

Boundaries 1-5 presented the bulk solution, while boundary 6 represent the unreactive glass surface. Boundaries 7-11 are the calcite microcrystal dissolving faces which are in contact with the solution (100 mM KCl, pH = 6.8). Boundary conditions are listed in Table 4.2. Ionic transport was considered to be governed solely by diffusion following Fick's first law. The diffusive flux of species i is given by the following equation:

$$J_i = -D_i \bigtriangledown c_i \tag{4.4}$$

where D_i, and c_i are the diffusion coefficient and concentration of species i respec-

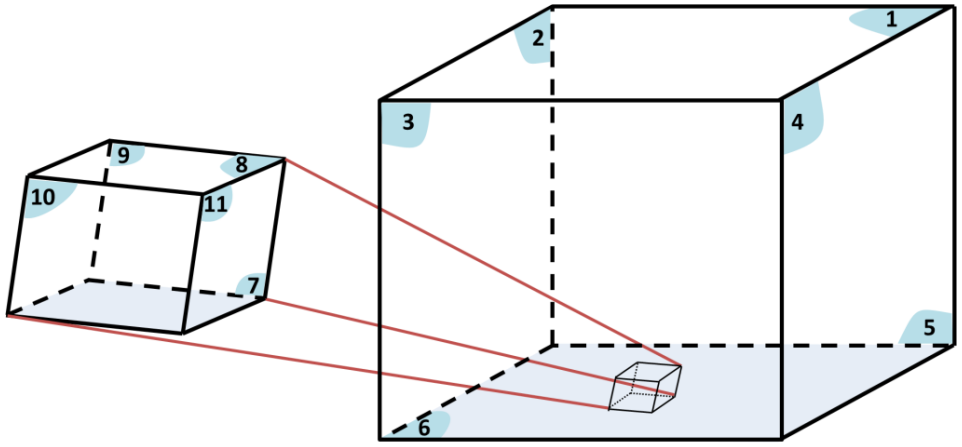

Figure 4.3: Schematic not to scale for the FEM model geometry, representing a calcite microcrystal in the bulk domain, numbers on the different faces represent the boundary numbers in the model. See Table 4.2 for boundary conditions.

tively.

Table 4.2: Boundary conditions applied in the model of calcite dissolution at neutral pH.

Boundary	**condition/Fig 4.3b**
B1-B5	$c_i = c_{0,i}$
B6	$J_i = 0$
B7-B11	$\mathbf{n}(D_{Ca^{2+}} \bigtriangledown c_{Ca^{2+}}) = J_{surf}$ $\mathbf{n}(D_{HCO_3^-} \bigtriangledown c_{HCO_3^-}) = J_{surf}$ $\mathbf{n}(D_{OH^-} \bigtriangledown c_{OH^-}) = J_{surf}$

Calcite acid induced dissolution

A 3D FEM model was constructed to mimic the geometry of a calcite microcrystal top surface, with the addition of the end of a 750 nm radius, 2.3° half-cone angle theta pipette in solution as shown in Figure 4.4. The bulk solution was at pH = 6.8 (100 mM KCl), and solution inside the SICM barrel at pH = 3.8 (100 mM KCl +

0.1 mM HCl); while the ISME was considered non-reactive as the membrane has no effect on the calcite dissolution or the calcium ions concentration. Simulations were constructed using the *transport of diluted species*, *chemical reaction engineering* and *electric current* modules. At low pH values the dissolution of calcite is dominated by the process in Equation 4.1.

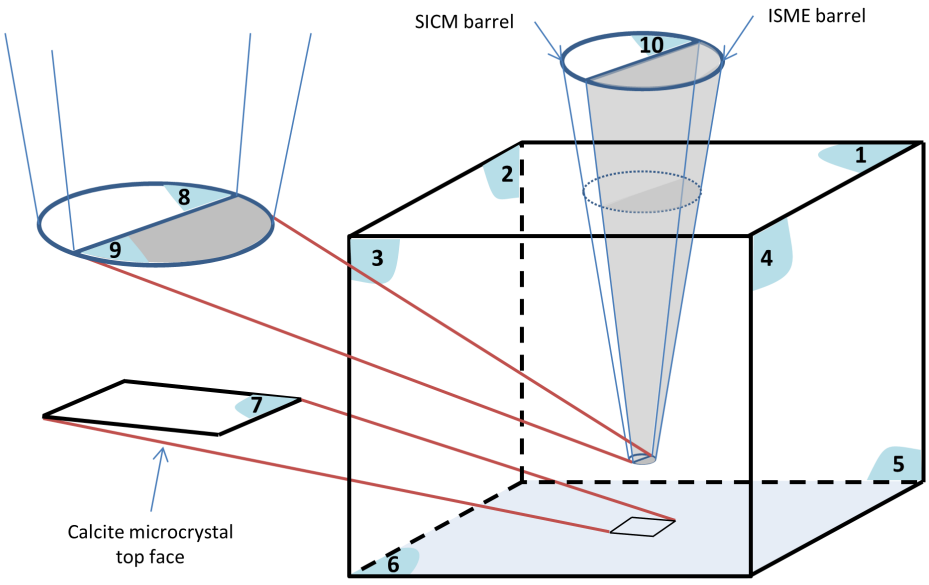

Figure 4.4: Schematic not to scale for the FEM model geometry, representing a calcite microcrystal and a ISME-SICM probe in the bulk domain. Numbers on the different faces represent the boundary numbers in the model, and the shaded half of the probe represents the ISME barrel which is not considered in the model. See Table 4.3 for boundary conditions.

Boundaries 1-5 represent the bulk solution, boundary 6 denote the non-reactive glass surface, boundary 7 is the active top surface of the calcite microcrystal, while boundaries 8 and 9 are the SICM barrel and ISME barrel tip ends respectively; boundary 10 denote the top end of the simulated SICM barrel. The study herein consisted of two stationary steps; the first one was run with boundary conditions listed in the second column of Table 4.3, to generate the dissolution diffusion profile around the microcrystal surface in bulk solution (pH 6.8). For the second step, a

steady state solution was obtained for acid induced dissolution with the probe at 300 nm distance from the surface, boundary conditions are listed in Table 4.3, third column.

Table 4.3: Boundary conditions applied in the model of acid induced calcite dissolution.

Boundary	**condition for step1**	**condition for step2**
B1-B5	$c_i = c_{0,i}$ $V = 0$ V	$c_i = c_{0,i}$ $V = 0$ V
B6, B9	$J_i = 0$	$J_i = 0$
B7	$\mathbf{n}(D_{Ca^{2+}} \bigtriangledown c_{Ca^{2+}}) = J_{surf}$ $\mathbf{n}(D_{HCO_3^-} \bigtriangledown c_{HCO_3^-}) = J_{surf}$ $\mathbf{n}(D_{OH^-} \bigtriangledown c_{OH^-}) = J_{surf}$	$J_{Ca^{2+}} = k_{!0}[H^+] + J_{surf}$ $J_{HCO_3^-} = k_0[H^+] + J_{surf}$ $J_{H^+} = -k_0[H^+]$ $J_{OH^-} = +J_{surf}$
B8	$J_i \neq 0$	$J_i \neq 0$
B10	$c_i = c_{0,i}$ $V = 0.1$ V	$c_i = c_{0,i}$ $V = 0.1$ V

The ionic transport in this model was governed by both diffusion and migration, where the flux J_i was given through the following equation:

$$J_i = -D_i \bigtriangledown c_i - \frac{z_i F}{RT} D_i c_i \bigtriangledown \phi \tag{4.5}$$

where D_i, z_i and c_i are the diffusion coefficient, charge and concentration of species i respectively. F, R and T are Faraday constant, gas constant and temperature. Diffusion coefficients used in both previous models are listed in Table 4.4.

Table 4.4: : List of diffusion coefficients of various species in the FEM model.[25]

Species	Ca^{2+}	H^+	OH^-	K^+
Diffusion coefficient (10^{-9} m^2 s^{-1})	0.792	7.8	5.273	1.957
Species	Cl^-	H_2CO_3	HCO_3^-	CO_3^{2-}
Diffusion coefficient (10^{-9} m^2 s^{-1})	1.185	0.932	2.032	1.185

4.5 Results and Discussion

4.5.1 Fabrication and Characterisation of ISME-SICM Probes

For the fabrication of the ISME-SICM probe, the inner wall of one of the barrels of the pulled pipette was silanised to keep the hydrophobic ionophore membrane attached to the glass wall. Prior to silanisation, the capillaries were subjected to an acid treatment for 24 hours. This restores the hydroxyl groups on the glass which enhances the attachment of the silane to the surface.[26] The silanisation process presented the most challenging aspect of the probe fabrication especially for small probes. Firstly, $((CH_3)_2SiCl_2)$ was used in an attempt to silanise the glass wall of the ISME barrel, but this compound usually reacts with water forming a silicone layer. Thus, the thickness of the produced film was not reproducible enough and the ISME barrel usually suffered a blockage due to this polymerisation process.[27] Alternatively, TMSDMA, which has a relatively high vapor pressure, and does not form a polymer with water nor produce a corrosive by-product, was employed successfully.[27] Furthermore, heating the capillaries up to 200° C during the application of TMSDMA vapor also ensures the absence of water vapor allowing a reproducible silanisation without blocking issues. To avoid any contact between the silane vapor and the SICM barrel, a flow of argon gas was applied into the

SICM barrel, minimising any issues arising later during the filling of the barrels with electrolyte solution. However, getting a potentiometric response from smaller ISME probes (< 1 µm diameter) was not achieved due to the high resistivity of the ionophore membrane in the small end of the tip.[12] This has prevented the miniaturisation of these probes into the nanoscale dimensions.

Employing a sensor with a liquid-based contact, calibration curves were recorded to verify the ISME response, using a range of $CaCl_2$ solutions (pCa 2 to 7 in a 100 mM KCl solution, pH = 6.8). A Nernstian ISME response was obtained correlating the open circuit potential (mV) and pCa, with a change of 31 mV for each 1 pCa unit change as depicted in Figure 4.5a. The probe was kept in a 50 mM $CaCl_2$ solution in a vertical position while not in use, and it exhibited a stable response for at least three days after fabrication, where neither calibration curves nor slope values show any significant change in potentiometric response (Figure 4.5a).

The ISME probe limit of detection was also investigated in relation to the thickness of the ionophore membrane. While the membrane thickness has no direct effect on the selectivity and response time of an ISME, thinner membranes increase the transmembrane ion fluxes and degrade detection limits.[28] Thus, a typical filling height of *ca.* 200 µm was always employed to provide a limit of detection around 0.3 µM in 100 mM KCl solution at pH 6.8.[29] The drift of potentiometric measurements employing liquid-based contact tip was investigated using a 0.1 mM $CaCl_2$ solution (pCa = 4). A drift of *ca.* 0.09 mV min^{-1} can be observed in Figure 4.5b, which could be attributed to the evaporation of the inner filling solution of the ISME barrel, and the occurrence of osmotic pressure differences across the ionophore membrane.[28,30]

The influence of the SICM bias, between the QRCE in bulk solution and the one in the SICM channel, on the potentiometric response of the ISME was investigated. Figure 4.5c shows the calibration plots of a typical ISME probe at different SICM bias values. A shift of 0.1 V in the magnitude of the open circuit

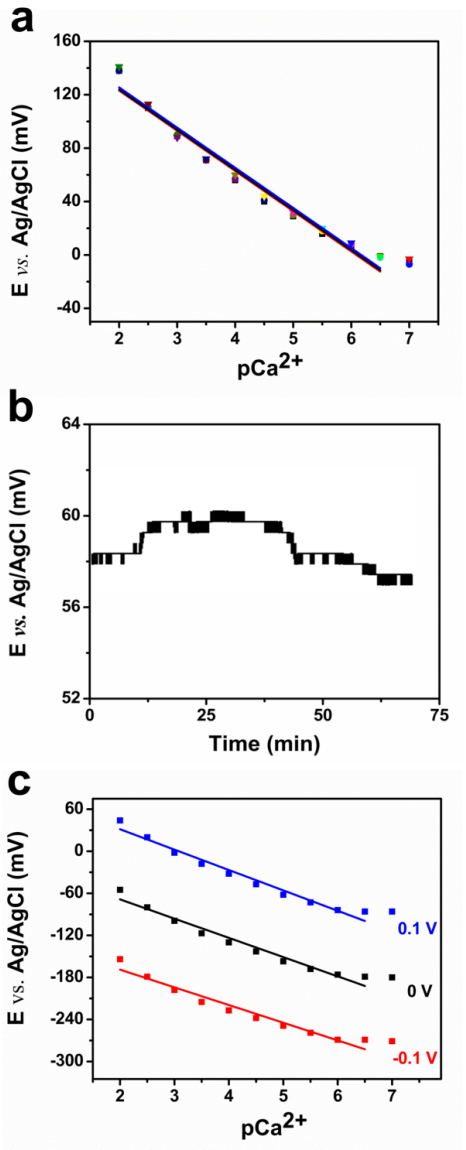

Figure 4.5: a) Calibration curves recorded for a liquid-based contact ISME with non-acid SICM tip on three consecutive days. b) Potentiometric long-term stability of the liquid-based contact sensor employing 0.1 mM $CaCl_2$ (pCa = 4) in 100 mM KCl solution at pH 6.8. c) Calibration plots of a typical ISME-SICM probe at different SICM bias values. Tip diameter: 1.5 µm

potential was observed for each 0.1 V increase in the SICM bias. However, the slope of the calibration curve remained stable (30 mV dec^{-1}) indicating that the ISME probe performance was not affected by the change in the SICM bias. A +0.1 V SICM bias was chosen to perform all experiments.

As a higher stability is required when performing imaging experiments for a longer time, a solid-contact probe was introduced. The probe exhibited a Nernstian response, with a slope of 39 mV per 1 pCa unit change, see Figure 4.6. The drift in potentiometric measurements of a PEDOT solid-contact probe was *ca.* 0.04 mV min^{-1}, see insert in Figure 4.6. The low drift in the solid-contact probe could be due to infusing the PEDOT coated electrode directly into the ionophore membrane which increases the surface contact area. Consequently, a relatively large interfacial capacitance arises, that reduces the possibility of polarisation of this interface.[12,28]

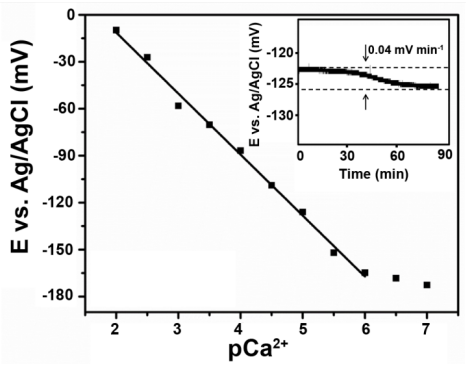

Figure 4.6: Typical calibration curve using PEDOT solid-contact sensor in $CaCl_2$ solutions between 0.1 µM and 10 mM (pCa 7 and 2, respectively) in 100 mM KCl solution at pH 6.8. Insert: potentiometric long-term stability of the sensor employing 0.01 mM $CaCl_2$ in 100 mM KCl solution at pH 6.8. Tip diameter: 3 µm.

4.5.2 Response Time of The ISME Probe

The SICM-ISME probe response time was tested using a probe with non-acid filled SICM barrel, where approach curves towards a calcite microcrystal were carried out with various approach velocities ranging from 0.1 to 8 µm s^{-1}. Figure 4.7a illustrates that the DC ion current recorded at the SICM barrel has no significant variation correlated with different approach speeds, although the noise level decreases with slowest approaches. In contrast, the potentiometric measurements shown in Figure 4.7b, which are translated into Ca^{2+} concentrations through the probe calibration curve, varies with the high velocities of the approach ($>$ 2.0 µm s^{-1}), and no sig-

nificant change is recorded for slower approach speeds ($< 1.0\ \mu m\,s^{-1}$). Thus, an approach velocity of less than $1\ \mu m\,s^{-1}$ was employed for all experimental measurements.

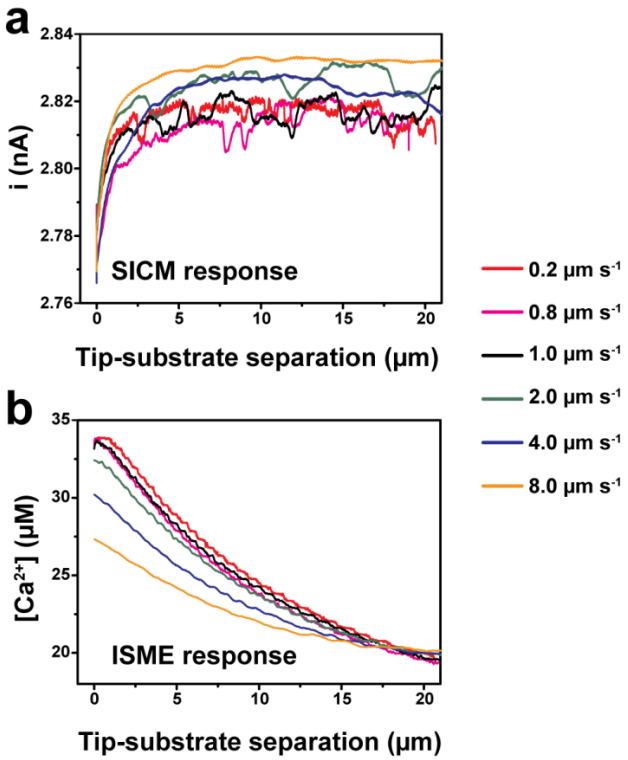

Figure 4.7: a) SICM response and b) ISME response for approach curves to the calcite microcrystal surface using the ISME-SICM probe at 0.2, 0.8, 1.0, 2.0, 4.0, 8.0 $\mu m\,s^{-1}$ velocities in 100 mM KCl solution at pH 6.8. Tip diameter: 1.5 µm.

Acid *vs.* non-acid ISME-SICM probe

The capability of the fabricated ISME-SICM probes for spatially resolved concentration profiling of interfaces were demonstrated by employing them to determine the Ca^{2+} concentration gradient associated with the pH dependent calcite microcrystal dissolution. For this, a 0.1 V bias was applied between the QRCE electrodes in the SICM barrel and in the bulk solution. Figure 4.8 shows typical ISME response for approach curves using a non-acid tip (black line) and an acid filled tip (blue line), to an inert glass substrate far away from any calcite microcrystals. This firstly con-

firms the stability of the ISME probe during the approach towards a sample, and secondly, illustrates that adding acid to the SICM barrel do not affect the ISME performance. A back ground calcium ion concentration of < 0.3 µM for an acid tip, and < 0.2 µM for non-acid tip filled with KCl solution (pH = 6.8) is recorded due to the presence of calcite microcrystals in the sample.

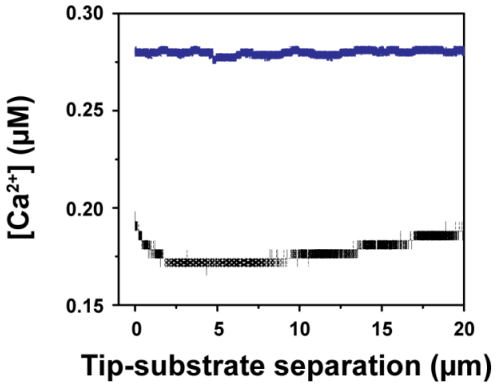

Figure 4.8: ISME response of approach curves towards glass substrate using acid filled SICM tip (blue line), and non-acid tip (black line).

Figure 4.9a illustrates two typical calibration curves obtained for the ISME barrel, with an acid filled SICM tip containing 100 mM KCl + 0.1 mM HCl at pH = 3.9 (red line and red y axis), and a SICM barrel filled with 100 mM KCl solution at pH = 6.8 (black line and black y axis). A shift in the potentiometric measurement between the two calibration curves is observed, and a small change occurred for the Nernstian slope (31 mV non-acid tips, and 40 mV acid tips).

The ISME potentiometric response translated into calcium ion concentration for two typical approach curves towards a calcite microcrystal are depicted in Figure 4.9b. The black line represents an approach that is carried out using a non-acid SICM barrel, while the red line denote the approach with an acid SICM barrel representing the acid induced dissolution. Both approaches start at 20 µm away from the microcrystal top surface, a sharper increase in the calcium ion concentration along the approach is observed with the acid tip, compared to the non-acid probe.

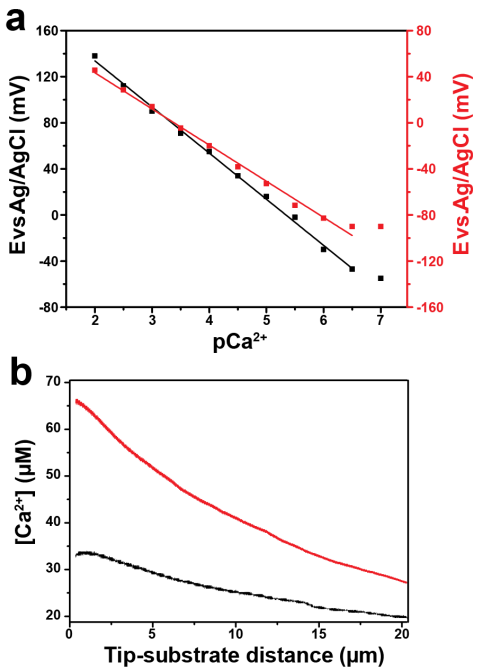

Figure 4.9: a) Calibration plots for the ISME-SICM probe using the non-acid tip containing 100 mM KCl solution at pH 6.8 (black line), and the acid tip containing 100 mM KCl + 0.1 mM HCl solution at pH 3.9 (red line) in the SICM channel, Note that the axes in (a) are colored on the graph in accordance with the graph line colors. b) ISME response for approach curves (υ = 0.6 µm s^{-1}) to the calcite microcrystal surface by using non-acid tip (black) and acid tip (red). Tip diameter: 1.5 µm.

This is attributable to the ejection of protons out of the SICM barrel towards the microcrystal surface; hence the acid induces the calcite dissolution as per equation 4.1 and thus gives rise to the concentration of calcium ions. Furthermore, the concentration of calcium ions near the microcrystal surface, *ca.* 300 nm distance, for the acid tip probe nearly doubles to that for the non-acid tip probe. For the first instance, this increase seems small compared to the pH difference between the two SICM barrels used in the experiment, pH 6.8 to 3.9. However, as the bulk solution in both cases is at pH 6.8, the proton concentration in the SICM tip that is filled with acid suffers a high drop due to the diffusion field created at the end of the tip. In fact, the drop in $[H^+]$ extends as high as 50 µm inside the SICM barrel (drop of 5% at 50 µm, and 92% at the end of the tip), which translates into an increase

in the pH value at the end of the SICM tip to reach 5.0 and further more at the microcrystal surface to be 5.1 as predicted by the FEM numerical model *vide infra*.

4.5.3 Insight from Simulation

The calcite dissolution with non-acid tip

As the calcite microcrystal dissolves to reach a steady state in the bulk solution at pH = 6.8 (as per equation 4.3), the pH near the surface increases due to the production of hydroxide ions. The diffusion profile for the calcium ions and the pH are predicted through a steady state numerical simulation (FEM model), through the application of different surface flux values to the calcite dissolving surface. Typical 2D (x-z) maps of the diffusion profile around the calcite microcrystal are depicted in Figure 4.10b (calcium concentration) and 4.10c (pH) which were obtained through the theoretical FEM model. A working curve was established by plotting the simulated calcium ion average concentration, at 300 nm away from the microcrystal surface corresponding to the SICM setpoint used herein, against the applied surface flux value (Figure 4.10a). According to this curve, the experimental calcium surface concentration 33.0 ± 0.2 µm (Figure 4.9b black line, pCa = 4.48) gives an interfacial flux of $2.82(\pm\ 0.02) \times 10^{-10}$ mol cm^{-2} s^{-1}, that is in good agreement with the values reported in literature.[31]

The calcite dissolution with acid tip

The interfacial calcite dissolution flux at pH = 6.8, obtained from the previous model, was used to reach a steady state diffusion profile around the calcite microcrystal prior to applying the acid induced dissolution study. Subsequently, a working curve shown in Figure 4.10d was generated through the acid induced dissolution at steady state, where a the average calcium concentration at 300 nm away from the crystal surface is plotted against the dissolution rate k_0. Figure 4.10e and f illustrates 2D maps of calcium ion concentration (e) and pH profile (f) that were

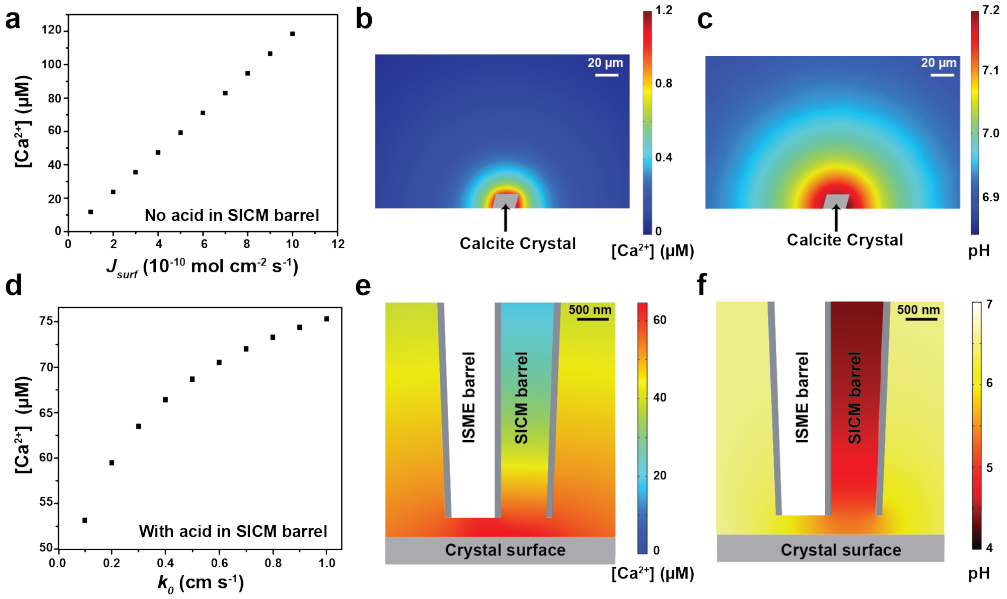

Figure 4.10: a) Plot of theoretical average interfacial calcium ion concentration at 300 nm away from the calcite microcrystal surface *vs.* J_{surf} calculated by the FEM simulation for a non-acid tip. Theoretical 2D maps of steady state b) calcium ion concentration and c) pH diffusion profiles around a calcite microcrystal dissolving in 100 mM KCl bulk solution at pH 6.8. d) Relationship between the average interfacial calcium concentration at 300 nm away from the calcite microcrystal surface and the k_0 calculated by the FEM simulation for an acid induced dissolution. Theoretical 2D maps of steady state e) calcium ion concentration and f) pH diffusion profiles around a calcite microcrystal and inside the SICM tip in the case of acid induced dissolution. Tip diameter: 1.5 μm.

generated near the calcite surface and inside the SICM barrel. The protons in the SICM barrel diffuse away to bulk solution, where a drop in proton concentration at the tip of the surface reaches 92% of the original 0.1 mM HCl. Subsequently, the pH at the end of the tip increases from 3.9 to 5.0, and reaches 5.1 at the microcrystal surface. The average calcium concentration at 300 nm away from the microcrystal surface, corresponding to the setpoint used herein, is plotted against dissolution rate constant k_0, (Figure 4.10d). The interfacial flux is given as follows:

$$J_{Ca^{2+}} = k_0[H^+] \tag{4.6}$$

This enabled the extraction of surface kinetics by comparing the experimental interfacial calcium concentration 66.0 ± 0.2 µM (pCa = 4.18) against the working curve. A rate constant of 0.4 ± 0.1 cm s^{-1} was extracted, which is in good agreement with literature values reported previously.[31]

Calcite microcrystals imaging

Dissolution of calcite microcrystals under acidic environment changes the topography of the microcrystal as well as the calcium concentration around the crystal and hence is an appropriate system for demonstrating the dual functionality of the ISME-SICM probes. This can reveal the capability of these probes in recording the topography using the SICM feedback mechanism, while simultaneously delivering the acid to induce the dissolution. As well as recording changes in ion concentration through the measurement of the ISME probe response. An ISME-SICM probe with solid-contact was used herein for imaging due to its higher stability compared to the liquid-contact ones. A hopping mode reported previously[16,32,33] was employed for mapping of an entire calcite microcrystal during dissolution. Briefly, the scanning probe was oscillated (200 nm peak-peak) to generate an alternating SICM current component i_{AC}, which then could be used as a set point for the feedback mechanism. The SICM-ISME probe approached the sample at 0.6 µm s^{-1} velocity, until the i_{AC} setpoint is reached, then the probe was retracted 10 µm in the z direction. Subsequently, the probe was moved 5 µm latterly, at a 4 µm s^{-1} scan rate, to start a new approach to the surface, until an image of 50 µm × 50 µm area is recorded. An optical micrograph of a typical calcite microcrystal in 100 mM KCl solution at pH 6.8 is shown in Figure 4.11a, and the corresponding topography map and calcium concentration profile are shown in Figure 4.11b and 4.11c, respectively. The topography generated using the SICM response matches the optical micrograph quite well, but with an advantage of providing height information as well as lateral dimensions. In this case, the calcite microcrystal average height was around 14 µm. The calcium

concentration map under acid induced dissolution conditions shows a significant increase in the calcium concentration from 10 µM at (10 µm away from the surface) up to 80 µM at the calcite microcrystal surface (300 nm working distance).

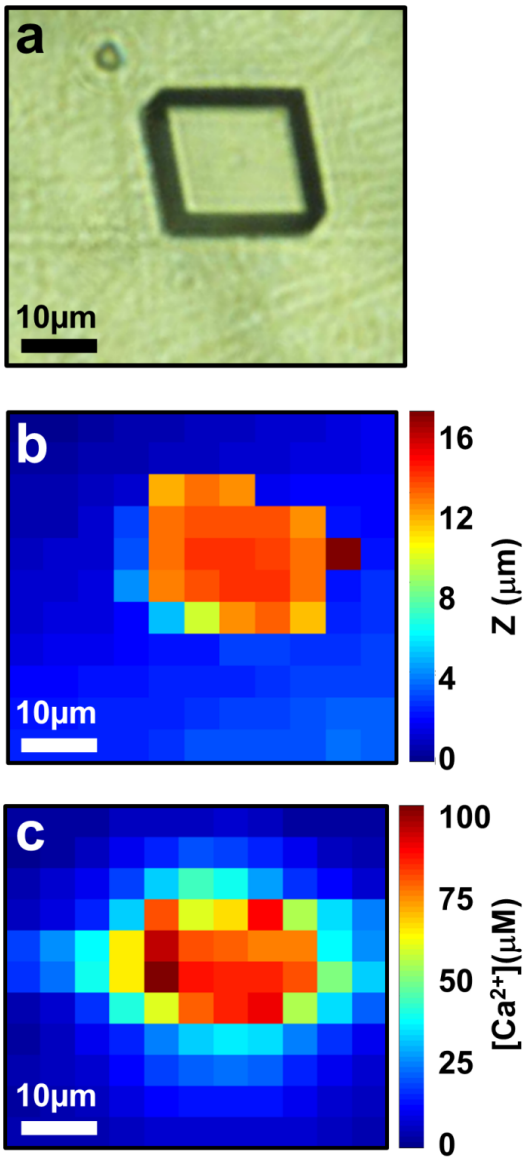

Figure 4.11: a) Optical micrograph, b) topographic and c) calcium concentration map of a calcite microcrystal with acid induced dissolution conditions. Distance modulation SICM feedback using hopping mode with 5 µm step. Tip diameter: 3 µm.

4.6 Conclusions

In this work, we have presented the fabrication and characterisation of a dual function ISME-SICM probe and its application for simultaneously tracking topography, delivering molecules/ions to the substrate surface and recording ions concentration. The capability of these probes was tested on the well-known calcite microcrystal dissolution problem under two distinct conditions, dissolution in neutral electrolyte solution, and an acid induced dissolution environments. The resulting values of the calcite dissolution flux extracted using finite element method simulations of the experiments, $2.82(\pm\ 0.02)\ \times\ 10^{-10}\ \mathrm{mol\,cm^{-2}\,s^{-1}}$ at pH 6.8 and the dissolution rate constant $0.4(\pm\ 0.1)\ \mathrm{cm\,s^{-1}}$ at pH 5.1 were in good agreement with values reported previously in the literature.[31] Although attempts to fabricate such probes have been reported previously, no data has been reported for its usage due to the complexity of probe fabrication and instrumentation.[16] The ISME solid-contact offered higher levels of stability compared to the conventional liquid-based contact, promoting the ability to use it for sample imaging over a long period of time. Thus, herein we present, for the first time, simultaneous mapping of topography and concentration distribution. The size of the probes reported in this work ranged between 1.5 and 3 µm (diameter), as no stable potentiometric response could be acquired for double barrel probes of size smaller than 1 µm in diameter. Another advantage of the probe is its ability to deliver reagents to the substrate using the SICM barrel, as well as the amenability of ISME barrel for detection of multitude of ions by changing the ionophore membrane. Thus the ISME-SICM probe could find applications in probing a wide range of samples such as cells *in vivo* and other materials like enamel and dentine.

4.7 References

(1) Bakker, E.; Bühlmann, P.; Pretsch, E. *Chem. Rev.* **1997**, 97, 3083-3132.

(2) Bühlmann, P.; Pretsch, E.; Bakker, E. *Chem. Rev.* **1998**, 98, 1593-1688.

(3) Numnuam, A.; Chumbimuni-Torres, K. Y.; Xiang, Y.; Bash, R.; Thavarungkul, P.; Kanatharana, P.; Pretsch, E.; Wang, J.; Bakker, E. *Anal. Chem.* **2008**, 80, 707-712.

(4) Eriksen, R. S.; Mackey, D. J.; van Dam, R.; Nowak, B. *Mar. Chem.* **2001**, 74, 99-113.

(5) Gupta, V. K.; Ganjali, M.; Norouzi, P.; Khani, H.; Nayak, A.; Agarwal, S. *Crit. Rev. Anal. Chem.* **2011**, 41, 282-313.

(6) Vanamo, U.; Bobacka, J. *Anal. Chem.* **2014**, 86, 10540-10545.

(7) Mensah, S. T.; Gonzalez, Y.; Calvo-Marzal, P.; Chumbimuni-Torres, K. Y. *Anal. Chem.* **2014**, 86, 7269-7273.

(8) Pretsch, E. *Anal. Chem.* **2002**, 74, 420A-426A.

(9) Thomas, R. C. *Ion-sensitive Intracellular Microelectrodes: How to Make and Use Them*; Academic Press Inc, 1978.

(10) Matzeu, G.; Zuliani, C.; Diamond, D. *Electrochim. Acta* **2015**, 159, 158-165.

(11) Vázquez, M.; Bobacka, J.; Ivaska, A.; Lewenstam, A. *Sens. Actuators, B* **2002**, 82, 7-13.

(12) Cadogan, A.; Gao, Z.; Lewenstam, A.; Ivaska, A.; Diamond, D. *Anal. Chem.* **1992**, 64, 2496-2501. (13) Bobacka, J.; McCarrick, M.; Lewenstam, A.; Ivaska, A. *Analyst* **1994**, 119, 1985-1991.

(14) Bobacka, J.; Lindfors, T.; McCarrick, M.; Ivaska, A.; Lewenstam, A. *Anal. Chem.* **1995**, 67, 3819-3823.

(15) Rubinova, N.; Chumbimuni-Torres, K.; Bakker, E. *Sens. Actuators, B* **2007**, 121, 135-141.

(16) Wei, C.; Bard, A. J.; Nagy, G.; Toth, K. *Anal. Chem.* **1995**, 67, 1346-1356.

(17) Yoon, Y.-H.; Shin, T.; Shin, E.-Y.; Kang, H.; Yoo, J.-S.; Park, S.-M. *Electrochim. Acta* **2007**, 52, 4614-4621.

(18) Edwards, M. A.; Williams, C. G.; Whitworth, A. L.; Unwin, P. R. *Anal. Chem.* **2009**, 81, 4482-4492.

(19) Hansma, P.; Drake, B.; Marti, O.; Gould, S.; Prater, C. *Science* **1989**, 243, 641-643.

(20) Shevchuk, A. I.; Gorelik, J.; Harding, S. E.; Lab, M. J.; Klenerman, D.; Korchev, Y. E. *Biophys. J.* **2001**, 81, 1759-1764.

(21) Takahashi, Y.; Shevchuk, A. I.; Novak, P.; Zhang, Y.; Ebejer, N.; Macpherson, J. V.; Unwin, P. R.; Pollard, A. J.; Roy, D.; Clifford, C. A. *Angew. Chem., Int. Ed.* **2011**, 50, 9638-9642.

(22) Izquierdo, J.; Kiss, A.; Santana, J. J.; Nagy, L.; Bitter, I.; Isaacs, H. S.; Nagy, G.; Souto, R. M. *J. Electrochem. Soc.* **2013**, 160, C451-C459.

(23) Archibald, D.; Qadri, S.; Gaber, B. *Langmuir* **1996**, 12, 538-546.

(24) Plummer, L. N.; Mackenzie, F. T. *Am. J. Sci.* **1974**, 274, 61-83.

(25) Haynes, W. M. *CRC Handbook of Chemistry and Physics, 93rd Edition*; Taylor & Francis, 2012.

(26) Cras, J.; Rowe-Taitt, C.; Nivens, D.; Ligler, F. *Biosens. Bioelectron.* **1999**, 14, 683-688.

(27) Munoz, J.-L.; Deyhimi, F.; Coles, J. *J. Neurosci. Methods* **1983**, 8, 231-247.

(28) Bühlmann, P.; Chen, L. D. *In Supramolecular Chemistry: From Molecules to Nanomaterials*; John Wiley & Sons, Ltd, 2012.

(29) Izquierdo, J.; Nagy, L.; Varga, Á.; Bitter, I.; Nagy, G.; Souto, R. M. *Electrochim. Acta* **2012**, 59, 398-403.

(30) Bakker, E.; Pretsch, E. *Anal. Chem.* **2002**, 74, 420 A-426 A.

(31) Arvidson, R. S.; Ertan, I. E.; Amonette, J. E.; Luttge, A. *Geochim. Cosmochim. Acta* **2003**, 67, 1623-1634.

(32) Nadappuram, B. P.; McKelvey, K.; Al Botros, R.; Colburn, A. W.; Unwin, P.

R. *Anal. Chem.* **2013**, 85, 8070-8074.

(33) Takahashi, Y.; Shevchuk, A. I.; Novak, P.; Murakami, Y.; Shiku, H.; Korchev, Y. E.; Matsue, T. *JACS* **2010**, 132, 10118-10126.

Chapter 5

Application of Finite Element Method FEM Simulation for the Characterisation of Dual Function Nanoscale pH-Scanning Ion Conductance Microscopy (SICM) Probes for High Resolution pH Mapping

Paulose Nadappuram B.; McKelvey K.; **Al Botros R.**; Colburn A. W.; and Unwin P. R.

Anal. Chem., 2013, 85(17), 8070 - 8074.

5.1 Abstract

The easy fabrication and use of nanoscale dual function pH-scanning ion conductance microscopy (SICM) probes is reported. These probes incorporate an iridium oxide coated carbon electrode for pH measurement and an SICM barrel for distance control, enabling simultaneous pH and topography mapping. These pH-SICM probes were fabricated rapidly from laser pulled theta quartz pipettes, with the pH electrode prepared by *in situ* carbon filling of one of the barrels by the pyrolytic decomposition of butane, followed by electrodeposition of a thin layer of hydrous iridium oxide. The other barrel was filled with an electrolyte solution and $Ag|AgCl$ electrode as part of a conductance cell for SICM. The fabricated probes, with pH and SICM sensing elements typically on the 100 nm scale, were characterised by scanning electron microscopy, energy-dispersive X-ray spectroscopy, and various electrochemical measurements. They showed a linear super-Nernstian pH response over a pH range of 2 to 10. The capability of the pH-SICM probe was demonstrated by detecting both pH and topographical changes during the dissolution of a calcite microcrystal in aqueous solution. This system illustrates the quantitative nature of pH-SICM imaging, because the dissolution process changes the crystal height (which provides dissolution rate information), as well as a change in interfacial pH (compared to bulk), which in turn when coupled with finite element method FEM modelling offer a vital method for calculating the dissolution rate. Both measurements reveal similar dissolution rates, which are in agreement with previously reported literature values measured by classical bulk methods.

5.2 Introduction

The measurement of local pH is hugely valuable in explaining complex interfacial reactions, such as corrosion,[1–2] metal deposition[3–4] and acid-base dissolution,[5–6] all

of which produce or consume protons and alter the pH near an interface. Additionally, many biological processes result in either intracellular[7−8] or extracellular[9] pH changes, and the quantitative measurement of these pH changes with high spatial resolution would aid in understanding the mechanisms involved.

While local pH can be visualised using optical techniques such as wide field fluorescence microscopy[9] and laser scanning confocal microscopy,[10] pH is commonly measured with electrodes. When deployed as the tip in scanning electrochemical microscopy (SECM), these electrodes have enabled the measurement of pH with high spatial resolution at interfaces.[11−14] The scale on which pH electrodes can be made has advanced in recent years to the micro[15−16] and nano scale.[17−18]

SECM pH probes employing a variety of metal/metal oxides have been reported previously.[15,19−21] Iridium oxide-based pH ultramicroelectrodes have proven particularly popular for spatially resolved pH measurements in SECM, owing to their fast response time, good stability over a wide range of pHs, temperatures and pressures, all-solid format and capability for miniaturisation.[22−23] Iridium oxide pH electrodes have been prepared by either electrochemical oxidation,[22] thermal decomposition[24] and sputter deposition[25] of iridium metal, or by the electrodeposition of iridium oxide from alkaline solutions of iridium salts.[23,26] Wipf *et al.* used a microscopic pH electrode produced by the deposition of iridium oxide onto carbon fibre microelectrode (7 µm diameter) to map pH changes near a platinum electrode during hydrogen evolution, and for monitoring the pH change associated with the oxidation of glucose by glucose oxidase immobilised onto a carbon microelectrode.[15]

Hitherto, pH probes used in SECM have typically been on the several microns scale or larger and, consequently, constant height (conventional) SECM scanning protocols have been used (*i.e.* without positional feedback). For high resolution pH mapping, nanoscale probes are mandatory, and these need to be placed close to the interface of interest.[27] This demands the use of positional feedback SECM, particularly for samples with large topographical features.

SICM has proven particularly powerful for topographical imaging of intricate surface geometries, including living cells.[27,28] SICM uses a nanopipette filled with an electrolyte, containing a quasi-reference counter electrode, QRCE (e.g. Ag/AgCl), as the scanning probe. A potential is applied between this electrode and an external QRCE, placed in the bulk solution, and the resulting ionic conductance current provides a (feedback) signal for distance control. Various SICM based positioning strategies have been developed over the years, to expand the range of substrates open to study. Moreover, the technique has been combined with complementary techniques including SECM[29–31] and near field scanning optical microscopy to enhance the information content.[32]

Herein, we present an extremely quick and simple method to fabricate a hybrid pH-SICM probe, with an iridium oxide-coated electrode for pH sensing and an SICM barrel for distance control. This report advances combined SECM-SICM[29] from amperometry/voltammetry to potentiometric imaging. pH-SICM probes were fabricated by the pyrolytic deposition of carbon into one of the barrels of a laser-pulled, sharp-point quartz theta pipette, followed by electrodeposition of hydrous iridium oxide to make it pH sensitive, with the open barrel forming part of the conductance cell for SICM measurement. The electrode size could be tuned by altering the pipette pulling parameters, but pH electrodes employed herein were typically on the 100 nm scale. The pH-SICM probes were employed for simultaneous mapping of pH and topography of a calcite microcrystal during dissolution to demonstrate their suitability for quantitative high spatial resolution measurements at surfaces and interfaces. This is an interesting system because the crystal size changes during dissolution which can be traced by the topographical response, while also determining the local interfacial pH. This provides two routes to determine the dissolution kinetics, which we show are consistent. Furthermore, measurements of an entire microcrystal is topographically demanding and hence for this study, we implemented pH-SICM in both a hopping mode,[30,33] and a constant separation mode,[31] to demon-

strate the versatility of the technique.

Finite element method FEM simulations were employed in this work to mimic the dissolution of a calcite microcrystal and track the interfacial proton diffusion profile in proximity of the crystal. Thus, extracting the dissolution rate value of calcite under the experimental conditions implemented herein.

5.3 Theory and Simulation

A three dimensional finite element method (FEM) model, relevant to the calcite microcrystal and dissolution conditions used in the study, was developed to estimate the surface pH and dissolution rate. This mass transport model prescribed the calcite microcrystal geometry in an aqueous solution under dissolution conditions (undersaturated solution). FEM modelling was performed using Comsol Multiphysics 4.3a (Comsol AB, Sweden) with transport of diluted species and chemical reaction engineering models implemented. All simulations were carried out using a PC equipped with an Intel core i7-3770, and 32 GB of RAM, and running 64 bit Windows 7. The basic geometry for the model is shown in Figure 5.1. Simulations were carried out with $>$ 1,000,000 tetrahedral mesh elements. The mesh resolution was defined to be finest near the surface of the crystal, which are boundaries 7-11. Simulations of varying mesh density were also performed (not reported) to ensure a fine enough mesh was used for the model.

The dissolution of calcite is strongly pH dependent and this process increases the local pH, at the calcite water interface. Plummer *et al*[34] proposed that the following three reactions occur simultaneously on the calcite surface.[35,36] Under the conditions of our experiment (pH $\sim$ 7), the dissolution process described by eq 5.3 dominates.

$$CaCO_{3(s)} + H^{+} \rightleftharpoons Ca^{2+}_{(aq)} + HCO^{-}_{3(aq)} \tag{5.1}$$

$$CaCO_{3(s)} + H_2CO_{3(aq)} \rightleftharpoons Ca^{2+}_{(aq)} + 2HCO^{-}_{3(aq)} \tag{5.2}$$

$$CaCO_{3(s)} + H_2O_{(l)} \rightleftharpoons Ca^{2+}_{(aq)} + HCO^{-}_{3(aq)} + OH^{-}_{(aq)} \tag{5.3}$$

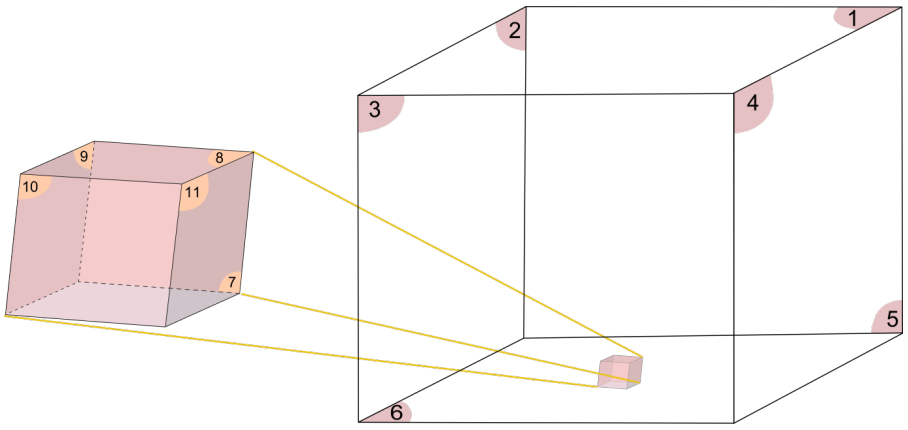

Figure 5.1: A schematic of the FEM model showing the calcite crystal (left).The crystal dimensions are length of the crystal l, width of the crystal w, height of the crystal h. The bulk solution consists of a cube with a dimension of $30l$. The boundaries are numbered according to the constraints listed in text.

The calcium carbonate aqueous solutions, which are open to the atmosphere, in the presence of a calcite crystal can be described by the equilibria in Table 5.1.[37] A mass transport model was designed to mimic the calcite microcrystal geometry in an aqueous solution, implementing these equilibria.

As all the experiments of calcite imaging with the pH-SICM probe were carried out after equilibrating the sample for 30 mins, mass transport was considered to be predominantly governed by diffusion, for which Fick's first law equation was solved under steady state conditions:

$$D_j \bigtriangledown c_j + R_j = 0 \tag{5.4}$$

where D_j is the diffusion coefficient and c_j is the concentration of species j,

Table 5.1: Equilibria data for the calcite-H_2O system open to the atmosphere.[37]

Eq	**Reaction**	$\mathbf{p}K_{eq}/\mathbf{p}K_a$
R5.1	$CO_2 + H_2O_{(l)} \rightleftharpoons H_2CO_{3(aq)}$	1.466
R5.2	$H_2CO_{3(aq)} \rightleftharpoons H^+_{(aq)} + HCO^-_{3(aq)}$	6.351
R5.3	$HCO^-_{3(aq)} \rightleftharpoons H^+_{(aq)} + CO^{2-}_{3(aq)}$	10.330
R5.4	$CaHCO^+_{3(aq)} \rightleftharpoons Ca^{2+}_{(aq)} + HCO^-_{3(aq)}$	1.015
R5.5	$CaCO_{3(aq)} \rightleftharpoons Ca^{2+}_{(aq)} + CO^{2-}_{3(aq)}$	3.2
R5.6	$H_2O_{(l)} \rightleftharpoons H^+_{(aq)} + OH^-_{(aq)}$	13.997

R_j is a kinetic term representing the loss or formation of species j defined by the equilibration reactions, as described by activity corrected mass action rate equations.[38] The equilibrium constant values used herein are illustrated in Table 5.1 (before activity correction). The diffusion coefficients of the individual species can be considered to be constant over the spatial domain investigated; these values are presented in Table 5.2.

Table 5.2: Diffusion coefficient values of various species used in the FEM model.[39]

Species	Ca^{2+}	H^+	OH^-	K^+
Diffusion coefficient (10^{-9} m^2 s^{-1})	0.792	7.80	5.273	1.957
Species	Cl^-	H_2CO_3	HCO_3^-	CO_3^{2-}
Diffusion coefficient (10^{-9} m^2 s^{-1})	1.185	0.932	2.032	1.185

The equilibrium concentrations in bulk solution were calculated using CO_2

partial pressure P_{CO_2} = 0.039% atm,[35] and the solution pH = 6.85, which was measured experimentally. The boundary conditions applied to the model, as illustrated in Figure 5.1, are listed in Table 5.3. Boundaries 1-5 are at a considerable distance away from the crystal (30× the largest dimension of the crystal), so they can reasonably be considered as bulk solution. Thus, they are constrained by a bulk concentration condition. Boundary 6 is constrained by a no-flux condition, to represent the unreactive surface of the glass substrate. Boundaries labelled 7- 11 represent the dissolving crystal faces on which a flux of produced hydroxyl, calcium and bicarbonate ions were imposed; to satisfy the dissolution equation 5.3 on these boundaries. A plot of average surface pH obtained from FEM simulations using a range of J_{surf} values (Figure 5.2), was used to calculate the dissolution rate associated with the average surface pH recorded experimentally on the calcite microcrystal during dissolution.

Table 5.3: Summarised boundary conditions for the FEM model.

Boundary	**condition**
B1-B5	$c_i = c_{0,i}$
B6	$J_i = 0$
B7-B11	$\mathbf{n}(D_{Ca^{2+}} \bigtriangledown c_{Ca^{2+}}) = J_{surf}$ $\mathbf{n}(D_{HCO_3^-} \bigtriangledown c_{HCO_3^-}) = J_{surf}$ $\mathbf{n}(D_{OH^-} \bigtriangledown c_{OH^-}) = J_{surf}$

5.4 Results and Discussion

5.4.1 pH Mapping of Calcite Dissolution

The dissolution of calcite is strongly pH-dependent and this process increases the local pH at the calcite-water interface.[34,35,40] The pH-SICM probe was used to map

the interfacial pH and changes in crystal size that occurred during calcite microcrystal dissolution. This served to illustrate the dual capability of these probes: topography mapping combined with simultaneous local pH measurements.

For mapping of an entire calcite microcrystal during dissolution, we implemented a hopping mode similar to that reported previously for SICM.[30,32] Thus, a series of approach curves that stopped upon reaching a specific AC-set point, signifying a particular (close) distance from the surface was used to create an image. Briefly, the probe was approached to the calcite microcrystal at a speed of 0.2 µm s^{-1} while the ac component of ionic current, i_{AC}, was monitored during the approach. The pH was recorded simultaneously as a function of z-position (normal to the substrate). As soon as the value of i_{AC} exceeded the set point, the probe was quickly withdrawn to 25 µm, moved to a new x-y pixel (in the plane of the substrate) to start a new measurement cycle.

An optical micrograph of a typical calcite microcrystal, in 0.01 M KCl, obtained directly on the experimental set up, is shown in Figure 5.2A and the corresponding 3-D topography map recorded by the pH-SICM probe is shown in Figure 5.2B. This SICM image is seen to match very with the optical image, with the advantage that the SICM image provides information of the crystal height as well as the lateral dimensions. The pH map corresponding to the distance of closest approach from the surface (estimated as 100 nm, from the magnitude of i_{AC}[41]) is shown in Figure 5.2C. As expected under dissolution conditions, a dramatic increase in pH was observed near to the microcrystal, with the pH taking values of *ca.* 7.9 ± 0.1 close to the microcrystal surface compared to a bulk value of *ca.* 6.85 in this particular case.

A three-dimensional FEM model, describing calcite microcrystal dissolution, was used to predict the pH on the crystal surface for different dissolution fluxes (see Figure 5.3). The pH image over the calcite microcrystal and surrounding surface shown in Figure 5.2D corresponds to dissolution with an interfacial flux of 1.6 ×

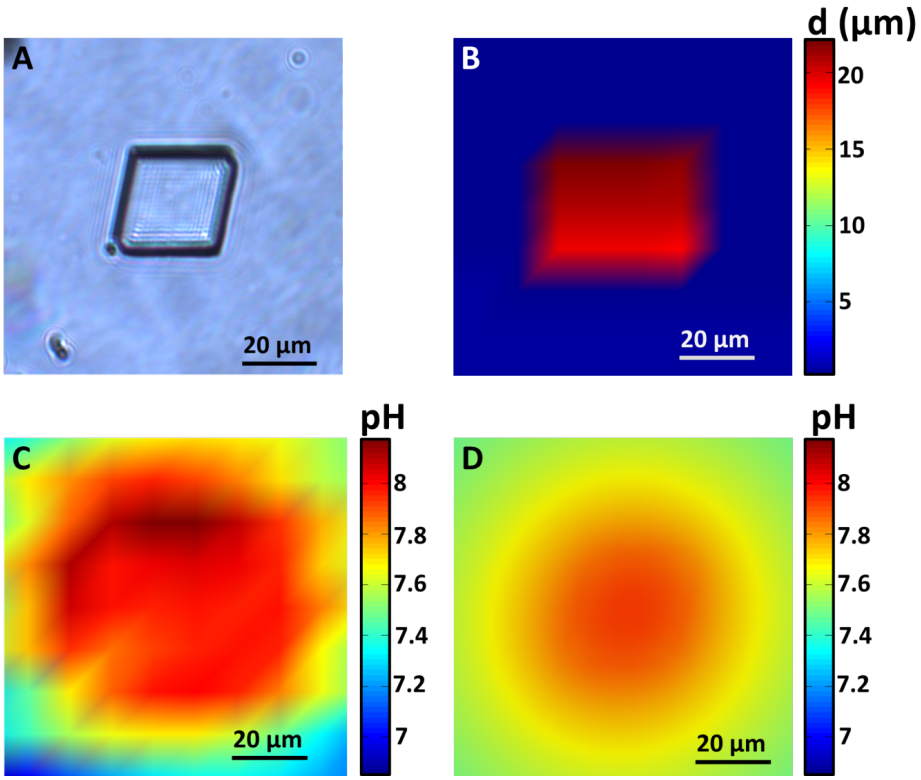

Figure 5.2: Topography and pH mapping of a calcite microcrystal. (A) Optical micrograph of the calcite microcrystal. (B) SICM topography image of calcite microcrystal. (C) pH map close to (100 nm from) the calcite microcrystal and glass surface recorded simultaneously with topography (bulk pH 6.85). (D) FEM model of the pH distribution close to (100 nm from) the calcite microcrystal and supporting glass substrate for a dissolution flux of 1.6 $\times$ 10^{-9} mol cm^{-2} s^{-1}.

10^{-9} mol cm^{-2} s^{-1} at the calcite/solution interface; yielding a pH 7.94, in good agreement with the surface pH recorded during the scan.

High resolution images in constant distance mode were recorded as a series of line scans over a scan area of 20 µm by 20 µm with a line scan every 1 µm. The scan rate employed was 1 µm s^{-1} and the tip/crystal distance for the probe size used, was *ca.* 100 nm, corresponding to the set-point employed.[41] Surface features resembling the edge of a calcite hillock[42,43] are observed in the topographical map demonstrating the feasibility of high resolution topography imaging, using these pH-SICM probes. To quantify the dissolution rate, two successive scans were performed on the calcite

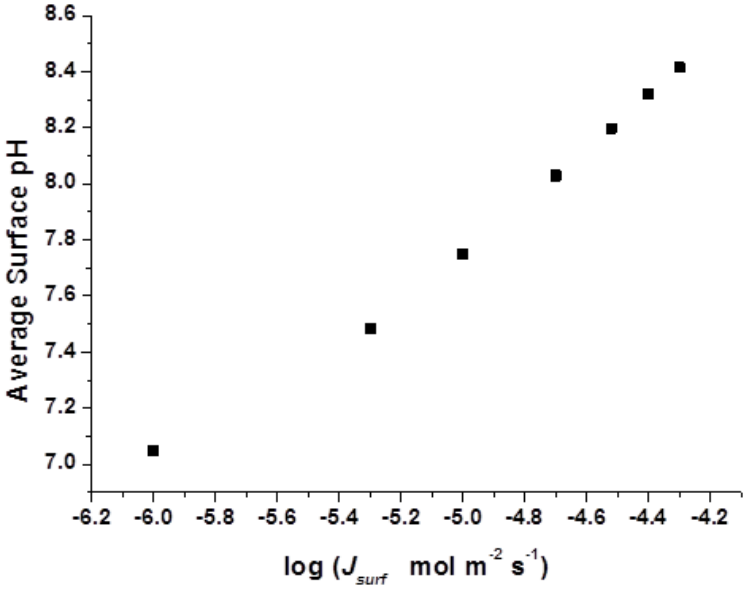

Figure 5.3: Relationship between the average interfacial pH (100 nm from the calcite microcrystal surface) and log(J_{surf}) calculated by the FEM simulation.

microcrystal surface and the change in crystal height between each (Figure 5.4 (panels A and B)) was determined. The two scans were performed in the same area with each of the lines in the second scan carried out 1200 s after those in the first scan. Between the two consecutive scans, an average height difference of 1.1 ± 0.1 µm was observed (for the scanning conditions employed, the effect of thermal drift on topography measurement[43] was < 0.1 µm, determined by repetitively imaging a glass surface) for an area of 400 µm^2 of the crystal surface, suggesting a dissolution rate of 2.6 (±0.2) × 10^{-9} mol cm^{-2} s^{-1} at pH 6.85.

Figure 5.4 (panels C and D) shows the respective, simultaneous pH map recorded on the surface of the calcite microcrystal. As expected, the average surface pH on the calcite microcrystal surface was higher than in the bulk electrolyte, and found to be 8.05 ± 0.06. This yields a dissolution flux of 1.9 (± 0.2) × 10^{-9} mol cm^{-2} s^{-1} (see Figure 5.3 for the working curve of pH to flux), which is in good

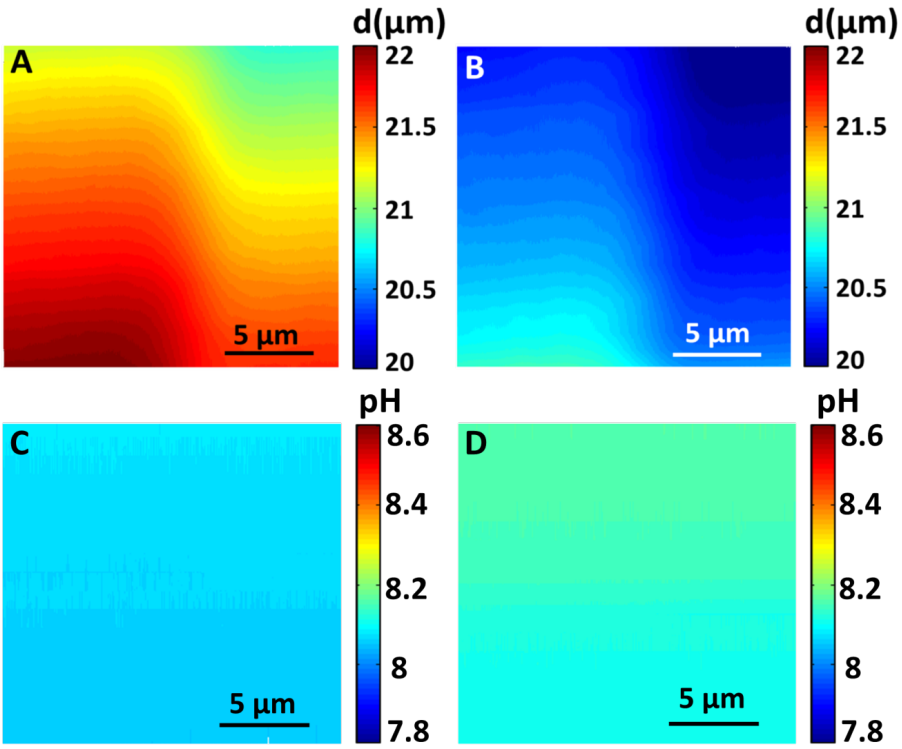

Figure 5.4: Simultaneous topography (A and B) and pH (C and D) images of calcite crystal surface recorded during two constant height electrochemical scans (bulk pH 6.85). Images (B) and (D) were recorded 20 minutes after (A) and (C).

agreement with the value found above from the direct measurement of the crystal plane. Moreover, these values are in good agreement with those expected and on earlier bulk measurements.[44,45]

5.5 Conclusions

A fast and inexpensive method to fabricate nanoscale iridium oxide-based pH-SICM probes has been presented. These probes incorporate SICM-based distance feedback control and are suitable for simultaneous topography and pH imaging. The capability of these probes for generating spatially-resolved pH maps of surfaces and interfaces has been demonstrated through studies of topographically challenging calcite microcrystals and analysing data through coupling with FEM modelling. Both the

pH distribution and height change yields rates which are consistent with expected values based on known dissolution kinetics, highlighting the promise of these probes for high resolution quantitative pH mapping in the future, and the capability of validating probes measurements and response time through numerical simulation.

5.6 References

(1) Zhao, M. C.; Liu, M.; Song, G. L.; Atrens, A. *Corros. Sci.* **2008**, 50, 3168 - 3178.

(2) Tanabe, H.; Togashi, K.; Misawa, T.; Mudali, U. K. *J. Mater. Sci. Lett.* **1998**, 17, 551 - 553.

(3) Zhang, J. M.; Lin, C. J.; Feng, Z. D.; Tian, Z. W. *J. Electroanal. Chem.* **1998**, 452, 235 - 240.

(4) Natter, H.; Hempelmann, R. *J. Phys. Chem.* **1996**, 100, 19525 - 19532.

(5) Compton, R. G.; Unwin, P. R. *Philos. T. Roy. Soc. A*. **1990**, 330, 1 - 45.

(6) Orton, R.; Unwin, P. R. *J. Chem. Soc. Faraday. T.* **1993**, 89, 3947 - 3954.

(7) Shen, S. S.; Steinhardt, R. A. *Nature* **1978**, 272, 253 - 254.

(8) Hess, S. T.; Huang, S.; Heikal, A. A.; Webb, W. W. *Biochem.* **2002**, 41(3), 697 - 705.

(9) Miesenböck, G.; De Angelis, D. A.; Rothman, J. E. *Nature* **1998**, 394, 192 - 195.

(10) Rudd, N. C.; Cannan, S.; Bitziou, E.; Ciani, L.; Whitworth, A. L.; Unwin, P.R. *Anal. Chem.* **2005**, 77, 6205 - 6217.

(11) Bard, A. J.; Fan, F. R. F.; Kwak, J.; Lev, O. *Anal. Chem.* **1989**, 61, 132 - 138.

(12) Bard, A. J.; Mirkin, M. V. *Scanning Electrochemical Microscopy*, 2nd edn., CRC Press, Boca Raton, Fla., 2012.

(13) Kueng, A.; Kranz, C .; Lugstein, A.; Bertagnolli, E.; Mizaikoff, B. *Angew. Chem. Int. Edit.* **2005**, 44, 3419 - 3422.

(14) Horrocks, B. R.; Mirkin, M. V.; Pierce, D. T.; Bard, A. J.; Nagy, G.; Toth, K. *Anal. Chem.* **1993**, 65, 1213 - 1224.

(15) Wipf, D. O.; Ge, F. Y.; Spaine, T. W.; Bauer, J. E. *Anal. Chem.* **2000**, 72, 4921 - 4927.

(16) Bezbaruah, A. N.; Zhang, T. C. *Anal. Chem.* **2002**, 74, 4428 - 4432.

(17) Zhang, X.; Ogorevca, B.; Wang, *J. Anal. Chim. Acta.* **2002**, 31, 1 - 10.

(18) Yamamoto, K.; Shi, G. Y.; Zhou, T. S.; Xu, F.; Zhu, M.; Liu, M.; Kato,T.; Jin, J. Y.; Jin, J. Y. *Anal. Chim. Acta.* **2003**, 480, 109 - 117.

(19) Hitchman, M. L.; Ramanathan, S. *Analyst* **1988**, 113, 35 - 39.

(20) Kreider, K. G.; Tarlov, M. J.; Cline, J. P. *Sensor. Actuat. B-Chem.* **1995**, 28, 167 - 172.

(21) Marzouk, S. A. M.; Ufer, S.; Buck, R. P.; Johnson, T. A.; Dunlap, L. A.; Cascio, W. E. *Anal. Chem.* **1998**, 70, 5054 - 5061.

(22) Wang, M.; Yao, S.; Madou, M. *Sensor. Actuat. B-Chem.* **2002**, 81, 313 - 315.

(23) Elsen, H. A.; Monson, C. F.; Majda, M. *J. Electrochem. Soc.* **2009**, 156, F1 - F6.

(24) Lodi, G.; Debattisti, A.; Bordin, G.; Deasmundis, C.; Benedetti, A. *J. Electroanal. Chem.* **1990**, 277, 139 - 150.

(25) Katsube, T.; Lauks, I.; Zemel, J. N. *Sensor. Actuator.* **1982**, 2, 399 - 410.

(26) Bitziou, E.; O'Hare, D.; Patel, B. A. *Anal. Chem.* **2008**, 80, 8733 - 8740.

(27) Hansma,P. K.;.; Drake, B.; Marti, O.; Gould, S. A.; Shiku, H.; Prater, C. B. *Science* **1989**, 243, 641 - 643.

(28) Novak, P.; Li, C.; Shevchuk, A. I.; Stepanyn, R., Caldwell, M.; Hughes, S.; Smart, T. G.; Gorelik, J.; Ostanin, V. P.; Lab, M. J.; Moss, G. W. J.; Frolenkov, G. I.; Klenerman, D.; Korchev, Y. E. *Nat. Methods* **2009**, 6, 279 - 281.

(29) Takahashi, Y.; Shevchuk, A. I.; Novak, P.; Zhang, Y.; Ebejer, N.; Macpherson, J. V.; Unwin, P. R; Pollard, A. J.; Roy, D.; Clifford, C. A.; Shiku, H.; Matsue, T.; Klenerman, D.; Korchev, Y. E. *Angew. Chem. Int. Edit.* **2011**, 50, 9638 - 9642.

(30) Takahashi,Y.; Shevchuk, A. I.; Novak, P.; Murakami, Y.; Shiku, H.; Korchev, Y. E.; Matsue, T. *J. Am. Chem. Soc.* **2010**, 132, 10118 - 10126.

(31) Comstock, D. J.; Elam, J. W.; Pellin, M. J.; Hersam, M. C. *Anal. Chem.* **2010**, 84, 1270 - 1276.

(32) Korchev, Y. E.; Raval, M.; Lab, M. J.; Gorelik, J.; Edwards, C. R. W.; Rayment, T.; Klenerman, D. *Biophys. J.* **2000**, 78, 2675 - 2679.

(33) Lazenby, R. A.; McKelvey, K.; Unwin, P. R. *Anal. Chem.* **2013**, 85, 2937 - 2944.

(34) Plummer, L. N.; Mackenzie, F. T. *Am. J. Sci.* **1974**, 274, 61-83.

(35) Stumm, W.; Morgan, J. *Aquatic chemistry: Chemical equilibria and rates in natural waters* 3edn., John Wiley & Sons, New York, 1995.

(36) Arvidson, R. S.; Ertan, I. E.; Amonette, J. E.; Luttge, A. *Geochim. Cosmochim. Ac.* **2003**, 67, 1623-1634.

(37) Haynes, W. M.; Lide, D. R.; Bruno T .J. *CRC Handbook of Chemistry and Physics 2009-2010.*CRC Press, Boca Raton, Fla., 2012.

(38) Grime, J. M. A.; Edwards, M. A.; Rudd, N. C.; Unwin, P. R. *P. Natl. Acad. Sci. USA*. **2008**, 105, 14277-14282.

(39) McGeouch, C.-A.; Peruffo, M.; Edwards, M. A.; Bindley, L. A.; Lazenby, R. A.; Mbogoro, M. M.; McKelvey, K.; Unwin, P. R. *J. Phys. Chem. C.* **2012**, 116, 14892-14899.

(40) Cravotta, C. A.; Trahan, M. K. *Appl. Geochem.* **1999**, 14, 581 - 606.

(41) Edwards, M. A.; Williams, C. G.; Whitworth, A. L.; Unwin, P. R. *Anal. Chem.* **2009**, 81, 4482 - 4492.

(42) Kim, I. W.; Giocondi, J. L.; Orme, C.; Collino, S.; Evans, *J. Cryst. Growth. Des.* **2008**, 8, 1154 - 1160.

(43) Dobson, P. S.; Bindley, L. A.; Macpherson, J. V.; Unwin, P. R. *Langmuir* **2012**, 21, 1255 - 1260.

(44) Rickard. D.; Sjoberg, E. L. *Am. J. Sci.* **1983**, 283, 815 - 830.

(45) Plummer, L. N.; Busenberg, E. *Geochim. Cosmochim. Ac.* **1982**, 46,1011 - 1040.

Chapter 6

Finite Element Method FEM Simulation for the Combinatorial Localised Dissolution Analysis: Application to Acid-induced Dissolution of Dental Enamel and the Effect of Surface Treatments

Parker A. S.; **Al Botros R.;** Kinnear S. L.; Snowden M. E.; McKelvey K.; Ashcroft A. T.; Carvell M.; Joiner A.; Peruffo M.; Philpotts C.; and Unwin P. R.

in preparation

6.1 Abstract

A combination of scanning electrochemical cell microscopy (SECCM) and AFM have been used to quantitatively study the acid-induced dissolution of enamel. A micron-scale liquid meniscus formed at the end of a dual barrelled pipette, which constitutes the SECCM probe, is brought into contact with the enamel surface for a defined period. Dissolution occurs at the interface of the meniscus and the enamel surface, under conditions of well-defined mass transport, creating etch pits that are then analysed via AFM. This technique is applied to bovine enamel, and the effect of various treatments of the enamel surface on acid dissolution (1 mM HNO_3) is studied. The treatments investigated are zinc ions, fluoride ions and the two combined. A finite element method (FEM) simulation, combined with the AFM data, allows the intrinsic rate constant for acid-induced dissolution to be quantitatively determined due to the well-defined mass transport within the SECCM probe. The dissolution of enamel, in terms of Ca^{2+} flux ($J_{Ca^{2+}}$), is first order with respect to the interfacial proton concentration and given by the following rate law; $J_{Ca^{2+}} = k_0[H^+]$, with $k_0 = 0.099 \pm 0.008$ cm s^{-1}. Treating the enamel with either fluoride or zinc slowed the dissolution rate, although the protective barrier only extends 20 nm into the enamel surface which meant that dissolution of modified surfaces tended towards that of native enamel after a short period of a few seconds. A combination of both treatments exhibited the greatest protection to the enamel surface, but the effect was again transient.

6.2 Introduction

The dissolution of solid materials is an area of significant interest[1] across many fields, including the earth sciences,[2,3] corrosion science,[4] and the life sciences,[5] as well as chemistry.[6–12] Studies of the mechanism and kinetics of dissolution processes are

important for both further understanding and developing technical applications. This requires methodologies that can probe dissolution under conditions of high and well-defined mass transport,[13] so that surface kinetics can be extracted free from convolution from mass transport limitations.[13,14] This means that dissolution experiments must deliver sufficiently high and well-defined mass transport rates such that surface kinetics are manifest in the measurement.

This chapter introduces a powerful combinatorial approach for dissolution studies, in which a large number of micron scale measurements are made rapidly on a small area of a single sample surface, for which different portions have been treated in different ways. The focus is on the acid-induced dissolution of dental enamel as an exemplar system, and which is also of significant interest. Enamel is the hardest mineral found in the human body,[15] forming the outer protective layer of teeth. Its main component is calcium hydroxyapatite (HAP, $Ca_{10}(PO_4)_6(OH)_2$) which makes up more than 95% of enamel by weight,[16] with the remainder comprised of a matrix of organic molecules, macromolecules and water.[17] Dental enamel is constructed from rods also known as prisms, each containing a tightly packed mass of HAP nanocrystallites in a highly orientated and organised structure.[18] Once formed, enamel has no vascular or nerve system, and can only regenerate through remineralisation processes in the oral cavity.[19] Conversely, the enamel layer can be affected adversely through acid-induced dissolution processes associated with dental caries or erosion from the modern diet.[20–22]

Acid attack of HAP is reasonably described by the following reaction:[23]

$$Ca_{10}(PO_4)_6(OH)_2)_{(S)} + 8H^+_{(aq)} \rightleftharpoons 10Ca^{2+}_{(aq)} + 6HPO^{2-}_{4(aq)} + 2H_2O_{(l)} \qquad (6.1)$$

This is the primary process of tooth demineralisation: protons react with HAP which releases Ca^{2+} and HPO_4^{2-} ions into the solution,[15,24,25] coupled with further solution processes (*vide infra*).

As highlighted above, to understand the relative contribution of surface processes and mass transport to demineralisation rates, experiments need to be carried out under controlled, calculable, and sufficiently high mass transport conditions.[13,14,23,26] The main approach with well-defined mass transport that has been used in studies of enamel and HAP dissolution is the rotating disk (RD) method.[27–32] However, while the RD method delivers well-defined mass transport rates,[33] analysis is often restricted to bulk solution measurements which places severe limitations on the time and spatial resolution of the technique.[13] This is particularly critical for the investigation of surface treatments that have a transient effect, which require methods with high time resolution in order to elucidate effects that the surface treatments have on enamel. In terms of spatial resolution, a number of studies have used high resolution microscopy to attempt to study enamel dissolution at the nanoscale[20,34–41] However, with the exception of scanning electrochemical microscopy (SECM),[40] the approaches often have rather low mass transport rates and all require the sample to be exposed to solution for long periods, making it difficult to monitor transient effects on dissolution, such as the effect of surface treatments.

Several treatments have successfully been used to protect enamel from acid dissolution.[42,43] It is well documented that treatment of enamel with fluoride results in a surface layer of fluoridated hydroxyapatite and fluorapatite[44–47] which resists acid attack better than natural enamel,[48,49] thus inhibiting demineralisation.[48,50] The effect of Zn^{2+} treatment on enamel decreases the loss of Ca^{2+} and PO_4^{3-} ions from the surface. Different mechanisms have recently been studied, where the binding of Zn^{2+} leading to the precipitation of an apatite-like phase, and the formation of a zinc complex at the surface of enamel has been suggested.[47,51–54]

The work presented here employs a new approach for the study of dissolution processes, coupling localised measurements with high and controlled mass transport through the use of SECCM.[55–59] The aim is to demonstrate the methodology and to gain a better understanding of the acid induced dissolution process on enamel

surfaces as well as the effect of treating the enamel surface with zinc and fluoride. Localised dissolution is achieved by confining the experiment to the meniscus of a pipette with a diameter *ca.*1 µm. This setup allows the rest of the surface to be kept in air giving each local dissolution event a high time resolution. Due to the high migration of ions across the meniscus, to the surface, and within the probe geometry fast surface kinetics can be investigated.[56] SECCM is used as a tool to allow very fine control of the delivery of acid to the enamel surfaces resulting in localised etch pits. These dissolution etch pits are then analysed using AFM and, using a finite element method (FEM) simulation, the intrinsic rate for proton induced dissolution (Ca^{2+} release) is extracted. We have presented preliminary data using this method as part of a multi technique approach to elucidate a new treatment for enamel erosion.[60] Here, we apply the technique in much more detail to common treatments of dental enamel, highlighting the spatial resolution of the techniques and developing a full theoretical model to perform the quantitative analysis of data.

6.3 Experimental details

6.3.1 Solutions

All solutions were prepared using 18.2 MΩ cm (25°C) water (Purite). Etching solutions (50 mM KNO_3 and 1 mM HNO_3 (Sigma-Aldrich)) were prepared daily (pH 3.3, Denver Instruments UB-10 pH meter). Zinc salt solutions used for enamel pretreatment were made using 1000 ppm of Zn^{2+} from $ZnCl_2$ (Sigma-Aldrich). Fluoride solutions for enamel pretreatment were 1000 ppm of F^- using NaF (Sigma-Aldrich).

6.3.2 Sample preparation

Bovine enamel samples were received from Unilever as 36 mm^2 area blocks polished to a 3 µm root mean squared (RMS) roughness, as measured by AFM (Bruker).

The samples were then further polished using diamond lapping particles on a silk polishing pad, starting with 3 µm sized particles and slowly working down to 50 nm (Buehler). The polishing was carried out until a mirror finish was achieved with an RMS of 1.5 ± 0.6 nm measured by AFM. Three different treatments were applied to each enamel block, one treatment per section, with rinsing of the sample in Purite water between treatments. To selectively treat a particular section, a low tack polyester tape (3M) was used to protect all but the area of interest, before submerging the sample in the treatment solution for 2 minutes (see Figure 6.1). The treatments used were 1000 ppm F^-, 1000 ppm Zn^{2+}, and a sector of the enamel was also subjected to a combined treatment with F^- and Zn^{2+}, applied sequentially as depicted in Figure 6.1.

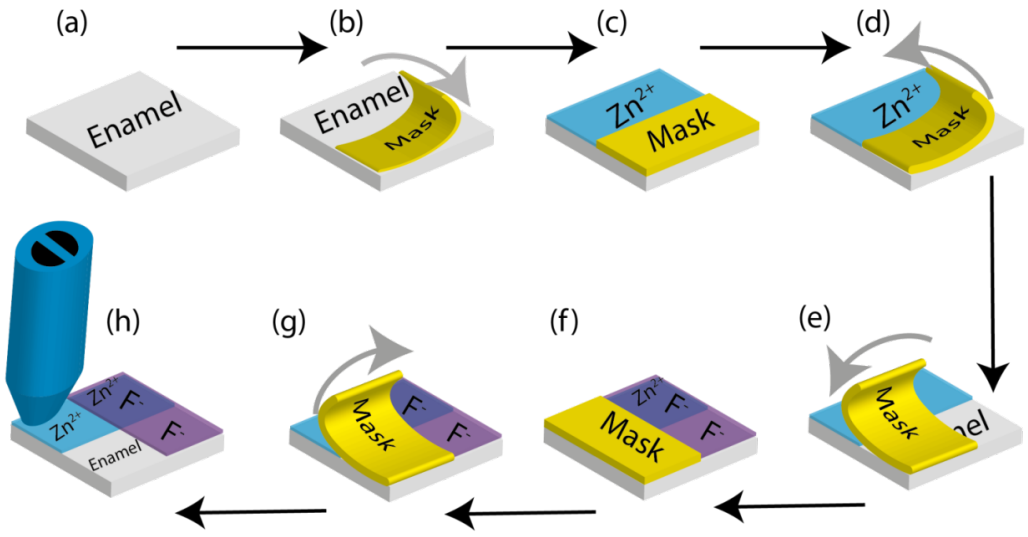

Figure 6.1: Representation of the localised treatments applied to an enamel block: a) Enamel block polished before any treatment applied; b) Half the sample masked off with polyester tape; c) Zn^{2+} treatment applied to sample; d) Polyester mask removed; e) Mask reapplied at 90° rotation; f) Zn^{2+} treatment applied to sample; g) Mask removed; h) process could be repeated to increase treatment numbers and SECCM experiments carried out.

6.3.3 SECCM method

The SECCM tips used were fabricated from 1.5 mm diameter borosilicate theta barrel capillaries (Harvard Apparatus) that were pulled to a sharp point using a P-2000 laser puller (Sutter Instruments Co.). The tip of the pipette was oval and approximately 800 nm across the main axis after being pulled. A representative tip is pictured in Figure 6.2(a). Each pipette was filled with the etching solution and a quasi-reference counter electrode (QRCE) comprising an AgCl-coated Ag wire was inserted into each barrel.

The SECCM technique was set up as recently described.[59] The pipette was positioned close to the enamel surface using a manual micrometer system (M-461 series, Newport) aided by a digital camera (Pixelink). Fine positioning of the pipette was achieved using a piezoelectric positioner system with a range of 38 µm normal to the substrate, in the z-axis (P-753.3CD positioner, Physik Instrumente) and 300 µm parallel to the substrate in the x- and y-axes (Nano-Bio300, Mad City Labs). A potential of 0.25 V was applied between the QRCEs in the barrels of the theta pipette using a home-built instrument controlled via LabVIEW 2011 and a field programmable gate array card (PCI-783R, National Instruments). An oscillation of 80 nm amplitude was applied to the z-position of the tip, with a frequency of 233.5 Hz, using an external lock-in amplifier (SR830DSP, Stanford Research Systems), and the resulting alternating current (AC) magnitude at the driving frequency was measured and used to inform on the meniscus condition. An approach-hold-withdraw method, as illustrated in Figure 6.2(b), was used to carry out local dissolution at the enamel surface with different solution contact times. First, as shown in Figure 6.2(b)(i), the z-piezo was used to move the pipette towards the surface and the approach was stopped when the meniscus made contact with the surface (without the pipette itself making contact) as evidenced by a sudden change in the AC value. Typically, a threshold value of one order of magnitude higher than the background

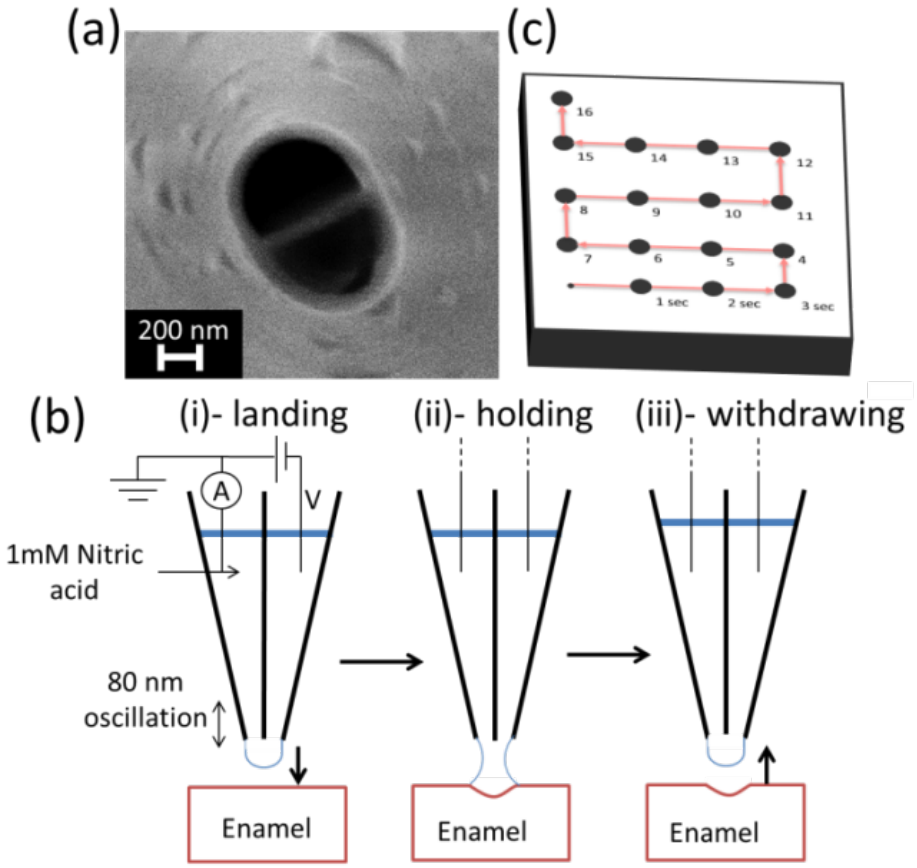

Figure 6.2: (a) SEM image of pipette tip. (b) Representation of the experimental setup used. The approach-hold-withdraw cycle and probe path used in SECCM experiments. (i) Probe approaches enamel surface. (ii) Meniscus makes contact with surface and is held for a set time. (ii) The probe is withdrawn and meniscus removed from the surface. (c) The path the probe takes during the whole array used. Red line represents tip path. Each spot is held in contact 1 second longer than the previous spot.

AC measured when the tip was in air. This change in current is due to the meniscus spreading out onto the surface.[61] The meniscus was held in contact with the surface for a precise period of time (Figure 6.2(b)(ii)), after which it was rapidly translated away from the surface (20 µm s^{-1}), breaking meniscus contact (Figure 6.2(b)(iii)). The pipette was then moved laterally to the next approach location at a velocity of 1 µm s^{-1} (taking 5 seconds), in this time the solution in the meniscus retuned to its initial conditions (equilibrium reached in << 1 sec).[59] This procedure was

used to prepare an array of local etch features, following the pattern described in Figure 6.2(c), which also shows the path of the pipette. The array created in this experiment started with a 1 s meniscus hold time on the surface, and this was increased by 1 s for each subsequent position, up to a total of 16 s. Six arrays were created in each treatment section of an enamel surface and a total of four bovine enamel samples were studied, meaning that 24 separate arrays were created for the four different surfaces. Optical images showing an experiment in progress and an example of the resultant pit arrays are provided in Figure 6.3.

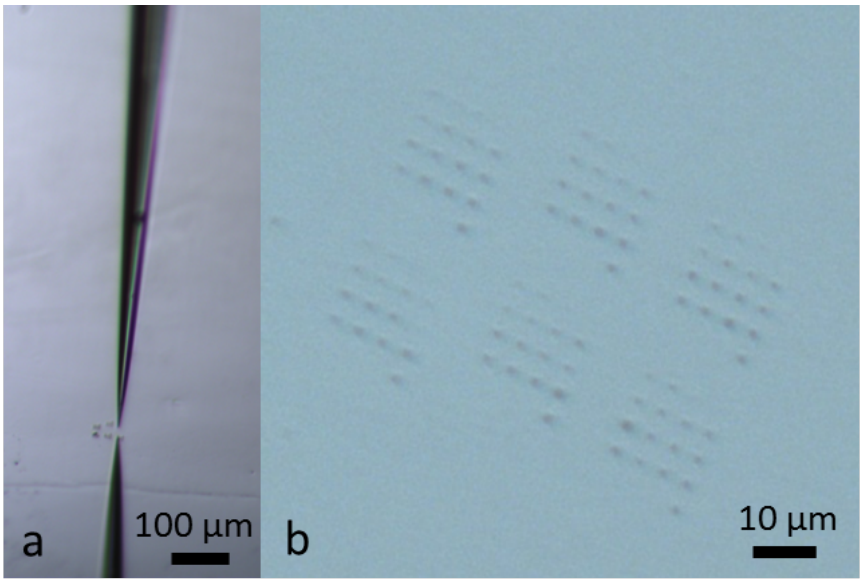

Figure 6.3: Optical images of: a) an experiment in progress; b) close up image of arrays of dissolution pits formed on a surface.

6.3.4 Atomic Force Microscopy

The SECCM etch pits were characterised using a Bruker Nano Enviroscope AFM with a Nanoscope IV controller in tapping mode. Tips used were 0.01-0.025 Ω cm Sb doped Si cantilevers (Bruker). The resultant images were analysed using SPIP 6.0.10 software.

6.4 Theory and Simulations

A 3D finite element method (FEM) model has been used to extract the acid induced dissolution rate of enamel. The theta pipette presents a symmetry plane perpendicular to the pipette septum such that it was possible to model only half a pipette, for computational efficiency, as illustrated in Figure 6.4. Values for the parameters used to describe the theta pipette geometry were typical values obtained through SEM images of the pipette: the major pipette radius perpendicular to the septum (mpr = 440 nm); the minor pipette tip radius parallel to the septum ($mptr$ = 260 nm); septum width (tw = 74 nm), pipette semi-angle ($semi\text{-}ang$ = 2.4°).

For simplicity the simulation assumed a planar enamel surface due to the relatively shallow pits formed after etching, especially at the short times. However, the meniscus contact width (mw) that is shown in Figure 6.4(a) was adjusted for each experimental time simulated, as informed from AFM data. The meniscus height (mh = 300 nm), and the fraction of the potential that falls across the simulation boundaries (E_f) were determined by matching the ionic conductance current in the simulation (with an inert substrate surface) to the experimental barrel current of an approach to an inert silicon oxide wafer substrate.[56] Whereas, the pipette height (ph = 100 µm), which is the height of the tip domain that was simulated, was chosen to be sufficiently large so not to influence the results of the simulation.[59] All simulations were carried out using the FEM simulation software Comsol Multiphysics (v4.3, Comsol AB) with LiveLink for Matlab (R2011a, Mathworks). The Nernst-Planck equation (equation 6.2) coupled with the electroneutrality condition (equation 6.3) was solved to determine ionic concentration distributions in the pipette and meniscus domains:

$$\bigtriangledown .(-D_i \bigtriangledown c_i - z_i u_i F c_i \bigtriangledown V) = R_i \tag{6.2}$$

$$\Sigma_i z_i c_i = 0 \tag{6.3}$$

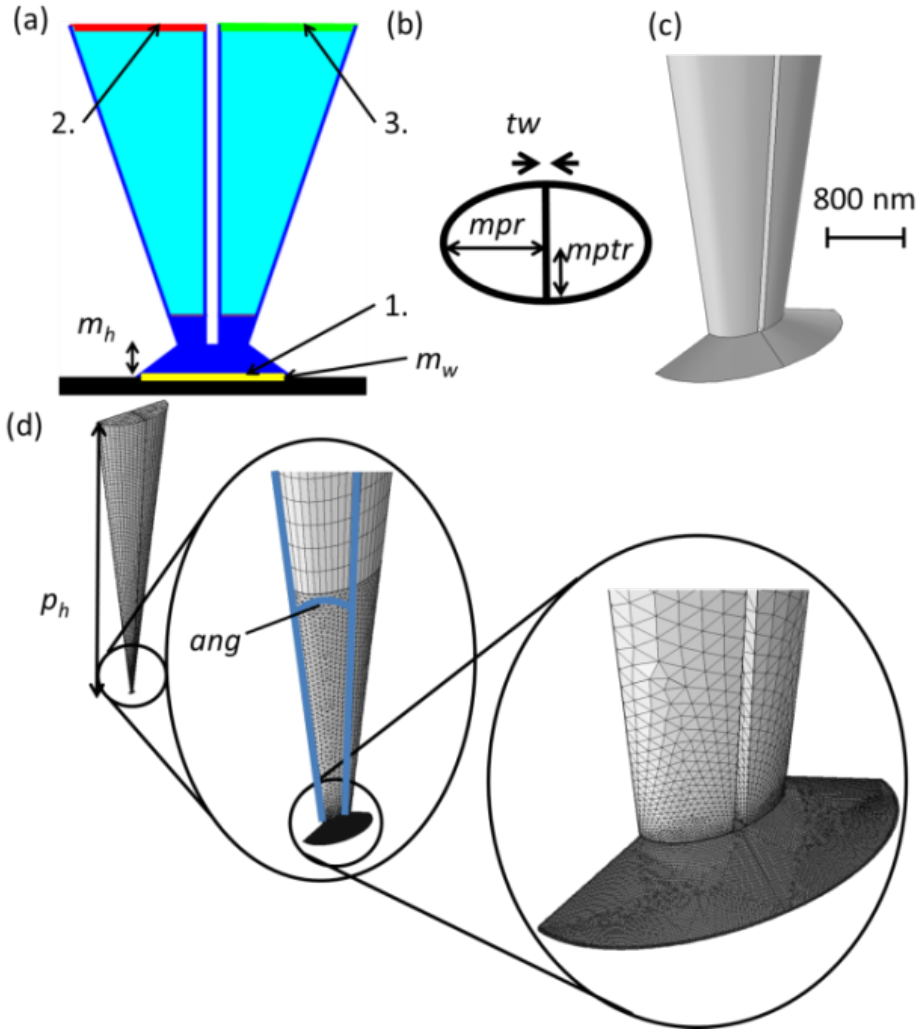

Figure 6.4: The pipette geometry used (a) 2D representation of the 3D simulations. (b) 2D representation of the end of the pipette. (c) The simulation geometry used zoomed into the region of the meniscus. (d) 3D representation of pipette also showing the meshing points used in experiments.

where c_i is concentration, D_i is diffusion coefficient (the values used are given in Table 6.1.),[56] z_i is charge, u_i is ionic mobility (calculated based on Einstein equation) of species i, F is Faraday constant, and V is the potential (between the 2 QRCEs). R_i indicates reactions leading to the formation or loss of species i within the field. Species in the solution were always kept at equilibrium, described by the

following equations.

$$H_3PO_4 \rightleftharpoons H^+ + H_2PO_4^- \qquad k_{a1}^* = \frac{[H_2PO_4^-][H^+]}{[H_3PO_4]} \quad (6.4)$$

$$H_2PO_4^- \rightleftharpoons H^+ + HPO_4^{2-} \qquad k_{a2}^* = \frac{[HPO_4^{2-}][H^+]}{[H_2PO_4^-]} \quad (6.5)$$

where k_{a1}^* and k_{a2}^* are acid dissociation constants for H_3PO_4 and $H_2PO_4^-$ respectively, that are corrected for the ion activity coefficients using MINEQL+ (Chemical Equilibrium Modelling System v4.6). In this simulation, convection from the electroosmotic flow was reasonably assumed to be negligible and so was not included because diffusion and migration play a much larger role under the experimental conditions.[58] As the experimental contact times (1-16 s) were much longer than the time needed to reach steady-state in the pipette, it was reasonable to assume steady-state dissolution for the simulation.[56] The initial concentrations for Ca^{2+}, HPO_4^{2-}, $H_2PO_4^-$, and H_3PO_4 were assigned to zero in the simulated domain. The bulk concentrations were maintained at the boundaries 2 and 3 (Figure 6.4(a)) with the following equation:

$$c_i = c_{0,i} \quad (6.6)$$

where c_i is instantaneous concentration at the boundary and $c_{0,i}$ is initial concentration of species i. To simulate the bias, 0 V was applied to surface 3 (one barrel), and E_f is applied to surface 2 (the other barrel). At the interface between the meniscus and the enamel surface, represented in 2D (Figure 6.4(a)) with surface 1 as enamel (yellow), a flux of H^+, Ca^{2+} and HPO_4^{2-} was applied. The flux of these species was directly related to the flux of protons at the enamel surface using the following equations:

$$-nN_{Ca^{2+}} = \frac{10}{8}\, k_0[H^+] \quad (6.7)$$

$$-nN_{H_2PO_4^{2-}} = \frac{6}{8}\, k_0[H^+] \quad (6.8)$$

$$-nN_{H^+} = -k_0[H^+] \tag{6.9}$$

where n is the inward unit vector and N_i is flux vector of species i, the intrinsic rate constant for the dissolution is k_0. The fractions (10/8) and (6/8) represents the stoichiometry coefficients of the acid dissolution reaction (equation 6.1); where protons are removed from the system, while, HPO_4^{2-} and Ca^{2+} are produced. All other boundaries, pipette walls and meniscus sides, were considered to be electrically insulating and have no flux.

Table 6.1: Diffusion coefficients of key solution species.[62]

Species	Ca^{2+}	H^+	OH^-	K^+
Diffusion coefficient (10^{-9} m^2 s^{-1})	0.792	7.80	5.273	1.957
Species	NO_3^-	H_3PO_4	$H_2PO_4^-$	HPO_4^{2-}
Diffusion coefficient (10^{-9} m^2 s^{-1})	1.902	0.882	0.959	0.759

6.5 Results and Discussion

6.5.1 Etch Pit analysis

Six arrays (each comprising 16 etch pits) were generated on each of the four enamel samples for each treatment. This resulted in 384 etch pits for each of the four treatment conditions, all of which were analysed using AFM. A representative AFM image of an array is shown in Figure 6.5. There is a noticeable trend towards deeper and wider dissolution pits with increased time.

The volume of the pits for each hold time was averaged across all the arrays and samples to produce Figure 6.6(a), which shows pit volume against meniscus contact time for untreated enamel, F^- treated enamel, Zn^{2+} treated enamel and

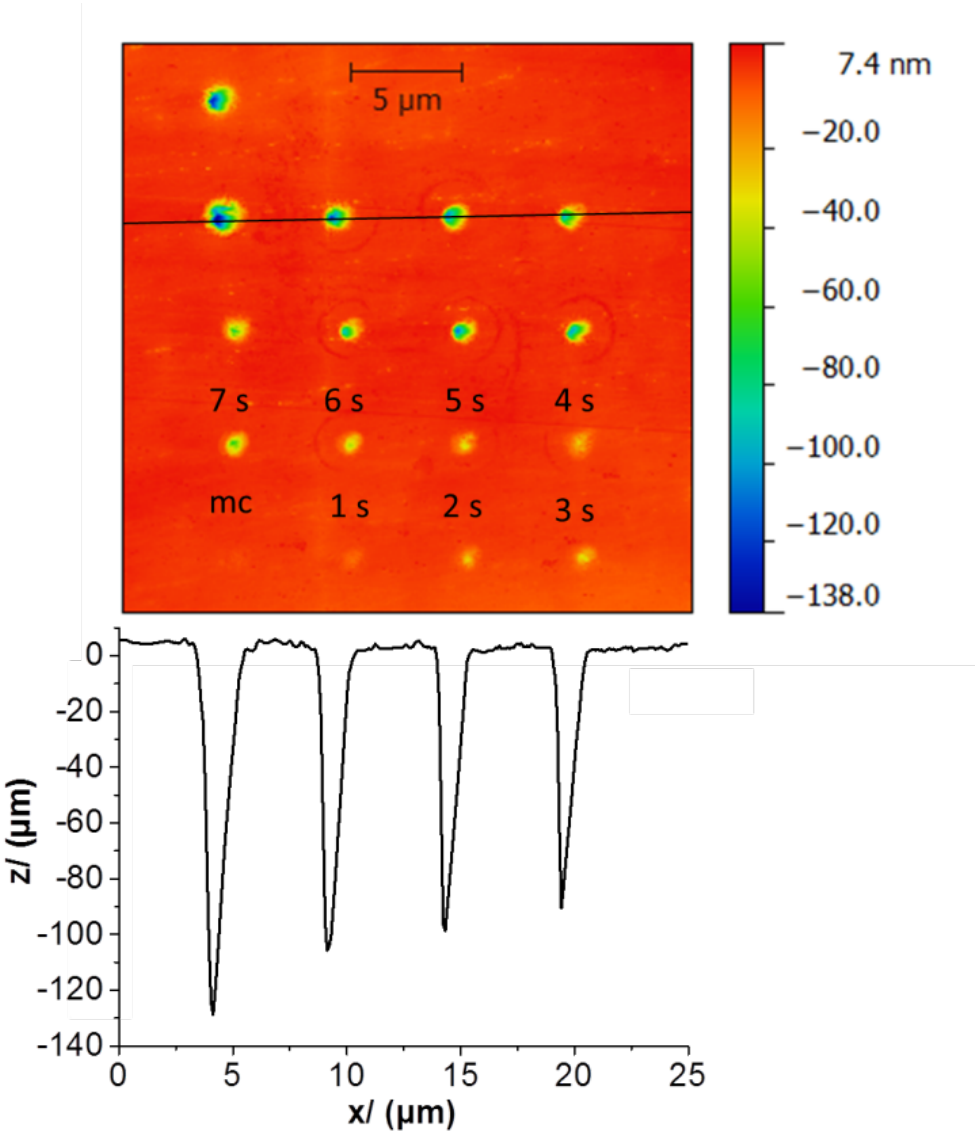

Figure 6.5: Typical array of etch pits formed using SECCM. Black line marks point of the profile at the bottom of the AFM image. The first point only makes momentary contact (mc) used for orientation of the sample.

the combined treatment. These data highlight that the etch pit volume increases with time for all surface types, but the extent of dissolution is greatest for untreated enamel. Treatment of the surfaces inhibits the extent of dissolution, although the difference from the untreated is most noticeable at short times. This is also evident in the plot of pit depth *vs.* time (Figure 6.6(b)).

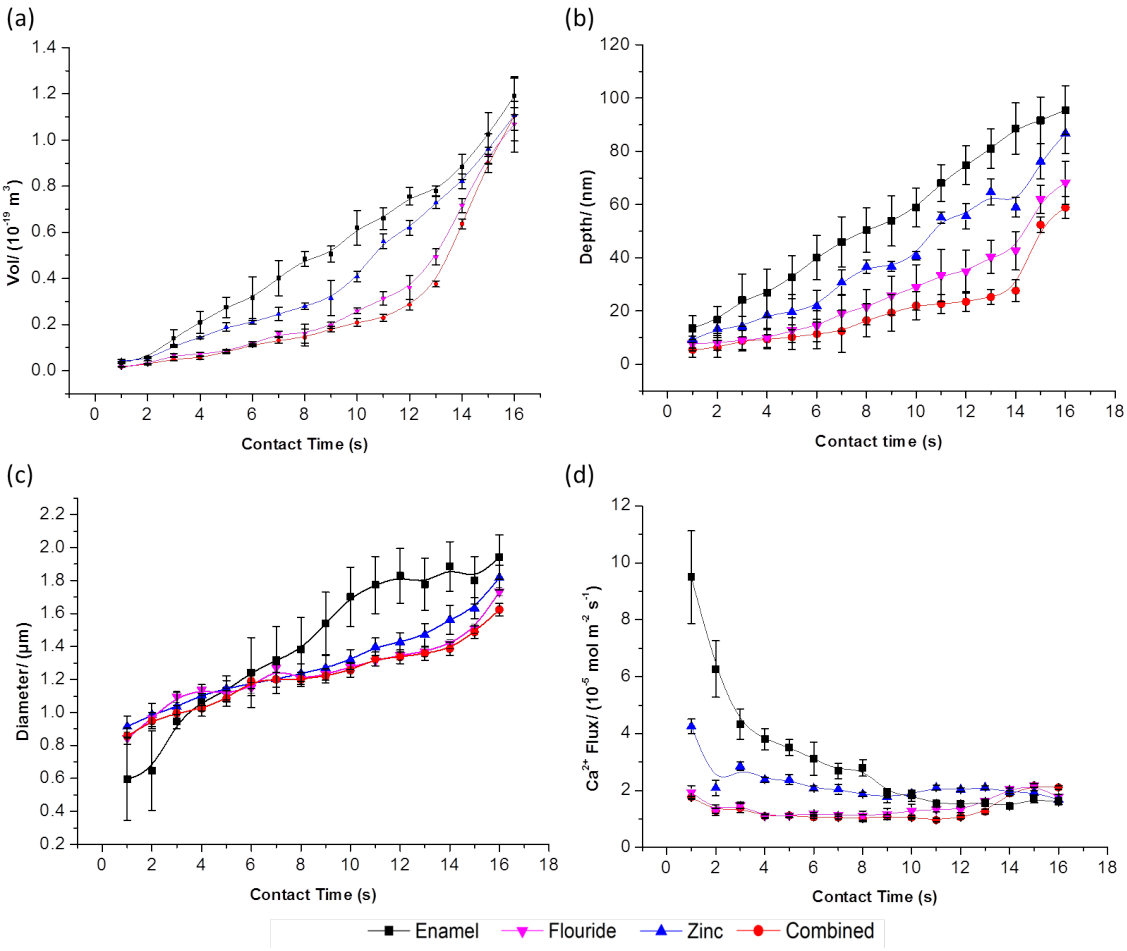

Figure 6.6: Graphs of contact time versus (a) Average etch pit volume. (b) Average pit depth. (c) Average pit diameter. (d) Average Ca^{2+} flux. Error bars show standard error of the mean, n=24. Curves through the points are to guide the eye.

In order to elucidate quantitative dissolution rates, it was necessary to know the pit diameter (Figure 6.6(c)), which relates to the area of meniscus contact. The change in diameter, and thus the area of contact between the meniscus and the surface, was taken into account and inputted into the simulations used to analyse the data i.e. a time dependant meniscus area was considered to ensure that surface fluxes were determined with high accuracy (*vide infra*, e.g. Figure 6.8). Another note is the possibility of leaving an aqueous droplet on the surface once the probe is retracted, this effect is considered to be minimal as the depth of the pits is found to be highly dependant on the etching time, which suggests that no or small volume drop is left behind and this is not affecting the pits morphology.[59]

Overall, the treatments appear to show fluoride providing more protection of the enamel surface to acid attack than zinc, with the combined treatment providing the greatest protection. However, at longer times, the treatments are less effective, based on the data in Figure 6.6. This is because the treatments only affect the surface layer of the enamel. The effect of the treatment does not penetrate substantially into the sample and protect the subsurface; this indicates these surface treatments would be suitable as a treatment that is applied regularly, such as toothpaste as in the mouth. In this situation treatments would be retained for longer periods of time and any newly exposed enamel would be further subjected to treatment.

The flux of Ca^{2+} ($\mathrm{mol\,cm^{-1}\,s^{-2}}$) was determined using the time-dependant pit volume and area (calculated using SPIP 6.0.10 software) to calculate the molar amount of enamel removed (density of enamel is 3.16 $\mathrm{g\,cm^{-3}}$, molar mass is 502 $\mathrm{g\,mol^{-1}}$).[15–19] The average flux for each contact time is shown in Figure 6.6(d).

6.5.2 Simulation

The model described earlier was implemented to calculate Ca^{2+} interactions and fluxes as a function of k_0 which was varied in the simulations between 1×10^{-3} $\mathrm{cm\,s^{-1}}$ and 7×10^{-5} $\mathrm{cm\,s^{-1}}$. The ratio of the diameter of contact area (obtained from AFM

images of pit, as described) to the diameter of the pipette was varied between 0.5 and 3. Fig 6.7 shows example concentration profiles for the key species involved in the acid attack and dissolution process for a rate constant, $k_0 = 0.08\ \mathrm{cm\,s^{-1}}$, which is at the upper end of those measured experimentally (*vide infra*). It can be seen that protons are significantly consumed at the enamel surface (interfacial concentration *ca.* 0.1 mM) but that, even with this rate constant, there is some contribution from surface treatments, which can be determined. The profiles also show that there is some asymmetry in the diffusion of ions to and from the surface due to the electric field between the 2 QRCEs in the Pipette.[56]

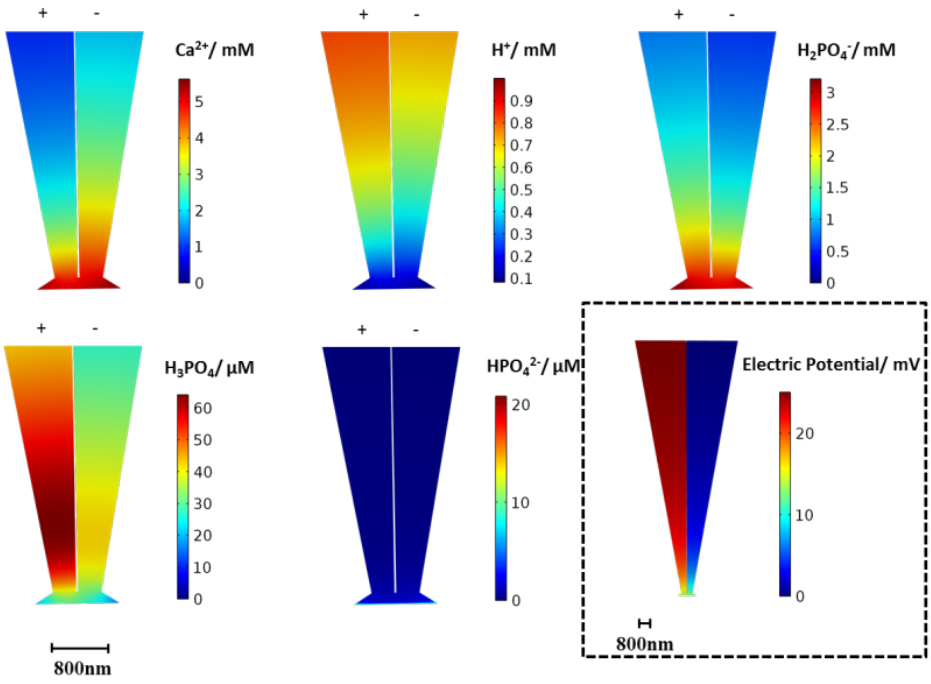

Figure 6.7: The concentration profiles of simulated species and electric potential at the end of the tip using an intrinsic rate constant of 0.08 $\mathrm{cm\,s^{-1}}$.

6.5.3 Determination of dissolution kinetics

A 3-D working plot showing the interfacial calcium flux from the enamel surface as a function of the dissolution (acid attack) rate constant and ratio of meniscus radius

to pipette radius ratio is shown in Figure 6.8. The experimental data yield $j_{ca^{2+}}$, as described above, along with the area of meniscus contact, leaving the kinetic term, k_{Hsurf}, which can then easily be determined. This calibration surface was used to derive the rate constant using the experimental results for all four treatment conditions and over all times. The average rate constant for each treatment is shown in Table 6.5.3. The result for the untreated enamel substrate is comparable to that of our previous work, 0.08 ± 0.04 cm s^{-1} using a different technique giving great confidence in the untreated enamel result.[30] The variation between the rates constants for different treatments was proven to have statistical significance by using one-way analysis of variance (ANOVA) ($p = 2.9 \times 10^{-9}$, 99%).

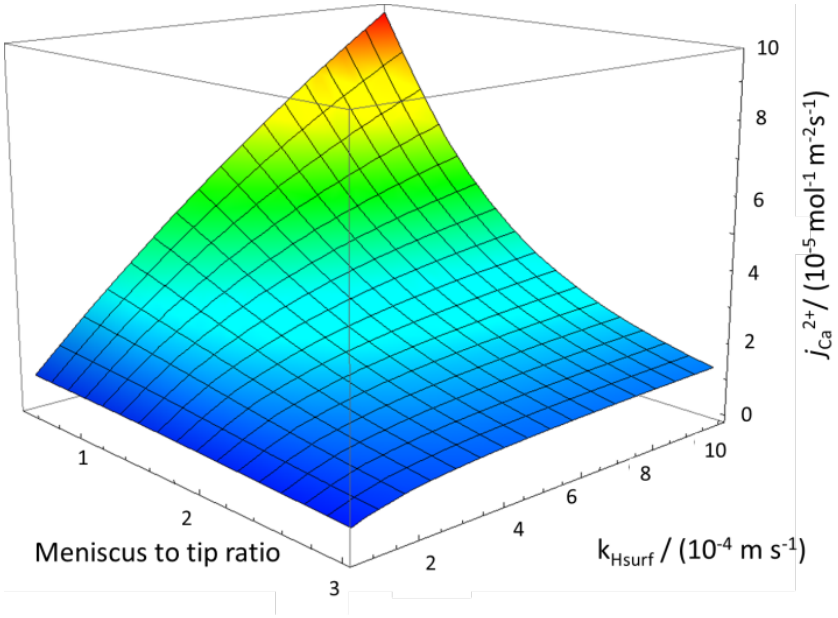

Figure 6.8: Simulated results showing Ca^{2+} flux (mol cm^{-2} s^{-1}) textitvs. intrinsic rate constant of dissolution (m s^{-1}) *vs.* meniscus to tip ratio.

Table 6.2: Calculated intrinsic rate constants for the different enamel substrates. Error is standard error of the mean (n=16).

Sample	**Intrinsic rate constant for H^+ attack ($\mathbf{cm\,s^{-1}}$)**	**Intrinsic rate constant for Ca^{2+} release ($\mathbf{cm\,s^{-1}}$)**
Enamel	0.079 ± 0.007	0.099 ± 0.008^a
Zinc treated	0.047 ± 0.006	0.058 ± 0.007^b
Fluoride treated	0.027 ± 0.006	0.033 ± 0.008^c
Combined treated	0.019 ± 0.004	0.025 ± 0.005^d

* Values with different letters are statistically different ($p < 0.01$): letters denote statistical comparison for different treatments by ANOVA and Tukey-Kramer analysis.

6.6 Conclusions

This study has presented a new method of combinatorial localised dissolution analysis highlighting the ability of SECCM to make multiple, rapid, localised, and independent measurements on a single surface, under conditions of highly defined and fast mass transport. Combined with AFM analysis of the resulting etched features, this provides a powerful platform to investigate surface processes. In the present study, by following the dissolution reaction with time, it has been possible to elucidate the efficacy of surface treatments on enamel dissolution, and how this changes during etching. With the additional information provided by FEM modelling,this method has proven to be particularly powerful for the investigation of dental enamel surfaces. Herein, the presented technique provides cheep and fast procedure to test multiple treatment simultaneously, as a single sample can be subjected to multiple treatments and their relative efficacy could be assessed under the same conditions. A particularly powerful aspect of the technique is that dissolution can be monitored for very short times, which is very beneficial as surface treatments often provide only a thin, transient coating. We expect that this approach could have myriad

applications in the future for examining surface coatings and treatments. Although not exploited in this study, it should also be pointed out that dissolution can be monitored via the ion-conductance current during meniscus contact[59] which further enhances the capabilities of this technique.

For the systems studied it has been found that both zinc and fluoride act initially to protect enamel from acid-induced dissolution, with fluoride having the greatest effect, whilst a combination of both treatments provided the optimum protection. This study demonstrates that the method outlined can be used to test treatments in a high throughput, automated approach to test single and multiple (combination) treatments of a surface very quickly and effectively.

6.7 References

(1) Dokoumetzidis, A.; Macheras, P. *Int. J. Pharm.* **2006**, 321, 1-11.

(2) Orr, J. C.; Fabry, V. J.; Aumont, O.; Bopp, L.; Doney, S. C.; Feely, R. A.; Gnanadesikan, A.; Gruber, N.; Ishida, A.; Joos, F.; Key, R. M.; Lindsay, K.; Maier-Reimer, E.; Matear, R.; Monfray, P.; Mouchet, A.; Najjar, R. G.; Plattner, G. K.; Rodgers, K. B.; Sabine, C. L.; Sarmiento, J. L.; Schlitzer, R.; Slater, R. D.; Totterdell, I. J.; Weirig, M. F.; Yamanaka, Y.; Yool, A. *Nature* **2005**, 437, 681-686.

(3) Bjorklund, R. B.; Arwin, H. *Langmuir* **1992**, 8, 1709-1714.

(4) Sherif, E.-S. M.; Erasmus, R. M.; Comins, J. D. *J. Colloid Interface Sci.* **2007**, 309, 470-477.

(5) Smith, D. C.; Simon, M.; Alldredge, A. L.; Azam, F. *Nature* **1992**, 359, 139-142.

(6) Azarmi, S.; Roa, W.; Lobenberg, R. *Int. J. Pharm.* **2007**, 328, 12-21.

(7) Demadis, K. D.; Lykoudis, P.; Raptis, R. G.; Mezei, G. *Cryst. Growth Des.* **2006**, 6, 1064-1067.

(8) Desarnaud, J.; Grauby, O.; Bromblet, P.; Vallet, J.-M.; Baronnett, A. *Cryst. Growth Des.* **2013**, 13, 1067-1074.

(9) Kameda, J.; Sugimori, H.; Murakami, T. *Phys. Chem. Miner.* **2009**, 36, 537-544.

(10) Mauldin, T. C.; Kessler, M. R. *J. Mater. Chem.* **2010**, 20, 4198-4206.

(11) Peruffo, M.; Mbogoro, M. M.; Edwards, M. A.; Unwin, P. R. *PCCP* **2013**, 15, 1956-1965.

(12) Yu, H.-D.; Yang, D.; Wang, D.; Han, M.-Y. *Adv. Mater.* **2010**, 22, 3181-3184.

(13) Unwin, P. R.; Macpherson, J. V. *Chem. Soc. Rev.* **1995**, 24, 109-119.

(14) Unwin, P. R. *J. Chem. Soc., Faraday Trans.* **1998**, 94, 3183-3195.

(15) Robinson, C.; Shore, R. C.; Brookes, S. J.; Strafford, S.; Wood, S. R.; Kirkham, J. *Crit. Rev. Oral Biol. Medicine* **2000**, 11, 481-495.

(16) Boyde, A. In *Teeth*; Springer Berlin Heidelberg, **1989**, pp 309-473.

(17) Shellis, R. P. *Arch. Oral Biol.* **1984**, 29, 697-705.

(18) Kay, M. I.; Young, R. A.; Posner, A. S. *Nature* **1964**, 204, 1050-1052.

(19) Francisconi, L. F.; Honorio, H. M.; Rios, D.; Magalhaes, A. C.; Machado, M. A. A. M.; Buzalaf, M. A. R. *Oper. Dent.* **2008**, 33, 203-208.

(20) West, N. X.; Hughes, J. A.; Addy, M. *J. Oral Rehabil.* **2000**, 27, 875-880.

(21) Higuchi, W. I.; Gray, J. A.; Hefferren, J. J.; Patel, P. R. *J. Dent. Res.* **1965**, 44, 330-341.

(22) Phillips, R. W.; Van Huysen, *G. J. Chem. Educ.* **1946**, 23, 579.

(23) Gray, J. A. J. Dent. Res. **1962**, 41, 633-645.

(24) Kwon, K.-Y.; Wang, E.; Chung, A.; Chang, N.; Lee, S.-W. *J. Phys. Chem. C* **2009**, 113, 3369-3372.

(25) Scheckel, K. G.; Ryan, J. A. *Environ. Sci. Technol.* **2002**, 36, 2198-2204.

(26) Dorozhkin, S. V. *Prog. Cryst. Growth Charact. Mater.* **2002**, 44, 45-61.

(27) Linge, H. G.; Nancolla, G. H. *Calcif. Tissue Res.* **1973**, 12, 193-208.

(28) Wu, M.-S.; Higuchi, W. I.; Fox, J. L.; Friedman, M. *J. Dent. Res.* **1976**, 55, 496-505.

(29) Bishop, D. W.; Eick, J. D.; Nancolla, G. H.; White, W. D. *J. Dent. Res.* **1974**, 53, 198-198.

(30) White, W. D.; Nancollas, G. H. *J. Dent. Res.* **1980**, 59, 1180-1186.

(31) Wu, M. S.; Higuchi, W. I.; Fox, J. L.; Friedman, M. *J. Dent. Res.* **1976**, 55, 496-505.

(32) White, W.; Nancollas, G. H. *J. Dent. Res.* **1977**, 56, 524-530.

(33) Nancollas, G. H.; Sawada, K.; Schuttringer, E. In *Biomineralization and Biological Metal Accumulation*, Westbroek, P.; de Jong, E. W., Eds.; Springer Netherlands, 1983, pp 155-169.

(34) Voegel, J. C.; Frank, R. M. *Calcif. Tissue Res.* **1977**, 24, 19-27.

(35) Barbour, M. E.; Parker, D. M.; Allen, G. C.; Jandt, K. D. *Eur. J. Oral Sci.* **2003**, 111, 258-262.

(36) Finke, M.; Jandt, K. D.; Parker, D. M. *J. Colloid Interface Sci.* **2000**, 232, 156-164.

(37) Pyne, A.; Marks, W.; Picco, L. M.; Dunton, P. G.; Ulcinas, A.; Barbour, M. E.; Jones, S. B.; Gimzewski, J.; Miles, M. J. *Arch. Histol. Cytol.* **2009**, 72, 209-215.

(38) Johnson, N. W.; Poole, D. F. G.; Tyler, J. E. *Arch. Oral Biol.* **1971**, 16, 385-394.

(39) Wang, L. J.; Tang, R. K.; Bonstein, T.; Orme, C. A.; Bush, P. J.; Nancollas, G. H. *J. Phys. Chem. B* **2005**, 109, 999-1005.

(40) McGeouch, C.-A.; Edwards, M. A.; Mbogoro, M. M.; Parkinson, C.; Unwin, P. R. *Anal. Chem.* **2010**, 82, 9322-9328.

(41) Qin, L.; Zhang, W.; Lu, J.; Stack, A. G.; Wang, L. *Environ. Sci. Technol.* **2013**, 47, 13365-13374.

(42) Ma, Q. Y.; Logan, T. J.; Traina, S. J.; Ryan, J. A. *Environ. Sci. Technol.* **1994**, 28, 408-418.

(43) Tanizawa, Y.; Sawamura, K.; Suzuki, T. *J. Chem. Soc., Faraday Trans.* **1990**, 86, 1071-1075.

(44) Martin, R. D.; Beeston, M. A.; Unwin, P. R.; Laing, M. E. *J. Chem. Soc., Faraday Trans.* **1994**, 90, 3109-3115.

(45) McCann, H. G. *Arch. Oral Biol.* **1968**, 13, 987-1001.

(46) Ten Cate, J. M.; Featherstone, J. D. B. *Crit. Rev. Oral Biol. Med.* **1991**, 2, 283-296.

(47) Peld, M.; Tõnsuaadu, K.; Bender, V. *Environ. Sci. Technol.* **2004**, 38, 5626-5631.

(48) Gray, J. A. *J. Dent. Res.* 1965, 44, 493-501.

(49) Kwon, K.-Y.; Wang, E.; Nofal, M.; Lee, S.-W. *Langmuir* **2011**, 27, 5335-5339.

(50) Wang, X.; Klocke, A.; Mihailova, B.; Tosheva, L.; Bismayer, U. *J. Phys. Chem. B* **2008**, 112, 8840-8848.

(51) Loher, S.; Stark, W. J.; Maciejewski, M.; Baiker, A.; Pratsinis, S. E.; Reichardt,

D.; Maspero, F.; Krumeich, F.; Günther, D. *Chem. Mater.* **2005**, 17, 36-42.

(52) Honda, Y.; Anada, T.; Morimoto, S.; Shiwaku, Y.; Suzuki, O. *Cryst. Growth Des.* **2011**, 11, 1462-1468.

(53) Chin, K. O. A.; Nancollas, G. H. *Langmuir* **1991**, 7, 2175-2179.

(54) Mohammed, N. R.; Mneimne, M.; Hill, R. G.; Al-Jawad, M.; Lynch, R. J. M.; Anderson, P. *J. Dent.* **2014**, 42, 1096-1104.

(55) Ebejer, N.; Schnippering, M.; Colburn, A. W.; Edwards, M. A.; Unwin, P. R. *Anal. Chem.* **2010**, 82, 9141-9145.

(56) Snowden, M. E.; Güell, A. G.; Lai, S. C. S.; McKelvey, K.; Ebejer, N.; O'Connell, M. A.; Colburn, A. W.; Unwin, P. R. *Anal. Chem.* **2012**, 84, 2483-2491.

(57) McKelvey, K.; O'Connell, M. A.; Unwin, P. R. *Chem. Commun.* **2013**, 49, 2986-2988.

(58) Ebejer, N.; Güell, A. G.; Lai, S. C. S.; McKelvey, K.; Snowden, M. E.; Unwin, P. R. *Annu. Rev. Anal. Chem. (Palo Alto Calif.)* **2013**, 6, 329-351.

(59) Kinnear, S. L.; McKelvey, K.; Snowden, M. E.; Peruffo, M.; Colburn, A. W.; Unwin, P. R. *Langmuir* **2013**, 29, 15565-15572.

(60) Parker, A. S.; Patel, A. N.; Al Botros, R.; Snowden, M. E.; McKelvey, K.; Unwin, P. R.; Ashcroft, A. T.; Carvell, M.; Joiner, A.; Peruffo, M. *J. Dent.* **2014**, *Supplement 1,* 42, S21-S29.

(61) Chen, C.-H.; Meadows, K. E.; Cuharuc, A.; Lai, S. C. S.; Unwin, P. R. *PCCP* **2014**, 16, 18545-18552.

(62) Lide, D. R. *CRC Handbook of Chemistry and Physics, 90th Edition;* Taylor & Francis, 2009.

Chapter 7

Conclusions and Remarks

BM-SICM, presented in Chapter 2, allows the simultaneous tracking of topography and mapping of charge density for a surface by hopping mode, which cannot be easily obtained using other techniques. The novelty of this approach was coupled with developing a numerical model introducing the potential perturbation signal, to establish an understanding of the physical phenomena associated with it. This enabled the design and analysis of the experiments, to provide information about the topography of the surface without interference from the surface charge density. This is accomplished through minimising the ion rectification which is induced by the surface charge by eliminating the bias offset during the tip approach. Cyclic voltammograms are then acquired at the end of each approach (close to the surface) which supplies vital additional information through the AC component amplitude and phase, that can be used along the theoretical model to analyse the probe response and resolve the surface charge. This method represents a major advance in surface science as charge mapping have proved to be challenging to probe and visualise.

CLSM-SECM, presented in Chapter 3, is a new approach into the visualisation of proton lateral diffusion profiles in bulk and near a surface. The proton

profile is generated through water oxidation at the UME, and the fluorescence confocal laser scanning microscopy tracked the pH changes near the surface through fluorescence intensity changes of the pH sensitive fluorophore *fluorescein*. This new coupled technique could find applications in a wide range of fields, especially for studying biological samples.

As presented in Chapters 4 and 5, new dual function probes, which were quick and easy to fabricate, were developed. A key aspect of this work was the development of numerical models, which enabled the rational design and analysis of optimal experiments.

Finally, in Chapter 6, the theta-barrelled droplet technique, SECCM, was extended to understand acid-induced dissolution of enamel, and investigate the effect of surface treatments on the dissolution kinetics. Once again, the numerical simulation enabled quantitative analysis of dissolution rates for the untreated enamel and various treatments effects.

In summary, this thesis has described major advances in the development of EC-SPM techniques, that have been used to investigate surface charge (Chapter 2), pH tracking (Chapters 3 and 5), calcium activity measurements (Chapter 4), and enamel acid-induced dissolution (Chapters 3 and 6). Finite element method numerical simulations have proven to be a powerful analysis tool to maximise the extraction of critical quantitative information, without which the experiments would only have been qualitative.

This thesis provides a platform of new techniques and quantitative models that will enable future development of applications of EC-SPMs in a wide range of areas, from cell biology to materials fabrication, and fundamental surface chemistry studies.